

# 3 Nuclear Reactions

L. G. Sobotka<sup>1</sup> · V. E. Viola<sup>2</sup>

<sup>1</sup>Washington University, St. Louis, Missouri, USA

<sup>2</sup>Indiana University, Bloomington, Indiana, USA

<b>3.1</b>	<b><i>Introduction</i></b> .....	<b>145</b>
<b>3.2</b>	<b><i>Basic Concepts</i></b> .....	<b>148</b>
3.2.1	Shorthand Notation for Nuclear Reactions .....	149
3.2.2	Mass-Energy Conservation: The Q-Value .....	150
3.2.3	The Nuclear Potential Energy: Coulomb Barrier Effects .....	152
3.2.4	Angular Momentum Effects: The Centrifugal Barrier .....	154
3.2.5	Summary of Energetic Factors in Nuclear Reactions and the Separation of Thermodynamic and Kinetic Factors .....	156
3.2.6	Cross Sections: An Introduction .....	157
3.2.7	Cross Sections, Excitation Functions, and Angular Distributions .....	159
3.2.8	Cross-Section Measurements .....	161
<b>3.3</b>	<b><i>Scattering Theory</i></b> .....	<b>161</b>
3.3.1	Preliminaries .....	161
3.3.2	The Optical Model (OM) .....	164
3.3.3	The Dispersive Optical Model (DOM) .....	169
<b>3.4</b>	<b><i>Near-Barrier Reaction Mechanisms</i></b> .....	<b>171</b>
3.4.1	Neutron Capture .....	173
3.4.2	Nucleon and Heavy-Ion Elastic Scattering .....	177
3.4.2.1	Nucleon Elastic Scattering .....	177
3.4.2.2	Heavy-Ion Elastic Scattering .....	179
3.4.3	Inelastic Excitation .....	180
3.4.4	Nucleon Knockout Reactions .....	185
3.4.5	Mean-Field-Dominated HI Reactions .....	187
3.4.5.1	Impact Parameter Dictates the Reaction Channel .....	187
3.4.5.2	Surface Reactions: Inelastic Scattering and Nucleon Transfer .....	188
3.4.5.3	Damped Collisions .....	189
3.4.5.4	Composite-Nucleus Formation .....	190
<b>3.5</b>	<b><i>Statistical Decay</i></b> .....	<b>192</b>
3.5.1	Preliminaries .....	192
3.5.2	The Hauser–Feshbach Treatment of Particle Emission .....	193
3.5.3	The Transition-State Treatment of CN Decay .....	194
3.5.4	The Density of States of Highly Excited Nuclei .....	195
3.5.5	Thermodynamic Models for Multifragmentation .....	196

<b>3.6</b>	<b><i>Mechanisms in the Nucleon-Nucleon Domain</i></b>	<b>198</b>
3.6.1	Reactions Near the Fermi Energy	201
3.6.2	Models of Collision Dynamics	202
3.6.3	Participant–Spectator Reactions	204
3.6.4	Relativistic Heavy-Ion Collisions: Dense Nuclear Matter	205
<b>3.7</b>	<b><i>The Nuclear Equation of State</i></b>	<b>207</b>
3.7.1	Background and Connection to Classical Thermodynamics	207
3.7.2	The Perspective from Energy-Density-Functional Theory	209
3.7.3	The Incompressibility from the Physical LDM-Like Expansion	210
3.7.4	Cluster Formation at Very Low Density	212
3.7.5	Multifragmentation: The Low-Density Regime and the Manifestation of the Liquid–Gas Phase Transition in Nuclear Collisions	213
<b>3.8</b>	<b><i>Addendum: Cross-Section Calculations</i></b>	<b>216</b>
<b>3.9</b>	<b><i>Selected Nuclear Reaction Web Resources</i></b>	<b>218</b>

**Abstract:** The investigation and application of nuclear reactions play a prominent role in modern nuclear chemistry research. After a discussion of basic principles and reaction probabilities that govern collisions between nuclei, an overview of reaction theory is presented and the various reaction mechanisms that occur from low to high energies are examined. The presentation strives to provide links to more standard chemical disciplines as well as to nuclear structure.

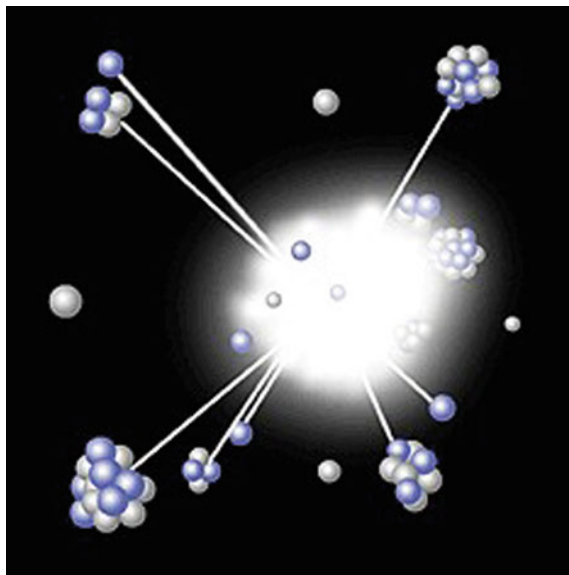
### 3.1 Introduction

Current understanding of nuclear reactions has been significantly expanded by developments in accelerator technology, which now provide nuclear science with a highly diverse arsenal of nuclear projectiles. It is possible to probe the nucleus with beams of photons, electrons, mesons, neutrons, antiprotons, and virtually all naturally occurring isotopes of elements ranging from hydrogen to uranium. In addition, there is a growing capability to accelerate radioactive nuclei off the line of beta stability.

This arsenal of tools has allowed the response of nuclei to excitation energy, angular momentum, and neutron/proton asymmetry to be studied. Excitation energies from the smallest allowed (excitation to the first allowed quantum state above the ground state) to that corresponding to the capture of a thermal neutron (one binding energy  $B_N$ ), to that required to totally vaporize a nucleus with  $A$  nucleons (• Fig. 3.1), an excitation energy of the order of  $AB_N$ , have all been investigated. The study of highly excited nuclei has provided new insights into nuclear systems with bulk densities both higher and lower than the central density

■ Fig. 3.1

Reconstruction of a highly energetic nuclear collision that disintegrates a gold nucleus into multiple nucleons and light clusters



of ground-state nuclei, densities which nature readily accesses in astrophysical objects. Similarly, the nuclear response to angular momentum from zero to that which prompts nuclei to fission (no matter what position in the periodic table) has been examined. Most recently, the use of secondary beams for reaction studies has allowed the study of nuclei formed in nature during nucleosynthesis of the elements – nuclei that previously had been inaccessible to experiment.

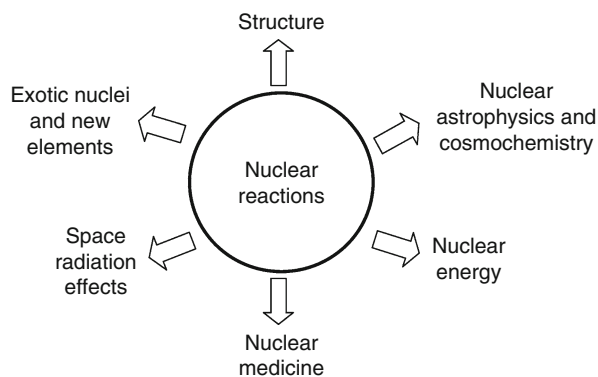
From a broader perspective, progress in related fields of nuclear science has frequently evolved from nuclear reaction studies, as indicated schematically in [Fig. 3.2](#). Reaction studies provide pathways for exploring nuclear structure, the formation of both new elements as well as isotopes of known elements (Loveland 2007), and nuclear astrophysics. At the more practical level, important nuclear applications have resulted from reaction studies, for example, nuclear energy, nuclear medicine (both for diagnostic imaging and therapy), activation analysis, and space-radiation effects due to cosmic-ray exposure.

The vantage point that will be maintained for the bulk of this chapter is that the atomic nucleus can be viewed as a two-component quantum fluid, i.e., the degrees of freedom are those associated with nucleons. Despite the quantum nature of the systems, classical analogs can be of great heuristic value. Leading this list of analogs is that of a charged two-component liquid drop. Here, the quantum aspects are buried in a few well-chosen coefficients of a physical expansion.

The Fermi-Gas Model applies a thin veneer of quantum mechanics to the Liquid-Drop Model (LDM), i.e., the Pauli exclusion principle must be obeyed by the spin  $\frac{1}{2}$  nucleons and thus neutrons and protons must occupy distinct quantum levels. The energy of the top-most occupied level in this simple picture is called the Fermi energy,  $E_F$ . There is a Fermi energy for neutrons and another for protons, each corresponding to a chemical potential, i.e., the energy associated with the addition or subtraction of a nucleon. The kinetic energies of the nucleons forced by the Pauli principle lead to an internal pressure (intimately related to that which holds up a neutron star against gravitational collapse), but, as the surface of a stable nucleus is stationary, the pressure must return to zero at the periphery (just as it must on the surface of a neutron star or any other self-bound stable object.)

■ Fig. 3.2

**Schematic representation of nuclear reactions as applied to other areas of science and technology**



At the next higher level of sophistication, a specific quantization is envisioned by imagining independent particles in a (real) central potential. The consequences of this confinement are the granularization of the single-particle states labeled by orbital angular momentum ( $\ell$ ) and its orientation relative to the nucleon's spin ( $s$ ). The quantum state of the nucleon, either in the entrance or exit channel, can dictate which nuclear reaction channel dominates. Turned around, studying reactions can provide insight into the underlying nuclear structure of the reactants or products.

Beyond the view of nuclei as nucleons moving independently in a mean field, one appreciates that the constituents are often engaged in complex correlations. This is akin to what one finds in water, where correlations (induced by hydrogen bonding) must be understood. However, unlike systems such as water, in which the correlations between identical units determine the interesting material properties, the nuclear system is composed of two distinguishable components.

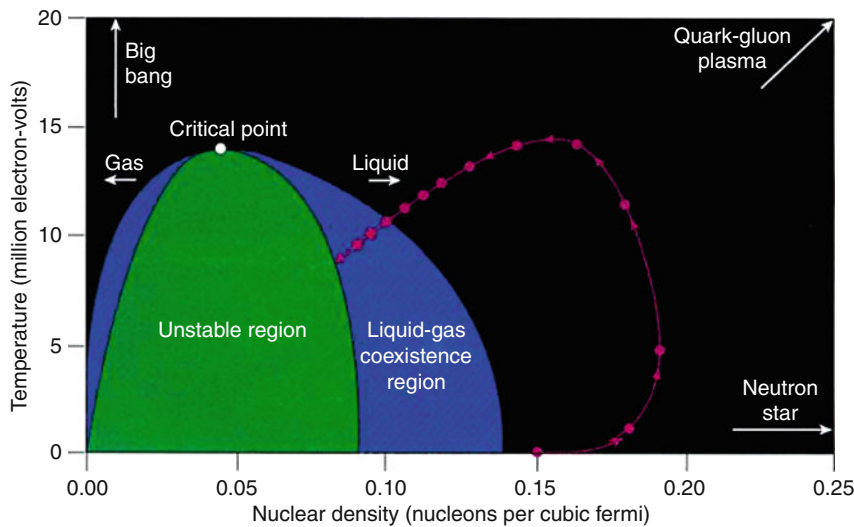
In-medium correlations have many observable effects. They influence the mass of nuclei and if one were to create a one-body potential to mock up their effects, it would cause clustering of levels around the Fermi surface. This, in turn, changes the density of many-body states  $\omega(E^*)$ ; the number of ways nucleons can distribute themselves into the allowed single-particle states within an excitation energy window. The density of states is Boltzmann's *wahrscheinlichkeit* in the expression  $S(E^*) = k_B \ln \omega(E^*)$ . For all but the lightest nuclei, the state density forms a quasi continuum as long as the excitation energy  $E^*$  is greater than the binding energy of a nucleon. This “high level density” allows for statistical treatments of reactions, in which it is the value of  $\omega(E^*)$  associated with a given decay path that controls the probability of that decay. Not surprisingly, the entropy (the measure of the density of states that is extensive in macroscopic systems) and the temperature (the inverse of the rate of increase of the extensive measure of the density of states, i.e.,  $S$ , with excitation energy) turn out to be useful concepts in explaining the competition between decay channels of an excited compound nucleus, including the fission channel(s), by making use of transition-state theory. This theory was developed by a collaboration between Ewing and Wigner in the 1930s. It is perhaps only from the unique perspective of the nuclear chemist that the utility of this theory to treat both chemical and nuclear reaction rates can be appreciated.

These correlated many-body systems can also be viewed as isolated drops of matter, which, if uncharged, could be infinite. Reaction studies have been called upon to explore the equation of state (EoS) of nuclear matter and to extract any phase transitions that punctuate the phase diagram (► Fig. 3.3). An equation of state is humankind's attempt to interrelate the variable set of thermodynamics, the absolute minimum set required to describe the macroscopic state of a system. Nuclei, being two-component systems, have a “chemical composition” sector (with chemical potentials and numbers of each as the variables, with one or the other chosen as independent), as well as a “mechanical” sector ( $P, V$ ) and a “thermal” sector ( $T, S$ ). Reaction data have been able to place rather tight constraints on the incompressibility of symmetric nuclear matter.

The isothermal incompressibility (the inverse of the compressibility) of an ideal gas is  $K = -(V)(dP/dV)_T = P$ . It is the equivalent science (although general interest is in the adiabatic compressibility) for nuclear systems that is sought. Insight into how this incompressibility changes with neutron–proton asymmetry is just now becoming available. It is this part of the EoS that dictates the behavior of supernovae, the events leading to neutron star formation, and the structure of such stars.

■ Fig. 3.3

The nuclear temperature–density phase diagram, indicating the nuclear landscape now available for reaction studies. The dotted trajectory shows the stepwise evolution of an energetic nuclear collision, in steps of about  $1 \times 10^{-23}$  s (Adapted from Mueller and Serot 1995)



Phase transitions are the delimiting punctuation of the EoS of any matter. One of the great successes of recent nuclear reaction studies has been to elucidate this punctuation, in particular, the nuclear analog of a liquid–gas phase transition (► Fig. 3.3).

As mentioned above, the perspective of this chapter is that of a nuclear system composed of neutrons and protons. The subnuclear aspects of the field are not addressed, for example, the origin of the nucleon–nucleon force and spin, quark–gluon degrees of freedom, and weak–interaction physics. For an overview of these subjects, see (NRC 1999).

## 3.2 Basic Concepts

In simplest terms, a nuclear reaction can be defined as a binary collision that alters the nucleon–nucleon associations, just as a chemical reaction is one that alters atom–atom associations. This change in association can produce different nuclei (via the exchange of nucleons or fusion) or can simply excite the nuclei (different correlations within the nucleus that no longer correspond to the ground state.) The latter type of reaction is called *inelastic* excitation. The former type might, or might not, proceed through an intermediate.

The case in which an intermediate state is formed can be written as



where the reactants  $A$  and  $a$  are the target and projectile that form an excited intermediate species  $C^*$ , or *composite nucleus*. The intermediate usually decays into a binary exit channel indicated by the product nuclei  $b$  and  $B$ . If the reaction loses all recollection of the entrance channel aside from quantities fixed by conservation laws (energy and angular momentum), the

intermediate composite is called a *compound nucleus* (CN), (• Fig. 3.4). In this case, exit-channel products are formed via statistical decay on a time scale longer than  $\sim 10^{-21}$  s, a time commensurate with those that characterize either collective nuclear motion (rotation or vibration) or nucleon transit across a nucleus. At the other extreme, *direct reactions* occur on a much shorter time scale ( $\sim 10^{-23}$  s), effectively bypassing the composite nucleus state. In reality, there is a continuum of time-dependent processes between compound and direct reactions. Intellectually, this continuum of mechanisms can be organized as viewing each step proceeding toward a CN as a fixed “generation” of nucleon-nucleon collisions. In a simple direct reaction the final state – right-hand side of • Eq. (3.1) – is reached in the first step. Several steps are required to dissipate entrance channel energy and disperse it statistically among all the nucleon degrees of freedom. In the language of statistical mechanics, the CN is the case where the allowed phase space (that piece of the many-body  $6N$  dimensional phase space allowed by conservation laws) has been fully sampled. The kinetic process by which this happens, organized by collision generation, is called the Multistep Compound Model, a model developed by Feshbach, Kerman, and Koonin (Feshbach et al. 1980), and often called FKK for short. The FKK codes commonly in use today are: EMPIRE, TALYS, and GNASH, which can be found on the Web.

In principle, the products of a nuclear reaction can be any species permitted by conservation laws. In practice, direct reaction final channels will be strong if they possess substantial overlap with those of the initial state. Similarly, if the reaction proceeds all the way to a CN, strong channels will be those that capture large portions of the available phase space. Compound nucleus wave functions are intractable objects. This, coupled with the myriad of equally complex final states, allows a statistical analysis to be employed. Even so, the full  $6N$  dimensional phase space is far too large to cope with and so insight must be used to calculate the phase space area of relevant parts (e.g., the part of phase space well described by two large clumps of matter, rather than one, will be proportional to the fission yield.)

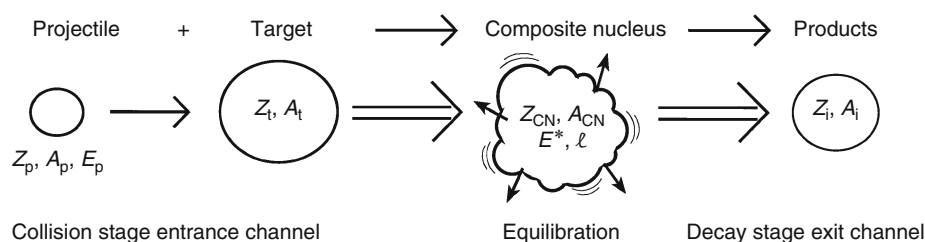
### 3.2.1 Shorthand Notation for Nuclear Reactions

The following shorthand notation is frequently employed:

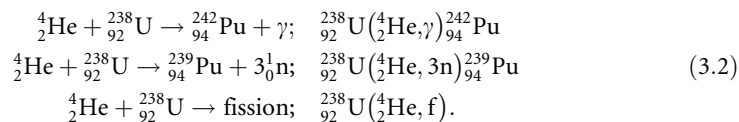
target (projectile, light products) heavy products, or  
 $A(a, b)B$ .

• Fig. 3.4

**Nomenclature for the time evolution of a nuclear reaction in which a composite nucleus is produced and then forms product nuclei**

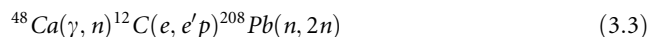


Note that the “products” are in plural; however, either can indicate a single particle. Typical examples, presented in both long- and shorthand notations, for reactions between  ${}^4\text{He}$  projectiles and a  ${}^{238}\text{U}$  target are:



Note that “one-way” arrows are used in the standard longhand reaction notation. Reaction studies are usually “one-way” exercises, i.e., equilibrium between reactants and products is not achieved. (Notable exceptions are bombs and the National Ignition Facility – NIF). On the other hand, Nature does achieve equilibrium (for many reactions) in the core of stars.

Using the shorthand notation, examples of photon capture, electron knockout and neutron-induced reactions are, respectively:



### 3.2.2 Mass-Energy Conservation: The Q-Value

The most fundamental constraint on any nuclear reaction is established by mass-energy ( $E = Mc^2$ ) conservation. The **Q-value** for a reaction is the rest-mass energy difference between the reacting nuclei and the product nuclei:

$$Q = \sum M_0(\text{reactants})c^2 - \sum M_0(\text{products})c^2, \quad (3.4)$$

where  $M_0$  is the rest mass of the nucleus. Nuclear mass-energy is tabulated in terms of *mass excess*  $\Delta$ , which is often given in units of energy rather than mass (see [Sect. 11.6](#) of the Appendix of this Volume, where it is denoted by  $D$ ):

$$\Delta = (M_0 - A \text{ u})c^2, \quad (3.5)$$

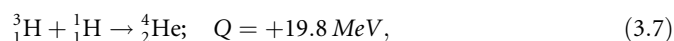
where  $A$  is the mass number and  $\text{u}$  is the *unified atomic mass unit* ( $1 \text{ u } c^2 = 931.494 \text{ MeV}$ ). The Q-value can be rewritten as

$$Q = [\Delta(\text{projectile}) + \Delta(\text{target})] - \sum \Delta(\text{products}) \quad (3.6)$$

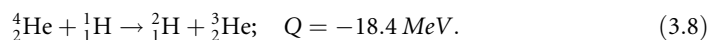
Sources of mass-excess values, as well as reaction and structure data, can be found in NNDC (2010). If the rest mass of the reactants exceeds that of the products, the reaction is *exothermic* ( $Q > 0$ ) and there is no energy threshold for the reaction. If  $Q$  is negative, the reaction is *endothermic* and projectile kinetic energy must be converted into rest-mass energy to compensate for this deficiency. Elastic scattering is defined by  $Q = 0$ .

In terms of writing energy-balanced (chemical-like) equations, Q-values correspond to product-side energy release. This is opposite to the sign convention for enthalpies, which can be viewed as reactant-side energy inputs. (Thus a negative enthalpy corresponds to a positive Q-value, i.e., the energy released in the reaction.) In a chemical reaction, the energy change comes from alteration of the atom associations, while in a nuclear reaction, the energy release comes from a change in the associations (i.e., correlations) at the nucleon level.

Two examples of concern in Big Bang nucleosynthesis, also discussed in [Chap. 12](#) of Vol. 2, are:



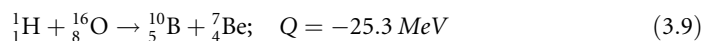




The first reaction (with a positive  $Q$ -value) is an important pathway in element formation; the second (with a negative  $Q$ -value) hinders destruction of  ${}^4\text{He}$  in stellar environments.

All  $(n, \gamma)$  reactions (called *neutron capture*) on stable target nuclei are exothermic, as are all  $(p, \gamma)$  reactions on stable nuclei. These  $Q$ -values are no more than the release of energy corresponding to the binding energy of that nucleon. One can think of this energy as the energy difference between an unbound nucleon at zero energy and the Fermi energy, which while approximately 30 MeV above the bottom of a one-body potential is, by definition, 1  $B_N$  below zero. The condition  $B_N = 0$  defines the drip lines, i.e., the limits of nuclear stability with respect to the strong force.

Charged-particle reactions with heavier nuclei can have positive or negative  $Q$ -values. If the collective binding energies of the products are greater than that of the reactants, as it would be the case if the products were closer to the peak in the binding-energy curve than the reactants, the  $Q$ -value will be positive. Negative  $Q$ -values occur, for example, when nuclei on the leading edge of the binding energy curve, such as  ${}^{12}\text{C}$  and  ${}^{16}\text{O}$ , are broken up into still lighter nuclei or when nuclei heavier than Fe fuse to build a heavier nucleus. Cosmic-ray-induced reactions that occur in the atmosphere, relevant to Li, Be, and B nucleosynthesis in nature and also to space travel, are examples of reactions with negative  $Q$ -values. (Such reactions are perhaps the principal impediment to long-duration space travel by humans.)



In reactions involving complex nuclei, two important quantities related to the  $Q$ -value, and also to the incident beam energy, are the excitation energy  $E^*$  (or equivalently  $U$ ) and the threshold energy  $E_{th}$ . The *excitation energy* is the excess energy deposited in the product nucleus (► Fig. 3.5). For excitation energies below one  $B_N$ , the discretized nature of  $E^*$  is important.

The *threshold energy* is the minimum projectile energy required to form the product nucleus in its ground state. Compound nucleus formation provides a simple example of this concept: target (t) + projectile (p)  $\rightarrow$  CN. In this case, energy and linear momentum conservation require (in the nonrelativistic limit):

$$\text{mass-energy:} \quad \Delta_t + \Delta_p + E_p = \Delta_{CN} + E_{CN} + E^*, \quad (3.10)$$

$$\text{linear momentum:} \quad p_p = \sqrt{2M_p E_p} = \sqrt{2M_{CN} E_{CN}} = p_{CN}, \quad (3.11)$$

$$\text{which gives:} \quad E^* = (A_t/A_{CN}) E_p + Q. \quad (3.12)$$

$$\text{Since when:} \quad E^* = 0, E_p = E_{th}, \text{ then} \quad (3.13)$$

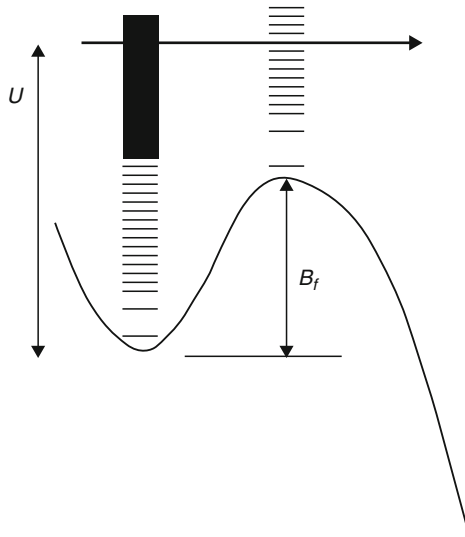
$$E_{th} = (A_{CN}/A_t)(-Q). \quad (3.14)$$

If  $Q$  is positive, there is no energetic threshold to limit the reaction. If  $Q$  is negative, energy in excess of the  $Q$ -value must be supplied to account for the center-of-mass motion of the composite nucleus. Equations for the situation in which two products are formed can be found in standard texts (e.g., Krane 1988; Cottingham and Greenwood 2001).

Under common reaction conditions during the first 50 years of nuclear reaction studies, the lighter of the two partners was the projectile incident on a heavier target at rest. However, with the advent of modern heavy-ion accelerators, this situation can now be interchanged, permitting the study of systems in which a heavy projectile is used to bombard a lighter target (*reverse*

■ Fig. 3.5

Schematic description of the increasing density of nuclear levels as the excitation energy  $U$  increases above the minimum in the potential energy (ground state). The abscissa in this plot is a deformation coordinate that represents the “reaction coordinate” and shows the change in level density as the system follows a one-dimensional path toward one possible decay mode, i.e., fission. The lowest density of states along this path is indicated for the height of the fission barrier  $B_f$ . In this figure  $U$  is used for the excitation energy. This is consistent with the use of  $U$  in thermodynamics to indicate the internal energy. The excitation energy  $E^*$  is the energy above the ground-state energy (mass) and in this example is indicated by the horizontal arrow



*kinematics*). This situation provides a unique experimental environment in which the reaction products are focused forward. Most recently, it has become possible to create reactions between colliding beams of heavy nuclei (e.g., Au + Au), thereby retrieving the available energy lost to center-of-mass motion in conventional fixed-target collisions.

### 3.2.3 The Nuclear Potential Energy: Coulomb Barrier Effects

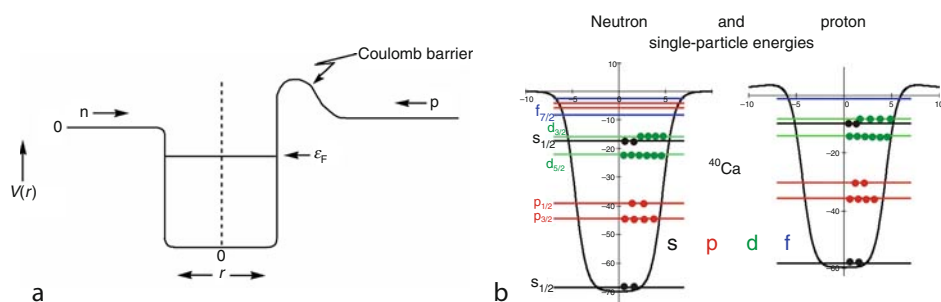
A second energetic factor, independent of the  $Q$ -value, is imposed by the *nuclear potential energy*, which summarizes the respective forces at play in atomic nuclei. As shown in [Fig. 3.6](#), the potential energy for a complex nucleus is the sum of

1. A *central attractive well* created by the strong nuclear force acting at short range on the constituent neutrons and protons, and
2. A *repulsive Coulomb interaction* of long range acting between the positive charges of the target and projectile.

The saturated, short-ranged nature of the attractive nucleon-nucleon interaction creates an approximately uniform *mean field* inside the nucleus, giving rise to a nearly flat behavior of the nuclear potential. Near the nuclear periphery, the long-range Coulomb repulsive interaction overpowers the short-range nuclear attraction, giving rise to the *Coulomb barrier* and

■ Fig. 3.6

(a) A schematic representation of the nuclear potential energy as a function of the distance from the center of a complex nucleus is shown. Neutrons (*left*) do not experience Coulomb repulsion, as do protons (*right*). The Fermi energy level is indicated by  $\epsilon_F$ . (b) A potential plot to scale for neutrons and protons in  $^{40}\text{Ca}$



a subsequent decrease in the potential at large distances according to the  $1/r$  law. The actual nuclear potential energy will be multidimensional if spherical symmetry is broken by the ground state being deformed, as always happens at midshell, or when fission-like phenomena are being treated.

Using Gauss' Law and assuming that the charge is uniformly distributed within a sphere of radius  $R_C$ , the Coulomb potential (i.e., electric potential energy) has the following form:

$$V_C(r) = \frac{Z_p Z_t e^2}{r} = \frac{1.44 Z_p Z_t}{r} \text{ MeVfm}; \quad r \geq R_C$$

$$V_C(r) = \frac{Z_p Z_t e^2}{2R_C} \left( 3 - \frac{r^2}{R_C^2} \right); \quad r < R_C. \quad (3.15)$$

Here  $Z_p$  and  $Z_t$  are the respective charges of the projectile and target nuclei and  $r$  is the separation distance between the centers of charge of the colliding nuclei.

The Coulomb barrier  $B_C^{\text{cm}}$  (in the center of mass) can be estimated as the interaction of nearly touching spheres, i.e.,  $B_C^{\text{cm}} = V_C(R_C)$ , where  $R_C = r_C(A_p^{1/3} + A_t^{1/3})$ . Empirical studies suggest a value of  $r_C \approx 1.4\text{--}1.6$  fm, also discussed in ▶ Sect. 2.2.3.1 of Chap. 2 in this volume. As with the  $Q$ -value, it is necessary to correct for center-of-mass motion, so that in the laboratory frame, the projectile energy required to surmount the Coulomb barrier is

$$B_C^{\text{lab}} = (A_{CN}/A_t) B_C^{\text{cm}}. \quad (3.16)$$

For charged particles with kinetic energies below the Coulomb barrier, the projectile usually elastically scatters from the target (discussion of Coulomb excitation below), leaving the reactants unchanged. Once the relative kinetic energy of the colliding pair becomes comparable to the Coulomb barrier, the projectile can classically penetrate into the attractive nuclear potential and produce a nuclear reaction. (Barrier penetration with lab energies below  $B_C^{\text{lab}}$  can occur but the probability is low.) This energy can be supplied by particle accelerators or in nature by either the high temperatures achieved in the core of a star or by the various cosmic accelerators that generate the high-energy nuclei found in cosmic rays. The Coulomb barrier is the energetic factor that determines the rate of reactions between charged nuclei at low energy.

This barrier also controls the decay rate for channels for which a charge separation is generated. Examples of the latter are all decay channels of an excited CN producing charged particles in the exit channel, ground-state (radioactive) decay via alpha-particle emission and fission.

Reactions between charged species first become probable when the projectile kinetic energy increases to values near the Coulomb barrier energy, permitting the tails of the nuclear matter distributions to overlap, [Fig. 3.7](#). Because of the diffuse tail of the matter distribution and quantum penetration, it is possible for reactions to occur below the nominal Coulomb barrier. Most often, such reactions involve Coulomb excitation or the transfer of one or a few nucleons at the nuclear surface. However, more complex reactions can occur, including amalgamation of target and projectile, although with low probability. As the overlap between the two nuclear matter distributions increases, the probability for nuclear reactions involving many or all nucleons becomes increasingly probable.

### 3.2.4 Angular Momentum Effects: The Centrifugal Barrier

A second repulsive energetic factor is due to the orbital angular momentum associated with noncentral collisions. As shown in [Fig. 3.8](#), initial projectile trajectories can be characterized semiclassically in terms of an *impact parameter*  $b$ , which is the distance between a given trajectory and one that passes through the center of the target.

The orbital angular momentum  $\ell\hbar$  is quantized, so that for a projectile of mass  $m$  and velocity  $v$ ,

$$\ell\hbar = (mv)b, \quad (3.17)$$

For the case of two colliding spheres with sharp surfaces, the maximum value of the impact parameter is determined by the touching condition

$$b_{\max} = R_p + R_t, \quad (3.18)$$

where  $R_p$  and  $R_t$  are the respective radii of projectile and target nuclei as shown in the left panel of [Fig. 3.9](#).

In a classical geometrical model, the maximum angular momentum for the collision of objects with a sharp surface is then,

$$\ell_{\max} \hbar = mvb_{\max} = mv(R_p + R_t) = mvr_0(A_p^{1/3} + A_t^{1/3}). \quad (3.19)$$

**Fig. 3.7**

Schematic picture of the increasing density overlap between projectile  $p$  and target  $t$  as two complex nuclei pass by one another

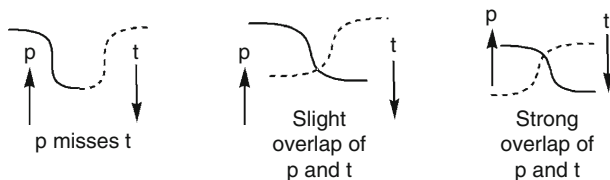


Fig. 3.8

Generation of angular momentum  $\ell\hbar$  for projectiles with different impact parameters  $b$ . Each annular ring corresponds to the area defined by a given impact-parameter range and its associated  $\ell$ -value. The indicated direction of rotation corresponds to “glancing” collisions represented by the two upper projectile trajectories. The middle trajectory leads to a “head-on” collision without angular momentum generation

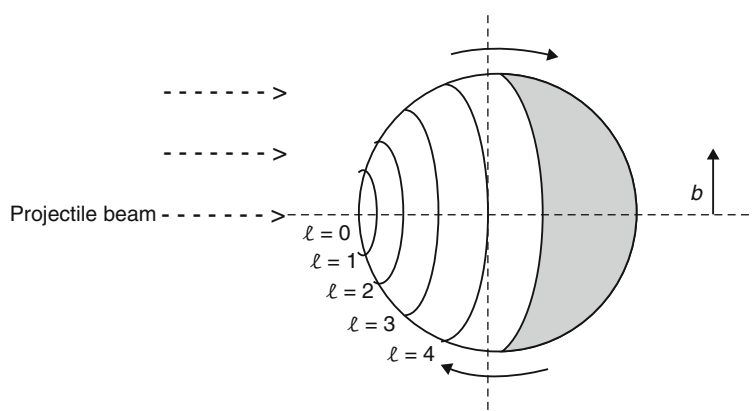
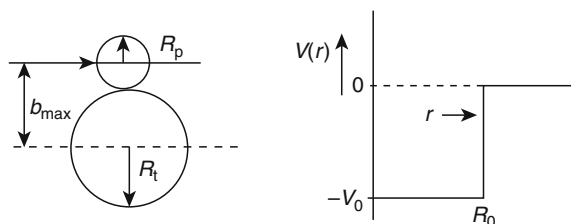


Fig. 3.9

Left: Touching-spheres model of a nuclear collision. Right: Square-well nuclear potential, corresponding to a nucleus with a sharp surface



The amount of energy tied up in *rotational energy*  $E_{\text{rot}}$  depends on the impact parameter and constitutes a *centrifugal barrier*,

$$E_{\text{rot}}(\ell) = \frac{\hbar^2 \ell(\ell+1)}{2\mu r^2} = \frac{(\hbar c)^2 \ell(\ell+1)}{2 \left( \frac{A_p A_t}{A_p + A_t} \right) u r^2}; \quad \ell = 0, 1, 2 \dots \ell_{\text{max}}, \quad (3.20)$$

where  $\mu$  is the reduced mass of the system, proportional to  $A_p A_t / (A_p + A_t)$ . (The constant  $\hbar c = 197.3 \text{ MeV fm}$  simplifies calculations when combined with the numerical value of  $u = 931.5 \text{ MeV}/c^2$ ).

Three additional points should be noted about this “barrier.” First, it drops off with distance much faster than the Coulomb barrier, i.e.,  $1/r^2$  versus  $1/r$ . Second, it is not the result of a real interaction. Rather, it can be viewed as removing that fraction of the energy from the

entrance channel that must be “spent” in angular momentum conservation and is thus not available for a reaction. In the standard language of chemistry, the relative separation is the reaction coordinate. The energy tied up in conserving angular momentum is not available to advance the reaction coordinate. Finally, it is this term in the expression for the energy that when put into the quantum mechanics (one-body) problem forces the wave functions to go to zero at the origin. The combined effects of the Coulomb and centrifugal barriers form independent constraints on the probability for a nuclear reaction.

The angular momentum involved in a reaction has important consequences, ranging from nuclear spectroscopic studies at low-angular momentum to the rotational instabilities that lead to fission, rotating dinuclear configurations (▶ Sect. 3.4.2), and for populating the highly deformed local minima responsible for fission isomers and super-deformed nuclei. For example, in a  $^{238}\text{U} + ^{238}\text{U}$  collision, angular momenta up to  $\ell_{\text{max}}\hbar \approx 1,000\hbar$  are possible. However, for values above  $\ell\hbar \approx 80\text{--}100\hbar$  the composite system becomes rotationally unstable and cannot fuse. Thus all of the cross section associated with angular momentum above this stability limit is associated with reaction channels other than CN formation.

### 3.2.5 Summary of Energetic Factors in Nuclear Reactions and the Separation of Thermodynamic and Kinetic Factors

To form a composite nucleus, the threshold energy must be exceeded and the available energy must exceed the combined Coulomb and centrifugal barriers for the reaction probability to be appreciable. The threshold energy is imposed by mass-energy conservation and is important only for negative  $Q$ -values. The Coulomb barrier applies only to charged-particle reactions. The centrifugal barrier is not a fundamental constraint since  $\ell = 0$  is always possible. (Also recall that  $\ell$  is not a good quantum number if the potential is not spherically symmetric. This means that  $\ell$ -waves can mix in such cases. However, as parity is a good quantum number, even values of  $\ell$  mix with even and odd with odd.) As a general rule, the Coulomb barrier dominates for charged-particle-induced reactions, except for some cases where light nuclei are involved. For  $(n,\gamma)$  reactions on stable nuclei, the  $Q$ -value is always positive and the Coulomb barrier is zero, so only the centrifugal barrier constraint is relevant.

If the nuclei on either side of the reaction can exist only in one (i.e., the ground) or a few (as in the products of a direct reaction) states, the entropy of the participants is small as is the temperature  $T$ . Under these conditions, a thermodynamic discussion reduces to one of enthalpy (as the “ $SdT$ ” term, i.e., the thermal term, in the free energies is tiny.) The  $Q$ -value represents the negative of the enthalpy, so a positive  $Q$ -value represents a spontaneous reaction. At  $T = 0$ , there are only two possible values of the degree of reaction: 0 (i.e., none) or 1 (all). So given enough time, something thermodynamics cannot give insight into, a positive  $Q$ -value will yield 100% products. (An energetically downhill reaction at equilibrium will yield 100% products at  $T = 0$ , a case realized in simple radioactive decay.) The barriers (both Coulomb and centrifugal) are kinetic factors. They do not influence ultimate equilibrium constants but they do determine rates (in the same way that the height of a chemical transition state determines the rate of a chemical reaction).

With the exception of the case of stars, or perhaps ultimately earth-bound fusion reactors, rates rather than true equilibrium are the concern. (As the reverse reactions required for true equilibrium do not occur.) Thus the description of the decay of a CN is a kinetic model.

### 3.2.6 Cross Sections: An Introduction

The compound nucleus scenario described in the previous section provides a useful framework for discussing the probability for a nuclear reaction as characterized by its *cross section*. As long as the excitation energy is not so high that internal thermal equilibration is short circuited, one can separate the formation process from the decay. When this is the case, the reaction probability can be factored into two terms: (1) the total probability for the projectile and target to fuse (entrance channel), and (2) the individual probabilities for formation of each product nucleus (exit channel). The total cross section can be defined more precisely in terms of the difference between the incoming and outgoing flux of beam particles. For specific exit channels, the production cross section is the fraction of the total cross section that yields a given product nucleus. Such a description fits equally well for direct reactions, which do not involve the intermediate composite-nucleus step.

In estimating the total reaction probability, a simple geometric touching-spheres model provides a useful benchmark calculation (► Fig. 3.9). In this model, a reaction will occur if the impact parameter  $b$  is less than or equal to the sum of the nuclear radii. For larger values of  $b$  there will be no reaction. The cross-sectional area defined by this geometry leads to a classical or *geometric cross section*,

$$\sigma^{\text{geo}} = \pi b_{\text{max}}^2 = \pi(R_p + R_t)^2 = \pi r_0^2 (A_p^{1/3} + A_t^{1/3})^2; \quad r_0 \approx 1.40 - 1.60 \text{ fm}. \quad (3.21)$$

For medium-mass nuclei, this value has dimensions of order  $10^{-24} \text{ cm}^2$ , which defines the unit for cross sections, the *barn* (b); i.e.,

$$1 \text{ barn} \equiv 1.0 \times 10^{-24} \text{ cm}^2 = 100 \text{ fm}^2. \quad (3.22)$$

For projectile energies well above the threshold and/or Coulomb barrier, ► Eq. (3.21) serves as a good approximation for the *total reaction cross-section*,  $\sigma_R \approx \sigma^{\text{geo}}$ .

For *neutron-capture* ( $n, \gamma$ ) reactions at very low energies ( $\ll 1 \text{ MeV}$ ), microscopic effects come into play, leading to significantly enhanced cross sections. Since ( $n, \gamma$ ) reactions can proceed without threshold or Coulomb barrier limitations, reactions can occur at very low energies. More importantly, the wave nature of matter becomes the dominant factor. At very low energies (thermal, i.e., 300 K, energies correspond to an average kinetic energy of 0.025 eV) the neutron reduced *de Broglie wave length* ( $\lambda = \hbar/p = 1/k$ ) is much larger than the nuclear radius; i.e.,  $\lambda > R$ . The reduced de Broglie wave length is the reciprocal of the wave number  $\lambda = 1/k$ , where  $k = (2mE)^{1/2}/\hbar$ . Thus, for very low neutron energies, the values of  $\sigma_R$  can greatly exceed  $\sigma^{\text{geo}}$ .

Between the thermal and geometric extremes (i.e., between where the de Broglie wave length dominates and the width of the average state greatly exceeds the spacing between states) there is a resonance region where the cross section is characterized by sharp spikes at well-defined energies. All three of these regions are illustrated schematically in ► Fig. 3.10.

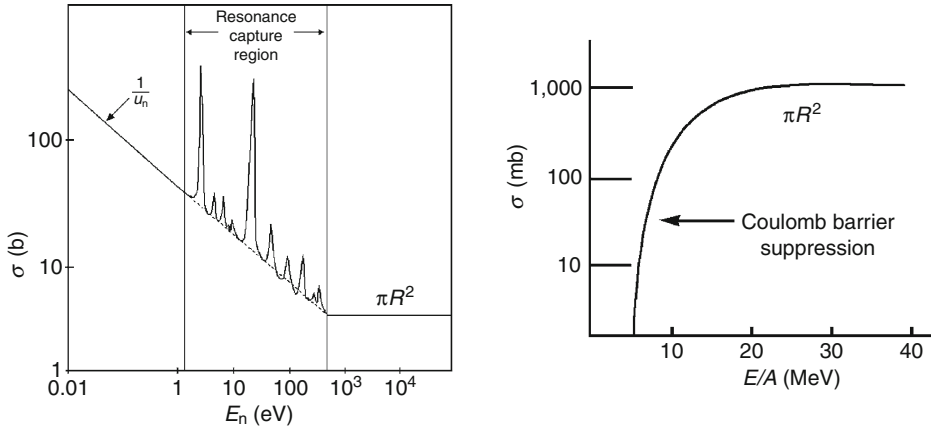
On the other hand, *charged-particle-induced reactions* at low energies are suppressed by the Coulomb barrier. To account for this effect, a simple modification of the form

$$\sigma_R = \sigma^{\text{geo}} (1 - B_C/E_p); \quad E_p \geq B_C \quad (3.23)$$

provides a good first approximation to the cross-section dependence on bombarding energy. By employing more sophisticated models that account for the diffuse nuclear surface and diffraction effects, a more quantitative description of the reaction cross section can be obtained.

Fig. 3.10

**Left:** Schematic representation of the excitation function for the capture of neutrons in a  $(n, \gamma)$  reaction. In this figure the velocity of the neutron is indicated by  $u_n$ . **Right:** Total cross section dependence on bombarding energy per nucleon for a charged-particle reaction



An important component of the reaction cross section is the relative distribution of angular momenta, or  $\ell$ -wave distribution, generated in a collision. Angular momentum affects the population of quantum states of a given spin in direct reactions and is also a major factor in generating rotating nuclei that stretch axially into highly deformed nuclear shapes (Janssens and Khoo 1991). Angular momentum also destabilizes nuclei toward fission, much as a high-charge content does. In the geometric model the angular momentum is given by  $\ell\hbar = m v b$  and  $\ell_{\max}\hbar = m v (R_p + R_t)$ , as shown in Fig. 3.8, and thus it is possible to partition the cross section by impact parameters,

$$\sigma_{\ell}^{\text{geo}} = \pi(b_{\ell+1}^2 - b_{\ell}^2) = \pi\lambda^2[(\ell+1)^2 - \ell^2] = \pi\lambda^2(2\ell+1). \quad (3.24)$$

By summing over all  $\ell$ -waves the total reaction cross section,  $\sigma_R^{\text{geo}}$ , is then given by

$$\sigma_R^{\text{geo}} = \pi\lambda^2 \sum_{\ell=0}^{\ell_{\max}} (2\ell+1) = \pi\lambda^2(\ell_{\max}+1)^2. \quad (3.25)$$

In the simple black-disk model described above, nuclear effects of the diffuse nuclear surface and the discrete (i.e., quantum) nature of the allowed nuclear structure have been ignored and it is assumed that nuclear matter is perfectly opaque. The *optical model* addresses these omissions and is the subject of the next major section. One of the major results of this model is the introduction of  $\ell$ -dependent *transmission coefficients*,  $T_{\ell}$ , where  $0 \leq T_{\ell} \leq 1$ . The reaction cross section then becomes

$$\sigma_R = \sum_{\ell} \sigma_{\ell} \pi\lambda^2 \sum_{\ell} (2\ell+1) T_{\ell}. \quad (3.26)$$

These transmission coefficients are then the probability that the target-projectile collision will penetrate the interaction barrier and produce a nuclear reaction. Thus as  $\ell$  increases,  $T_{\ell}$  decreases; that is,  $T_{\ell} = 1$  corresponds to complete absorption and  $T_{\ell} = 0$  to pure elastic scattering.



### 3.2.7 Cross Sections, Excitation Functions, and Angular Distributions

Experimentally, evidence for a target-projectile interaction can be gained from measuring the probability for formation of the products that populate the various exit channels. This information then serves as the basis for interpretation of the reaction mechanism through which a nuclear collision proceeds. It may also provide essential data for nuclear astrophysics, as described in [▶ Chap. 12](#) of Vol. 2, and for evaluating and implementing nuclear applications, discussed in [▶ Chaps. 38](#) and [▶ 39](#) of Vol. 4).

The total reaction cross section is the sum of all possible reaction channels:  $\sigma_R = \sum_b \sigma(a, b)$ . Exit channels may involve only a single heavy nuclear product, as in the case of  $(n, \gamma)$ , reactions two fragments (as in fission) or even multiple fragments, as in multifragmentation. By measuring all possible exit channels,  $\sigma_R$  can be determined. Alternatively,  $\sigma_R$  can be measured with beam-attenuation measurements by measuring the rates [particle/s] of the beam reaching a detector with the target in and with it out (see the Addendum).

Measurements of production cross sections are performed with a wide range of both radiochemical and direct counter techniques. Historically, radiochemical techniques were particularly useful for measuring heavy residues, for which discrete  $Z$  and  $A$  identification are difficult to determine with nuclear particle detectors in reactions with normal kinematics. However, with the availability of very heavy-ion beams and the widespread use of reverse kinematics, the measurement of mass ( $d\sigma_A/dA$ ), charge ( $d\sigma_Z/dZ$ ), and isotope ( $d\sigma_Z/d\sigma_A/dAdZ$ ) distributions from direct counter techniques are now routinely done. For heavy residues, these values are frequently summarized graphically in terms of an *excitation function*, or cross section as a function of projectile energy, as in [▶ Fig. 3.11](#). Extensive listings of production cross sections are maintained in several databases (IAEA 2010; NEA 2010; NNDC 2010; RND 2003).

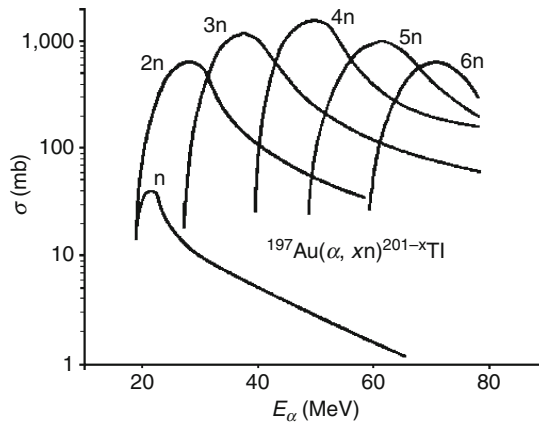
In conducting direct counter experiments, the emission of reaction products over the full  $4\pi$  of solid angle  $(\theta, \phi)$  must be taken into account, as well as the transformation of laboratory data into the center-of-mass system (Krane 1988). Thus, measurements of the *angular distribution*, i.e., differential cross section as a function of angle  $d\sigma(\theta, \phi)/d\Omega$ , must be made. In the absence of spin-polarized targets or projectiles, the cross section is independent of azimuthal angle  $\phi$ . In this case, the angular distribution is characterized by the single differential cross section,  $d\sigma(\theta)/d\Omega$ , where  $\Omega$  is the solid angle into which the particles are emitted. The production cross section is then given by

$$\sigma(a, b) = \int_0^{2\pi} \int_0^\pi \frac{d\sigma(\theta, \phi)}{d\Omega} d\Omega = 2\pi \int_0^\pi \frac{d\sigma(\theta)}{d\Omega} \sin\theta d\theta. \quad (3.27)$$

For statistical decay of a composite nucleus with no angular momentum, particles are emitted isotropically; that is,  $d\sigma(\theta)/d\Omega$  is independent of angle in the center-of-mass system. Thus,  $d\sigma(\theta)/d\Omega = \text{constant}$  or  $d\sigma(\theta)/d\theta \propto \sin\theta$ . If the composite nucleus is formed in a state of high angular momentum with the axis of rotation oriented perpendicular to the beam direction (i.e., from an ensemble of reactions, the angular momenta are uniformly distributed in a plane perpendicular to the beam), as in the approximate case in heavy-ion reactions, then one observes strong forward-backward peaking, reaching a limiting value of  $d\sigma(\theta)/d\Omega$ ,  $\propto 1/\sin\theta$  or  $d\sigma(\theta)/d\theta = \text{constant}$ . Schematic angular distributions for these two extremes are shown in [▶ Fig. 3.12](#).

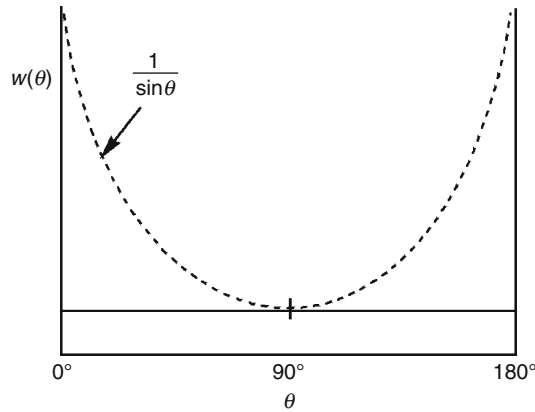
■ Fig. 3.11

Excitation function for the  $^{197}\text{Au}(^4\text{He}, xn)^{201-x}\text{Tl}$  reaction (Lanzafame and Blann 1970)



■ Fig. 3.12

Schematic angular distributions for particle emission from an equilibrated hot nucleus. Solid line is for a system with no angular momentum and dashed line is an upper limit for very high angular momentum



On the other hand, for direct reactions, the projectile-like products tend to be focused in the direction of the incident beam momentum vector. Depending on the quantum state, collision energy and time scale, forward peaking or peaking at specific angles will be observed. Thus, angular distributions serve as key indicators of the degree of equilibration achieved in a reaction, as well as providing a means of evaluating the reaction mechanism and imparted angular momentum.

One of the most sensitive tests of any nuclear reaction model is its success in reproducing absolute doubly differential cross sections  $d^2\sigma/d\Omega dE$ . In order to obtain the differential cross section for a given exit channel, it is necessary to integrate over the full kinetic energy distribution of the emitted particles at a specific angle,

$$\frac{d\sigma(\theta)}{d\Omega} = \int_0^\infty \frac{d^2\sigma(\theta, E)}{d\Omega dE} dE. \quad (3.28)$$

It is the kinetic energy distribution as a function of angle that reveals the physics content of a nuclear reaction most transparently. For a fully equilibrated CN, the spectra of evaporated light particles are Maxwellian in shape and unchanging in angle in the center-of-mass system. The spectra of charged particles are suppressed at low energies by the Coulomb barrier. Two-body direct reactions exhibit discrete spectral lines or resonances, depending on the nuclear structure sampled in the collision. The two-body (simple momentum balance) scenario also produces a good first-order description of fission, yielding Gaussian-like fragment energy spectra resulting from highly stretched breakup configurations.

### 3.2.8 Cross-Section Measurements

Determination of the cross section for a nuclear reaction product requires measurement of the *reaction rate*,  $R$  = number of events/unit time. As in any two-body collision (second-order rate process), the rate is the product of a target-projectile collision factor  $cn_p n_t$  and the “probability”  $\sigma$  that if a collision occurs, a specific product will be formed, i.e.,

$$\frac{dN(a, b)}{dt} = R(a, b) = cn_p n_t \sigma(a, b), \quad (3.29)$$

where  $c$  is a coefficient and the dimensions of  $n_p n_t$  are defined by the geometry of the experiment. Three cases are of general interest:

1. Accelerator-based bombardments in which a beam of particles  $n_p$  is incident on a planar target.
2. Nuclear reactors, where a gas of neutrons permeates  $n_t$  target nuclei.
3. Stellar interiors, where the reactants act as two interacting gases.

Practical aspects of cross-section calculations are discussed in the Addendum at the end of the chapter.

## 3.3 Scattering Theory

The presentation in the preceding section is meant to give a general overview of relevant concepts needed to describe nuclear reactions. In this section a treatment of quantum scattering is presented. This presentation is meant to facilitate a comparison between various types of scattering and to link nuclear reactions to structure. Additional background on scattering theory can be found in (Bertulani 2009).

### 3.3.1 Preliminaries

Before dealing with the scattering problem, the quantum objects under study should be considered. If the neutron and proton constituents of the nucleus were noninteracting, self-bound nuclei would not exist. One might posit that the binding energy is the sum of attractive

two-body interactions, all  $A(A - 1)/2$  of them. This amounts to making two assumptions: (1) that neutrons and protons are the only constituents in nuclei, i.e., nucleons are elementary particles and (2) that the interaction is *pair-wise additive*. The former assumption is formally incorrect, but not bad when the available energy is less than the mass of the pion, the lightest field particle that mediates the residual strong force (nuclear force). The second assumption is also likely wrong. Most nucleon-based descriptions of the residual strong force include 3-body forces between nucleons, but the origin of these – beyond *pair-wise additive* contributions – is unclear. Such interaction terms could come from the fact that nucleons are not truly elementary and the employed degrees of freedom (DoF), those of the nucleons, is an incomplete set. (Axilrod and Teller 1943 first introduced 3-body forces in an attempt to explain the crystal structure of solid Ar as a patch when they simplified the many-body problem by dropping all of the degrees of freedom associated with the electrons and retaining only those associated with the nuclear positions. Their assumption being that, if they could have solved the problem employing all degrees of freedom, a 3-body force would not be needed.) However, because the field-mediating bosons of Quantum Chromodynamics do interact with one another, while they do not in Quantum Electrodynamics, pair-wise additivity would not be expected in the former. Whatever the reason, nucleon-based theories require 3-body terms (see also [Chap. 2](#) in this Volume).

High-energy electron reaction studies measuring  $(e,e'p)$  cross sections have shown that only 70–80% of the protons participate in independent-particle motion of the type imagined in one-body potential models. This low “occupancy” of one-body states is caused by strong correlations within the nucleus. These correlations are primarily between pairs of nucleons, but  $\alpha$ -particle clustering, sometimes called “quarteting,” in any low-density region also suppresses one-body behavior. Nucleons are somewhat different objects inside and outside a nucleus, as they effectively lose 0.8% of their mass, i.e., the binding energy, when transported inside a nucleus. Often, the term “dressed” is used to describe nucleons in the nucleus.

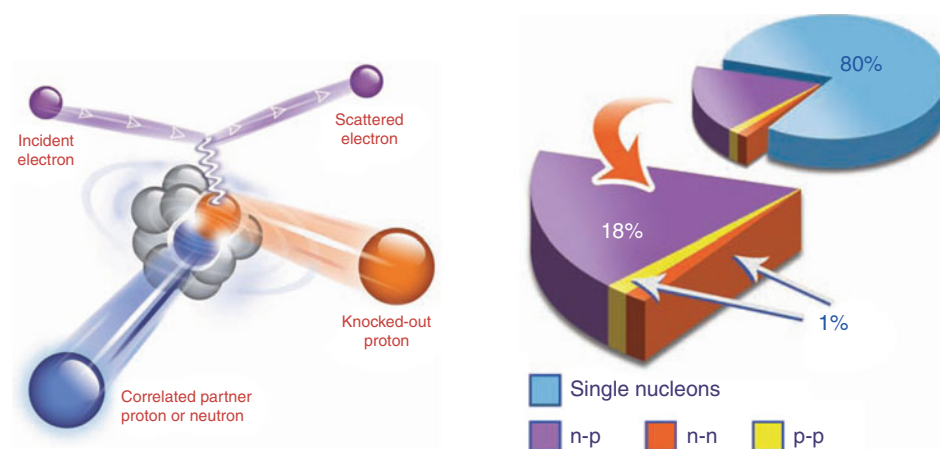
Very recent electron scattering studies using two-nucleon knockout reactions  $(e,e'pp)$  and  $(e,e'pn)$ , have shed considerable light on these in-medium correlations (Subedi et al. 2008). This work showed that the overwhelming strong pair correlations are between neutrons and protons with large relative momenta and small center-of-mass (CM) momenta ([Fig. 3.13](#)). Large relative momenta are expected due to the rather hard core of the nucleon-nucleon interaction, but the tensor force undoubtedly plays a role and helps distinguish like-nucleon versus different-nucleon correlations. The tensor force arises because the interaction between nucleons depends on the relative orientation of their spins with respect to their relative spatial vectors (see [Chap. 2](#) in this Volume).

Due to the Pauli principle, only n-p pairs can have their spins aligned and otherwise have the same quantum numbers. These pairs are referred to as short-range correlated (SRC) pairs and their presence strongly affects the properties of cold, dense nuclear matter, such as that found in neutron stars. This nucleon-nucleon interaction is also required to explain the fact that the n-p spin triplet is bound (i.e., the deuteron) while the n-n and p-p, required singlets, are not. Consideration of n-p interactions is also essential to understand the evolution of the phenomenological spin-orbit interaction as a function of n/p asymmetry (Otsuka 2005), one of the most discussed topics in nuclear structure research today.

A focus on like-nucleon singlet (spin zero, i.e., BCS-like) pairing is warranted in an effort to explain the slight variation in mass responsible for the overwhelming dominance of even-even nuclei as well as explaining their ground-state spins. On the other hand, this myopic focus near the Fermi energy misses the source of the bulk of nuclear binding.

Fig. 3.13

The initial nucleon correlations as seen from a two-nucleon knockout experiment (*left*) are summarized in a pie chart on the right (Subedi et al. 2008)



Descriptions of nuclei based on realistic nucleon-nucleon interactions that include the effects mentioned above have, as of this time (2010), only been able to deal with nuclei with  $A < 12$  (Pieper et al. 2002). Above this mass number, various approximations are employed. Simplifying this many-body problem all the way down to independent particles moving in an overall potential is of great heuristic value and utility. (This utility does not extend to calculation of the total binding energy. For this, one needs to add a macroscopic correction to the total binding energy. In this macroscopic-microscopic approach, pioneered by Strutinsky (1967), it is the macroscopic part that captures the impact of nucleon-nucleon correlations far removed from the Fermi surface). The single-particle approximation leads to the one-body problem, i.e., the type solved for generating hydrogenic wave functions (in this case, a solitary  $e^-$  moving in a  $1/r$  potential.) The greatly simplified (“one-body”) potentials (one for neutrons and one for protons) are separately adjusted to explain phenomena that occur *near* the Fermi surfaces for neutrons and protons. In fact, to explain behavior away from the Fermi surfaces, the potential depths have to be made both energy-dependent and complex.

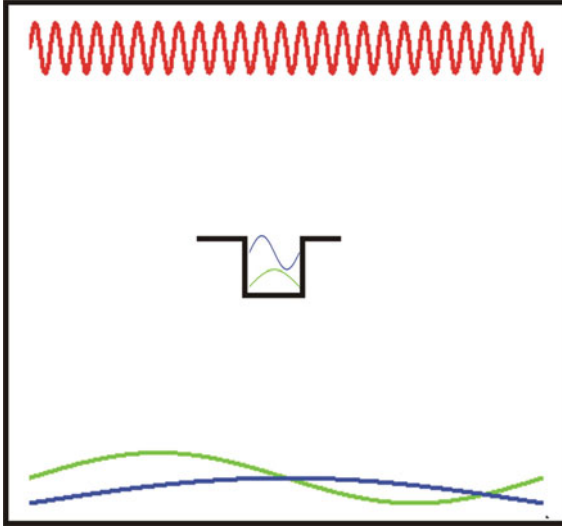
Consider a nucleon interacting with a (one-body) potential well formed by, at least, the  $A - 1$  interactions of this nucleon with the others. Now imagine that this potential is itself in a large box of dimensions much larger than the range of the nuclear force (Fig. 3.14). Considering only the short-ranged nuclear force, outside the well the potential is zero. The box, while large relative to nuclear dimensions, presents a boundary condition, so the box contains (in the absence of the internal potential) all the “particle-in-a box” states. The wave function with the lowest energy has no internal nodes; the more nodes - the higher the energy (eigenvalue).

As the depth and width of the internal potential is “dialed up,” these particle-in-a-box wave functions are modified – increasing the frequency in the region of the potential well and can even localize some of them entirely within the potential well. The latter, having no probability far-removed from the potential well, are the “bound-states.”

The presence of the attractive potential produces a positive phase shift  $\delta$  of the wave function at large distance, relative to the wave function without the potential (Fig. 3.15).

■ Fig. 3.14

**Nucleon potential in a box.** As the potential is made either deeper or wider, states are moved from ones quantized only by the box boundary conditions, essential free waves, to those confined to the central potential. The latter correspond to bound nuclear states



This phase shift is a direct consequence of the higher frequency within the range of the potential. As the potential is made either wider or deeper, states are “sucked” in (from the box) and are localized in the potential well. In the case of a one-dimensional square well of depth  $V$  and width  $L$ , the number of bound states for a particle of mass  $m$  is  $N = 1 + [(2mV)^{1/2}L/(\pi\hbar)]$  where the square brackets stand for the integer part. Every time the phase shift passes  $\pi$ , another one of the continuum (particle-in-a-box) states is “sucked” into the well. This phase shift, which plays a central role in scattering problems, records the asymptotic compression of the wave function, but the number of  $(1/2)$  oscillations (each producing a bound state) is lost. However, the number of bound states for each  $\ell$ ,  $N_\ell$ , can be recovered as it is encoded in the zero energy (i.e., threshold) phase shift,  $\delta_\ell(0) = N_\ell \pi$ . This is known as Levinson’s Theorem.

### 3.3.2 The Optical Model (OM)

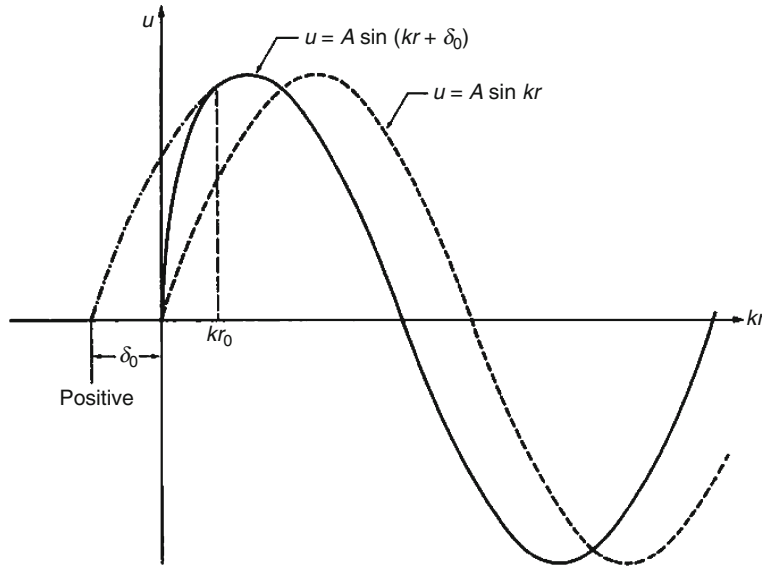
The interaction of a nucleon with a nucleus can be modeled if the potential is made complex (Buck et al. 1960; Hodgson 1967; Messiah 1958). The common form is

$$\begin{aligned}
 U(r, E) &= V(r, E) + iW(r, E) \\
 &= [-V_v(E)f(r, r_v, a_v) + 4a_s V_s(E)f'(r, r_s, a_s) + V_{so}(E)h(r, r_{so}, a_{so})(\ell\mathbf{s}) + V_c(r, a_c)] \\
 &\quad + i\{-W_v(E)f(r, r_v, a_v) + 4a_s W_s(E)f'(r, r_s, a_s) + W_{so}(E)h(r, r_{so}, a_{so})(\ell\mathbf{s})\}.
 \end{aligned} \tag{3.30}$$

where  $\ell\hbar$  and  $\mathbf{s}\hbar$  are angular momentum vectors and  $(\ell\mathbf{s})$  is the scalar product of the vectors  $\ell$  and  $\mathbf{s}$ .

Fig. 3.15

Illustration of the change in a wave function  $u$ , with an attractive potential and the associated phase shift



Note that the potential depends on the projectile center-of-mass energy  $E$  as well as radius  $r$ . The former accounts for the nonlocalities (and thus generates effective masses and spectroscopic factors, which are related to the occupancies of single-particle states).  $V$  and  $W$  are the real and imaginary parts of the potential, both of which have volume, surface, and spin-orbit-dependent components,  $V_v$ ,  $V_s$ , and  $V_{so}$ , respectively. (The spin-dependent term given above is appropriate for the scattering of spin  $1/2$  particles by spin 0 nuclei; for the scattering of particles of zero spin, there is no spin-dependent term, while for the scattering of particles of higher spin, more complex forms are required).  $V_c$  is the Coulomb potential, a term needed if the incident particle is charged. The refracting potential  $V$  elastically scatters the incident particles, and the absorbing potential  $W$  takes account of all the inelastic processes.

The unitless form factors (Fig. 3.16) are most often taken as

$$f(r, r_i, a_i) = \frac{1}{1 + \exp\left(\frac{r - R_i}{a_i}\right)}, \quad (3.31)$$

and

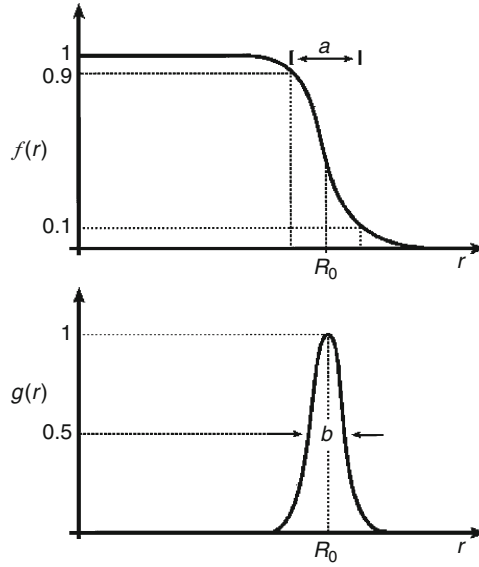
$$h(r, r_i, a_i) = -\frac{1}{2} \left( \frac{\hbar c}{m_\pi c^2} \right)^2 \frac{f'(r, r_i, a_i)}{r}. \quad (3.32)$$

Here  $f' = df/dr$ .

The nuclear radii are  $R_i = r_i A^{1/3}$  and the parameters  $a_i$  encode the diffuseness of the nuclear surface. The subscript  $(i)$  allows these constants to be different for the different terms in the potential. The spin-orbit form is analogous to the Thomas form for atoms. Relativistic treatments generate such a term, but do not provide insight into the strength or even its sign. The Coulomb potential can be taken to be that for uniformly charged spheres or calculated numerically assuming form factors for the density similar to that for the potential.

■ Fig. 3.16

Form factors of the OM for the real,  $f(r)$ , and imaginary,  $g(r) = -af'(r)$ , components



To calculate the observable cross sections for two particles interacting through the above potential, Schrödinger's equation must be solved,

$$\frac{\hbar^2}{2\mu} \nabla^2 \Psi + (E - V) \Psi = 0, \quad (3.33)$$

where the radial part of the kinetic energy operator is (in  $D$ -dimensions)

$$\nabla_r^2 = \frac{1}{r^{D-1}} \frac{\partial}{\partial r} r^{D-1} \frac{\partial}{\partial r}. \quad (3.34)$$

As the spin of the incident particle can couple in two ways to the orbital angular momentum  $\ell$  (to give total angular momenta of either  $j = \ell \pm 1/2$ ), there are two solutions for each  $\ell$  to the one-body quantum problem posed above. These solutions are identified with “+” for the “stretched” (i.e., parallel) case and “−” for the “jack-knifed” case. In the solution of the radial problem, the kinetic operator can be reduced to a simple second derivative by solving for the product of  $r$  times the radial wave function, sometimes called the reduced radial wave function  $y$ . Employing  $y$  and defining  $\rho = kr$ , the resulting radial wave equations become,

$$\frac{d^2 y_\ell^+(\rho)}{d\rho^2} + \left[ 1 - \frac{V_c}{E} - \frac{(-V_v + iW_v)f(\rho) + 4a_s(V_s + iW)f'(\rho)}{E} - \frac{\ell(V_{so} + iW_{so})h(\rho)}{E} - \frac{\ell(\ell+1)}{\rho^2} \right] y_\ell^+(\rho) = 0 \text{ and} \quad (3.35)$$

$$\frac{d^2 y_\ell^-(\rho)}{d\rho^2} + \left[ 1 - \frac{V_c}{E} - \frac{(-V_v + iW_v)f(\rho) + 4a_s(V_s + iW)f'(\rho)}{E} + \frac{(\ell+1)(V_{so} + iW_{so})h(\rho)}{E} - \frac{\ell(\ell+1)}{\rho^2} \right] y_\ell^-(\rho) = 0. \quad (3.36)$$



The wave number is  $k = (\lambda)^{-1} = \sqrt{(2\mu c^2 E)/\hbar c}$ . These (reduced) radial wave functions are zero at the origin and beyond the nuclear field tend asymptotically to the form

$$\begin{aligned} y_\ell^\pm(\rho) &\propto [H_\ell^{\text{in}}(\rho)] - S_\ell^\pm [H_\ell^{\text{out}}(\rho)], \\ &\propto [G_\ell(\rho) - iF_\ell(\rho)] - S_\ell^\pm [G_\ell(\rho) + iF_\ell(\rho)], \end{aligned} \quad (3.37)$$

where the terms in square brackets can be thought of as the incoming and outgoing waves and the  $S_\ell^\pm = \exp(2i\delta_\ell)$  are the elements of the so-called scattering matrix, where  $\delta_\ell$  are the phase shifts associated with the nuclear potential. (If the potential is spherical,  $\ell$  is a good quantum number and one only needs to be concerned with the diagonal elements of this matrix, indexed by  $\ell$ . If on the other hand, the potential is deformed,  $\ell$  is not a good quantum number and a full matrix – introduced by J. Wheeler – is required). The regular (goes to zero at the origin) and irregular (finite at the origin) Coulomb functions  $F_\ell(\rho)$  and  $G_\ell(\rho)$  are solutions of [Eqs. 3.35](#) and [3.36](#) without the nuclear terms. These functions have the asymptotic forms

$$\begin{aligned} F_\ell(\rho) &\xrightarrow{\rho \rightarrow \infty} \sin \left[ \rho - \eta \ln 2\rho - \frac{1}{2} \ell \pi + \sigma_\ell \right], \\ G_\ell(\rho) &\xrightarrow{\rho \rightarrow \infty} \cos \left[ \rho - \eta \ln 2\rho - \frac{1}{2} \ell \pi + \sigma_\ell \right]. \end{aligned} \quad (3.38)$$

The incoming and outgoing waves have the asymptotic forms

$$\begin{aligned} H_\ell^{\text{in}}(\rho) &\xrightarrow{\rho \rightarrow \infty} \exp \left[ -i \left( \rho - \eta \ln 2\rho - \frac{1}{2} \ell \pi + \sigma_\ell \right) \right], \\ H_\ell^{\text{out}}(\rho) &\xrightarrow{\rho \rightarrow \infty} \exp \left[ +i \left( \rho - \eta \ln 2\rho - \frac{1}{2} \ell \pi + \sigma_\ell \right) \right]. \end{aligned} \quad (3.39)$$

The nonspin-flip  $B(\theta)$  and spin-flip  $A(\theta)$  scattering amplitudes are

$$A(\theta) = f_C(\theta) + \frac{1}{2ik} \sum_{\ell=0}^{\infty} \{ (\ell+1)S_\ell^+ + \ell S_\ell^- - (2\ell+1) \} e^{2i\sigma_\ell} P_\ell(\cos\theta), \quad (3.40)$$

$$B(\theta) = \frac{1}{2ik} \sum_{\ell=0}^{\infty} \{ S_\ell^+ - S_\ell^- \} e^{2i\sigma_\ell} P_\ell^1(\cos\theta), \quad (3.41)$$

where  $\sigma_\ell$  is the (unitless) Coulomb phase shift for the  $\ell$ th partial wave,  $f_C(\theta)$  is the (unitless) Coulomb scattering amplitude, and  $\eta$  is the (unitless) Coulomb or Sommerfeld parameter. These are given by

$$\begin{aligned} \sigma_\ell &= \arg \Gamma(\ell+1+i\eta) = \sigma_0 + \sum_{s=0}^{\ell} \tan^{-1} \left( \frac{\eta}{s} \right), \\ f_C(\theta) &= -\frac{\eta}{2k} \csc^2 \left( \frac{\theta}{2} \right) \exp \left[ 2i\sigma_0 - i\eta \ln \left( \sin^2 \frac{\theta}{2} \right) \right], \end{aligned} \quad (3.42)$$

and

$$\eta = \frac{Z_p Z_t e^2}{\hbar v} = \frac{\mu Z_p Z_t e^2}{k \hbar^2} = 0.1575 Z_p Z_t \sqrt{\frac{A_p}{E_{\text{lab}}/\text{MeV}}}. \quad (3.43)$$

(The gamma function  $\Gamma$  is used in the definition of the Coulomb phase shift.) There are three potential observables for elastic scattering. The first is the differential (elastic) scattering cross section,

$$\frac{d\sigma_E}{d\Omega}(\theta) = |A|^2 + |B|^2. \quad (3.44)$$

The above reduces to the famous Rutherford formula when the Coulomb amplitude  $f_C$  is all that contributes to the scattering amplitude

$$\frac{d\sigma_{\text{Ruth}}}{d\Omega} = |f_C|^2 = \left( \frac{1.44 Z_1 Z_2}{4E/\text{MeV}} \right)^2 \text{fm}^2 = \frac{D_c^2}{16} \csc^4\left(\frac{\theta}{2}\right) \text{fm}^2, \quad (3.45)$$

where  $D_c$  is the distance of closest approach.

The second and the third observables are the polarization,  $P(\theta)$ , and spin rotation,  $Q(\theta)$ , (Glauber and Osland 1979),

$$P(\theta) = \frac{2 \text{Im}AB^*}{|A|^2 + |B|^2} \quad \text{and} \quad Q(\theta) = \frac{2 \text{Re}AB^*}{|A|^2 + |B|^2}. \quad (3.46)$$

If the incident particle is a neutron, the total elastic cross section is finite and integrates to

$$\sigma_E = \pi\lambda^2 \sum_{\ell=0}^{\infty} \left\{ (\ell+1) |1 - S_\ell^+|^2 + \ell |1 - S_\ell^-|^2 \right\}. \quad (3.47)$$

To deduce the total inelastic (sometimes called the reaction) cross section, all one needs to note is that for each  $\ell$ -wave, the outgoing wave is reduced in intensity by  $|S|^2$  relative to the ingoing wave, therefore

$$\sigma_R = \pi\lambda^2 \sum_{\ell=0}^{\infty} \left\{ (\ell+1) (1 - |S_\ell^+|^2) + \ell (1 - |S_\ell^-|^2) \right\}. \quad (3.48)$$

The transmission coefficients can be identified with

$$T_\ell^\pm = 1 - |S_\ell^\pm|^2 \quad (3.49)$$

and in so doing, one can see that the reaction cross section in the absence of intrinsic spin effects results in [Eq. \(3.26\)](#).

The total cross section, a quantity finite only for neutron scattering, comes from the sum of the elastic and reaction cross sections. Upon canceling terms for each pair of  $|1 - S_\ell|^2 + 1 - |S_\ell|^2$  terms, one gets

$$\sigma_T = \sigma_E + \sigma_R = 2\pi\lambda^2 \sum_{\ell=0}^{\infty} \left\{ (\ell+1) (1 + \text{Re}S_\ell^+) + \ell (1 - \text{Re}S_\ell^-) \right\}. \quad (3.50)$$

There are several interesting benchmarks related to the results of [Eqs. \(3.47\)–\(3.50\)](#). The elastic scattering cross section (for neutrals) spans from where  $S_\ell = 1$  (both elastic and inelastic cross sections are zero) to  $S_\ell = -1$ . Thus the cross section for each  $\ell$  lies between

$$0 \leq \sigma_{E,\ell} \leq 4\pi\lambda^2(2\ell+1). \quad (3.51)$$

When  $S_\ell = 0$ ,

$$\sigma_{E,\ell} = \sigma_{R,\ell} = \pi\lambda^2(2\ell+1) \quad \text{thus} \quad \sigma_{T,\ell} = 2\pi\lambda^2(2\ell+1). \quad (3.52)$$

► Equation (3.52) demonstrates that the presence of the inelastic scattering implies an elastic contribution. This explains the factor of 2 in ► Eq. (3.50), which indicates that the *total* cross section for neutrals, that is, the case for which the elastic scattering cross section is finite, is *twice* the geometric reaction value. Recalling the initial discussion of the geometric cross section, partial waves with  $\ell$  greater than some value  $\ell_{\max}$  do not contribute significantly to the summations in ► Eqs. (3.48)–(3.50), thus the sums may be truncated.

### 3.3.3 The Dispersive Optical Model (DOM)

In 1926 R. de L. Kronig noticed that the reflection and absorption of light were interrelated. The next year Hans Kramers explained this relation, essentially allowing for the calculation of *both* the absorption (extinction coefficient) and the index of refraction from the measurement of the 90° reflectance. The key concept is that the response of a system to the stimulus (in this case light and the response in question is called the dielectric response) is dictated by a *complex* quantity, for which the real and imaginary parts are “two-sides of the same coin.” The “sides” are related to one another by energy integrals over the complementary components. (That is, the real part at energy  $\varepsilon$  is related to an integral over all energies of the imaginary component with a pole at the energy of interest, and vice versa.) For example, in the case of the complex dielectric response ( $\alpha$  in the equations below) of matter as a function of the frequency of the stimulus  $\omega$

$$\alpha = \alpha_1 + i\alpha_2$$

$$\alpha_1(\omega) = \frac{1}{2}P \int_{-\infty}^{\infty} \frac{\alpha_2(\omega')}{\omega' - \omega} d\omega' ; \quad \alpha_2(\omega) = -\frac{1}{2}P \int_{-\infty}^{\infty} \frac{\alpha_1(\omega')}{\omega' - \omega} d\omega', \quad (3.53)$$

where P stands for the “Cauchy principal value” of the integral whose integrand has a singularity. These relationships are the result of “causality”; that is, the system cannot respond before the stimulus arrives. From the earliest days of the nuclear optical model, it was appreciated that this relationship should be enforced, as it is in all careful optical spectroscopy.

The difficulty in imposing causality is that the interrelationships are in the form of “dispersion relations.” That is, one must know the real (imaginary) part of the response at *all* energies to deduce the imaginary (real) response at any energy. It is the “all” that provides the stumbling block. As a consequence, this dispersive form of the optical model, or dispersive optical model (DOM), has only limited applicability. However, recently, more effort has been directed at the dispersive optical model analyses of data, as they have been shown to be of great value in predicting the behavior of nuclei removed from stability. The utility of this generator is that in addition to using scattering data (at positive energy), structural data (at negative energy, i.e., the position of bound states) is used to fix the real part of the potential, making both parts more robust (via the dispersion interrelationship). A concise discussion of the Kramers–Kronig dispersion relations as applied to the dielectric response can be found in (Kittel 1986). A full presentation of the dispersive optical model can be found in (Mahaux and Sartor 1990) and its most recent application to nuclei as a function of n/p asymmetry can be found in (Charity et al. 2006, 2007). The most important implications of the DOM [based primarily on nucleon knockout reactions ( $e, e'p$ ) and n and p elastic scattering] are presented below.

First, the connection between the full complex potential and that used in one-body structure models must be unmasked. The imaginary part of the potential vanishes at the Fermi surface. Thus the real one-body potential used as a basis for simple nuclear structure

models is *only* valid near the Fermi surface. Or conversely, if one is interested in phenomena that only involve excitations near the Fermi energy, working with a real potential is valid. On the other hand, at high excitation energies, which are likely to involve particles far above and holes far below the Fermi surface, the imaginary component must be dealt with.

The second feature of this model is that effective masses and spectroscopic factors can be extracted from the energy dependence of the potentials (the former from the real part and the latter, which are related to the occupancy of single-particle states, from the imaginary part). The most striking result of the optical model is that the potential must be made energy-dependent if either the position of the single-particle levels or elastic scattering over a broad range of energies are to be reproduced. While the positions of the levels near the Fermi surface can be extracted from single-nucleon transfer reactions, (e,e'p) reactions are needed to determine the strength functions below the Fermi surface. (These functions will exhibit sharp peaks for orbits slightly below the Fermi surface and broad distributions for deeply bound orbits.) This dependence is shown in ▶ Fig. 3.17 for  $^{208}\text{Pb}$ .

If the dependence is linear, an effective mass ( $m^*$ ) can be introduced to allow the single-particle energy to be recast in terms of a fixed potential,

$$\varepsilon = \frac{(\hbar k)^2}{2m} + \left[ V_0 + \frac{dV}{d\varepsilon} \varepsilon \right] = \frac{(\hbar k)^2}{2m} + [V_0 + \alpha \varepsilon], \quad (3.54)$$

$$\varepsilon = \frac{(\hbar k)^2}{2m(1-\alpha)} + V_0(r) \left( \frac{1}{1-\alpha} \right) = \frac{(\hbar k)^2}{2m^*} + V_0'(r), \quad (3.55)$$

with

$$\frac{m^*}{m} = 1 - \alpha = 1 - \frac{dV(r, \varepsilon)}{d\varepsilon} \approx 0.7 \quad (3.56)$$

Referring back to the harmonic oscillator, ▶ Fig. 3.18 shows that an effective mass greater (less) than the nucleon mass will decrease (increase) the single-particle level spacing, making both the single-particle level density and many-body density of states larger (smaller).

The above discussion is associated with the finite range of the nucleon-nucleon interaction. This can also be viewed (via a Fourier transform) as a momentum dependence of the

▶ Fig. 3.17

The energy dependence of the potential needed to reproduce the positions of the single-particle levels for  $^{208}\text{Pb}$  (from Mahaux and Sartor 1990)

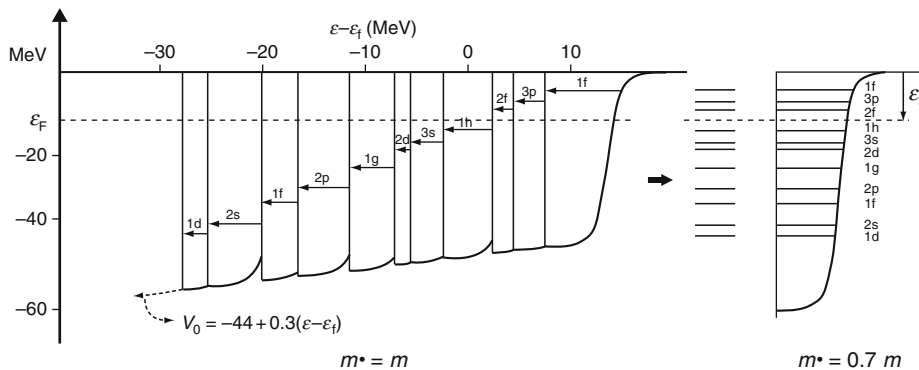
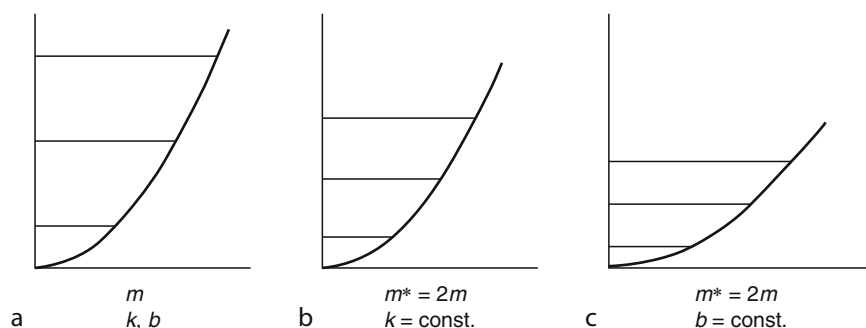


Fig. 3.18

How an effective mass affects the single-particle level spacing



interaction. As a consequence, the effective mass contribution mentioned above is often called the “ $k$ -mass” or the momentum-dependent effective mass. This mass is relevant for matter (i.e., neutron-star calculations) and its dependence on neutron–proton asymmetry has attracted considerable attention (Li et al. 2008).

The description of real nuclei requires more than the  $k$ -mass. A second multiplicative effective-mass term, the “omega mass” or  $m_\omega$ , arises from a time nonlocality of the interaction. (As the exchange involves mesons with mass, the “throwing” and “catching” are not simultaneous events.) This time nonlocality can be viewed as a fundamental energy (or frequency) effect. Following prescriptions developed by Mahaux and collaborators (Mahaux and Sartor 1990), the relative change of the effective mass from real nucleon masses can be represented by two unitless terms,

$$\frac{m^*}{m} = m_k m_\omega. \quad (3.57)$$

The “omega mass” is peaked at the nuclear surface, producing what solid-state scientists would call surface states. In the nuclear case, this just corresponds to low-lying (i.e., near the Fermi surface) collective excitations associated with the physical surface. The combined effective masses and the potentials from which they are derived are shown in Fig. 3.19. The  $k$ -mass suppresses the effective mass in the interior and the omega-mass produces a peak at the nuclear surface. Also extracted from this analysis are the occupation probabilities of single-particle levels, a subject that will be addressed in the next section when discussing single-particle knockout reactions from nuclei far-removed from stability.

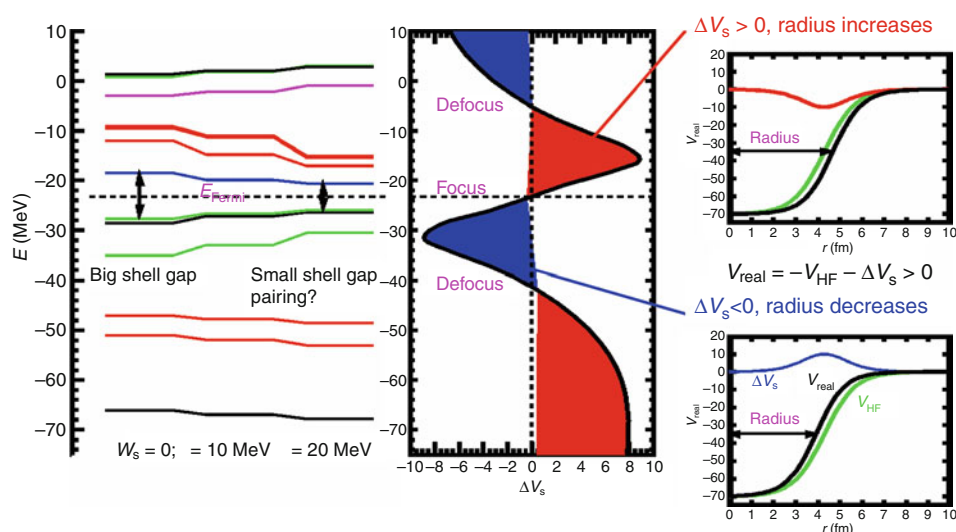
What must also be appreciated is that effective masses: (1) can be viewed as a compact repackaging of other physics, such as momentum dependent potentials, and (2) are required for discussing reactions as well as structure. Examples of the latter (for reactions) stem from the fact that the spacing of single-particle levels near the Fermi surface affects the many-body density of states ( $\omega$ ).

### 3.4 Near-Barrier Reaction Mechanisms

The study of nuclear reaction mechanisms has revealed a breadth of phenomena that have subsequently stimulated advances in related areas of nuclear research, as well as in nuclear

■ Fig. 3.19

Effect of the omega-mass on the refocusing of single-particle levels near the Fermi surface. This focusing is the result of the requirement that the potential be “pushed in” below the Fermi surface and “pulled out” above the Fermi surface in order to reproduce both the position of bound states and the scattering data (from Charity et al. 2007)



applications. The impetus to obtain a quantitative understanding of these phenomena has motivated the development of increasingly sophisticated measurement technologies, described elsewhere in this Handbook. Here, only an overview of the principal reactions of interest to, or being investigated by, nuclear chemists is provided. Additional references can be found in (Cerny 1974; Durand et al. 2001; Benenson et al. 2002).

Nuclear reaction mechanisms can be schematically separated into two general categories: low-energy reactions that are strongly influenced by structure around the Fermi energy and those at much higher energies where elementary nucleon-nucleon collisions become increasingly important. In either case, the correlations existing within the (ground-state) projectile and target can play determinative roles. This is true at low energy (alpha decay informs about alpha-clustering in the low-density surface of heavy nuclei) as well as high energy (where  $e^-$ -induced knockout reactions indicate an overwhelming dominance of high relative-momentum n-p pairs.)



As the model of nuclei composed of nucleons moving independently in a one-body potential is one that is roughly 75% correct, this mean-field approach often provides a rather good initial description of reactions. However, above energies commensurate with the depth of the one-body potential, this potential has little meaning and the best starting point is to consider collisions as sequences of individual nucleon-nucleon collisions. Often a distinction between the *mean-field* and *nucleon-nucleon* (N-N) regimes is made at bombarding energies of about 20 MeV per projectile nucleon (20 MeV/A). Below this energy, individual nucleon-nucleon (N-N) interactions lead to thermalization sufficiently quickly that no individual nucleon has sufficient energy to escape the mean-field potential well. When this has been achieved, a compound nucleus has been formed. As the relative collision energy increases, the

energy dissipation process produces harder N-N collisions with scattered nucleon energies in excess of the mean-field constraints, leading to prompt particle emission. The transition from mean-field to N-N dominance as the bombarding energy increases is a continuous one, mediated by the number of collisions that are not prohibited by the Pauli Principle (*Pauli blocking*). The blocking of 2-body collisions is strong below the Fermi energy, thus leading to surprisingly long mean-free paths at low energy, but weakens as the relative energy per nucleon approaches the Fermi energy.

However, it must also be appreciated that in either regime (mean-field or N-N), the correlations that exist in nuclei can be observed, sometimes as details in the extremes of distributions, other times as an essential ingredient required to explain gross observations, such as the  $\alpha$ -particle emission in general.

This section is divided into several parts that focus on the near-barrier domain. The following section addresses N-N dominated reactions. One final comment must be made in an attempt to be forward looking. While the partition of reactions into low and high energy (mean-field dominated or not) has been common in the past, future work must move beyond this mental partition. As mentioned above, due to correlations in the nucleus, the ground state is replete with high-energy nucleons, well above what would be expected from the Fermi-gas model. It is actually this aspect, the correlations that exist in nuclei (for example as a function of n/p asymmetry), that will be the focus of many reaction studies in the future.

### 3.4.1 Neutron Capture

Recent work at the lowest energies has generated detailed data on (n,x) reactions on nuclei throughout the periodic table. Due to interest in advanced fuel cycles, as well as for possible transmutation of reactor waste, the attention has focused on the actinide elements. (All of these data can be found at the NNDC web site.)  *Figure 3.20* shows both fission and capture cross sections over six orders of magnitude in energy for  $^{232}\text{Th}$ . The three regions shown schematically in  *Fig. 3.10* are clearly seen. The central region is dominated by pronounced resonances, bordered on each side by smoothly varying cross sections. The resonances for heavy nuclei have many-body wave functions, far too complicated to describe. (Only in the lightest nuclei can these resonances be described by simple single-particle excitations.) At higher energy, the number of these many-body resonances is so large per unit energy that they overlap and no experimental resolution would be sufficient to resolve them. At energies lower than the resonance region, one sees capture into the tail of the lowest-lying resonance, but with a probability that increases with the increasing de Broglie wavelength of the neutron (with decreasing energy).

In calculating the capture cross section for the lowest-energy neutrons, it is necessary to consider the energy *level width*  $\Gamma_i$  and the *natural lifetime*  $\tau_i$  of resonances. The uncertainty principle gives

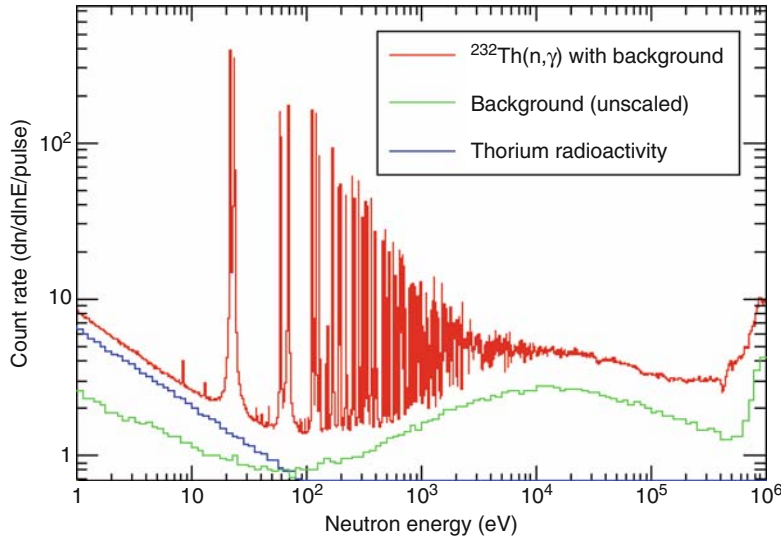
$$\Gamma_i = \hbar/\tau_i, \quad (3.58)$$

i.e., short lifetimes correspond to large level widths. For the general reaction  $A + a \rightarrow [CN] \rightarrow B + b$ , the resonance cross section is given by the *Breit–Wigner* form (Breit and Wigner 1936):

$$\sigma(a, b) = \frac{\pi \lambda^2 w(I) \Gamma_a \Gamma_b}{(E_a - E_0)^2 + (\Gamma/2)^2}, \quad (3.59)$$

Fig. 3.20

The Th n-capture and fission cross sections from 1 eV to 1 MeV (from Aerts 2006)



where  $w(I)$  is a spin factor, a function of the spin of the CN (many-body) state,

$$w(I) = \frac{2I_{\text{CN}} + 1}{(2I_A + 1)(2I_a + 1)}, \quad (3.60)$$

and  $\Gamma$  is the total width composed of the sum of the partial widths  $\Gamma = \sum_k \Gamma_k$  (the summation index  $k$  includes the exit channel  $b$ ).  $E_a$  is the projectile center-of-mass energy and  $E_0$  is the energy of the resonant state.

At very low energies, comparable to the average thermal energy  $(3/2)k_B T \approx 0.025$  eV,  $(n, \gamma)$  is the only open channel. Thus the sum above has only one term, corresponding to gamma-ray emission ( $b = \gamma$ ). These conditions, plus the realization that the neutron capture rate should depend on the velocity  $v$  (this is basically a detailed balance argument, more neutrons per unit time will impact the nucleus per unit time at high velocity than low), lead to the following approximations:

$$\begin{aligned} E_a = E_n \approx 0, \quad \text{so that} \quad E_n - E_0 \approx -E_0 \quad \text{and} \\ \Gamma_a = \Gamma_n \propto v_n \Gamma \quad \text{and} \quad \Gamma_b = \Gamma_\gamma = \Gamma. \end{aligned} \quad (3.61)$$

Furthermore,  $E_0$  is a constant close to zero (as the resonance is close to zero energy). Thus the first term in the denominator is small compared to the second and, aside from terms that do not depend strongly on energy, the Breit-Wigner formula – [Eq. \(3.59\)](#) – reduces to a simple  $1/v$  dependence,

$$\sigma(n, \gamma) \propto \pi \lambda^2 w(I) \left( \frac{v_n \Gamma \Gamma}{\Gamma^2} \right) \approx \frac{\pi \hbar^2 v_n}{(m v_n)^2} \propto \frac{1}{v_n}. \quad (3.62)$$

That is, for *thermal neutrons*, the lower the energy the higher the cross section.



As the neutron energy increases from thermal to higher energies, the cross section first falls monotonically according to the  $1/v$  law. In the vicinity of each resonance state, where  $E_n \approx E_0$ , sharp spikes are observed in the cross section. When the state density (levels per unit energy) times the mean intrinsic width rises to order one, states are no longer resolved. At this point, the cross section is smoothly varying, of magnitude very roughly equal to the geometric value  $\sigma^{\text{geo}} = \pi R^2$ .

While the actinide region has achieved much recent attention,  $(n, \gamma)$  reactions throughout the periodic table are important for the analytic tool of neutron activation. Cd is also important for reactor control as the reaction  $^{113}\text{Cd}(n, \gamma)$ , with  $\sigma = 2.0 \times 10^4$  b, is used to control the reactor neutron flux and hence the multiplication factor  $k$  in reactor design. The reaction  $^{135}\text{Xe}(n, \gamma)$  with  $\sigma = 2.6 \times 10^6$  b is a prominent fission-product poison that creates problems in the operation of nuclear reactors by consuming neutrons unproductively.

One of the most important features that can be gleaned from the  $(n, \gamma)$  data mentioned above is the density of states in the excitation energy region near the binding energy of the neutron. Upon capture, a neutron with thermal energy creates a nucleus with  $A + 1$  nucleons and  $E^* = B_N$ . Collecting data from throughout the periodic table has validated the dependences expected for the many-body density of states from the *Fermi-Gas Model*. In this model, which is also needed to calculate the contribution to the heat capacity of the conduction electrons in metals (the component that becomes dominant at very low temperatures), the excitation energy (the thermodynamic internal energy often indicated by  $U$ ) is proportional to the square of the temperature. The reason for the square rather than the linear dependence in classical gases is that not all the nucleons share in the excitation energy. The number of excited nucleons increases in proportion to  $T$ , as does the average energy of each of these (excited) nucleons. The same explanation holds for conduction electrons in metals at very low  $T$ .

$$E^* = aT^2. \quad (3.63)$$

As  $dU = + SdT - PdV$  and  $U = E^*$ , the entropy is

$$S = \left( \frac{dE^*}{dT} \right) = 2aT, \quad (3.64)$$

and thus, using the Third Law,  $S = k_B \ln \omega(E^*)$ , one would expect the density of levels to be roughly

$$\omega^L(E^*) \approx Ce^{2aT} \approx Ce^{2\sqrt{aE^*}}. \quad (3.65)$$

Refer to Huizenga and Moretto (1972) for a general discussion of level densities. Note that the state density  $\omega$  enumerates each projection of the angular momentum while the level density  $\omega^L$  does not.

A more careful analysis of a two-component Fermi gas with spin and thermal energy ( $U = E^* - E_{\text{rot}}$ ) yields (Bohr and Mottelson 1969)

$$\omega^L(U) = Ce^{2\sqrt{aU}} / U^2. \quad (3.66)$$

In practical usage the constants  $a$  and  $C$  are empirically-determined. Only experiments at low  $E^*$ , like resonance counting, are sensitive to the prefactor  $C$ . Experiments in the region of unresolved states are sensitive only to a relative change in the level density, i.e.,  $\omega^L(E^* + \Delta) / \omega^L(E^*)$ , and thus only the *level density parameter*  $a$  can be extracted. It is the parameter  $a$  that

relates the excitation energy to the nuclear temperature. This parameter is roughly proportional to  $A$  but is reduced near closed shells. For near-ground-state nuclei away from closed shells, the average value is near  $a \approx (A/8) \text{ MeV}^{-1}$  (► Fig. 3.21).

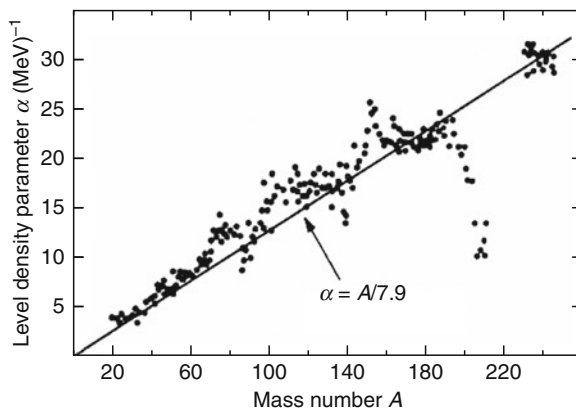
The mass number dependence is what one would expect from “particle-in-a-box logic,” i.e., the larger the box, the greater the number of single-particle levels per unit energy and the greater the number of ways to distribute particles among these levels with a fixed total available energy. However, independent-particle models predict that  $a$  should be closer to  $(A/12) \text{ MeV}^{-1}$ . There are both macroscopic and microscopic explanations for this discrepancy. From a macroscopic view, the nuclear surface, being less dense than the bulk, can accommodate more levels per nucleon. (Lower density, larger volume per particle, larger box, higher density of single-particle states.) This approach was pioneered by Töke and Swiatecki (1981).

These semiclassical formulations for the mass number  $A$  and deformation dependence of  $a$  are extensively used in statistical decay models. From the microscopic point of view, the augmentation of the density of states at low energy is explained as follows. In a single-particle picture the excitation is “carried” by exciting nucleons to single-particle states (solutions to the one-body potential problem). However, collective rotational bands can be built on any single-particle structure (excitation). Although these states are in principle described in the single-particle picture, they would lie at very high excitation energy in such a model rather than where they really are – low energy. Thus the enhancement in the level density at low energy – the  $a \approx (A/8) \text{ MeV}^{-1}$  – can be viewed as a consequence of collective excitations that in a pure single-particle picture belong at very high energy. While the relocation of many-body states from high to low energy greatly increases the  $\omega^L$  at low energy, it hardly affects the count at high energy as the number of states increases exponentially.

Thus one would expect  $a$  to decrease ( $\omega$  increases, but the rate of increase slows) with excitation. In the last decade this has been confirmed (Shlomo and Natowitz 1990). Modern statistical model calculations (see ► Sect. 3.5) now employ an excitation-energy-dependent  $a$  that varies from about  $a = (A/7) \text{ MeV}^{-1}$  at low energy to about  $a = (A/13) \text{ MeV}^{-1}$  by the time the total excitation energy reaches 100 MeV.

► Fig. 3.21

Level-density parameter  $a$  as a function of mass number. The solid line shows an average fit for  $a = (A/7.9) \text{ MeV}^{-1}$  (from Huizenga and Moretto 1972)



### 3.4.2 Nucleon and Heavy-Ion Elastic Scattering

#### 3.4.2.1 Nucleon Elastic Scattering

*Elastic scattering* describes the simplest target-projectile interactions: specifically, those in which the colliding nuclei experience only an angular deflection, but do not change their  $Z$  or  $A$  composition or their energy state (► Fig. 3.22). For below-barrier projectile energies, the differential cross section for elastic scattering is governed by the Rutherford (Coulomb) scattering equation (► Eq. (3.45)). Rutherford employed this expression to deduce an upper limit to the size of nuclei and, from the angular distribution, the atomic number of the scatterer (Rutherford 1911). This same technique is in common use in analytical surface science work and was notably applied to analyze the elemental composition of lunar samples in situ by observing the scattering of alpha particles emitted from a radioactive source.

Below the Coulomb barrier only elastic and inelastic excitation by Coulomb excitation are likely. Moving above the Coulomb barrier, various inelastic reaction channels compete with each other and with elastic and Coulomb excitation for the partitioning of the income flux. These channels interfere with one another, as do elastic fluxes from near and far-side scattering. ► Figure 3.23 shows all the existing data for nucleon scattering from Ca isotopes. (Shown are the differential cross sections and the analyzing powers. The cited reference also contains spin-rotation data.) Also shown in this figure are the Dispersive Optical Model fits that define the potential, which in turn define the effective masses and occupancies of single-particle states.

The occupancy of single-particle states was extracted in the 1980s for stable nuclei using  $(e,e'p)$  for several nuclei on the line of beta stability. Much recent effort has been spent in attempting to do the same for nuclei off the line of stability and thus extract the asymmetry dependence of spectroscopic factors. Spectroscopic factors expose the deviation from a simple one-body description of the nuclear quantum problem. For example, if removal of a nucleon, from a system with  $A$  nucleons and associated quantum numbers, leaves the  $A - 1$  system in the ground state, the spectroscopic factor would be unity. However, as the real  $A$  (and  $A - 1$ ) systems are strongly correlated, removal of a particle requires a “reorganization” of the others. The spectroscopic factors can be roughly thought of as the fraction of the wave function (of valence particles) that can be described by occupancy of a mean-field quantum solution. Standard shell models predict spectroscopic strength less than one, but such calculations

■ Fig. 3.22

Trajectories of projectiles impinging on a target for reactions below the barrier (*left*), where only elastic scattering occurs and above the barrier (*right*), where the more central trajectories are absorbed. As is seen, nuclear reactions will necessarily decrease the large angle fraction of elastically scattered projectiles

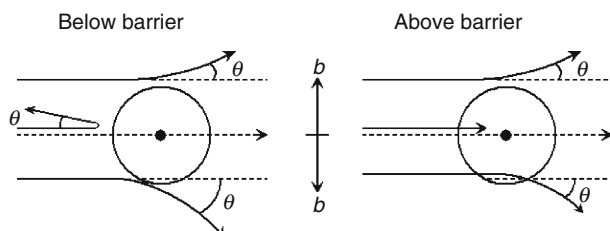
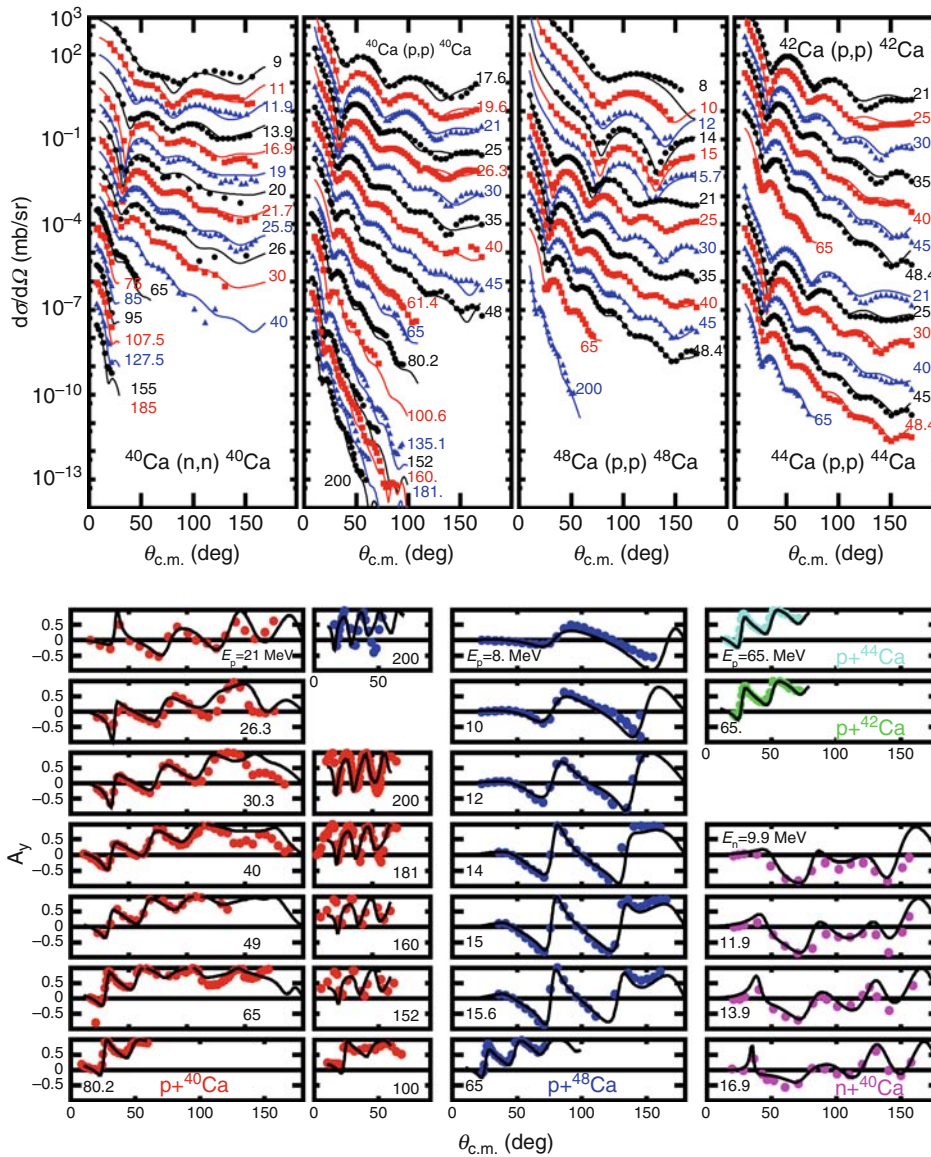


Fig. 3.23

World data set (below 200 MeV) of n and p elastic scattering on Ca isotopes along with DOM fits  
(From Charity et al. 2007)

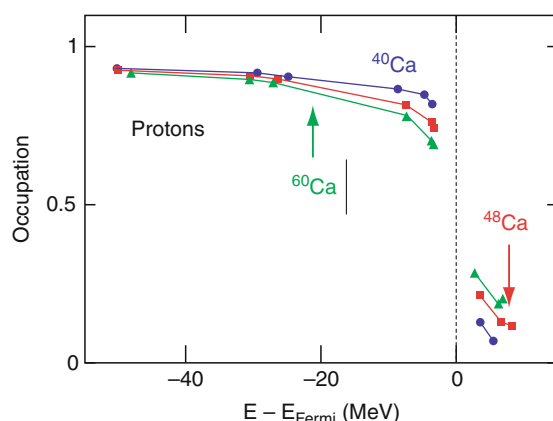


only capture that piece of the correlations contained in the space of the calculation. Particle correlations (for example multiparticle hole strength required to describe the ground state) beyond this very limited space would yield spectroscopic strength with even greater reductions than those predicted by standard shell-model calculations.

Three experimental lines of approach have been used to study the evolution of spectroscopic strength with asymmetry: the dispersive optical model, nucleon knockout reactions, and

■ Fig. 3.24

Proton single-particle occupation probabilities in  $^{40}\text{Ca}$  (circles),  $^{48}\text{Ca}$  (squares), and  $^{60}\text{Ca}$  (triangles) as deduced from a Dispersive Optical Model fit (Charity et al. 2007)



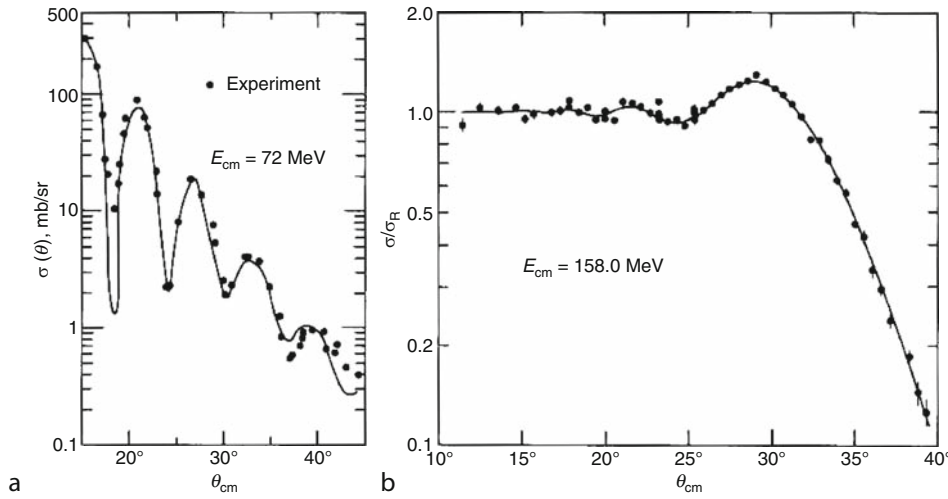
transfer reactions, the latter two projects using secondary beams. The results from these experiments are as follows: there is a general trend that the spectroscopic strength decreases (below the Fermi surface) for the minority (protons in this case) species. That is, for the analysis of the Ca isotopes presented in Fig. 3.23, the proton spectroscopic strength below the Fermi surface decreases in going from  $^{40}\text{Ca}$  to  $^{48}\text{Ca}$  to  $^{60}\text{Ca}$  ( $^{60}\text{Ca}$  being an extrapolation from the fit), Fig. 3.24. This trend is likely the result of increasing p-n correlations mediated by the tensor force. The same trend is found in nucleon knockout reactions (Gade et al. 2004). However, here the effect mentioned above is found to be much stronger than that found in the DOM analysis. An additional difference is that the knockout work implies that this effect is a function of binding energy (the greater the binding, the greater the correlations), while in the dispersive optical model, the evolution is more subtle, depending on the parity of the levels (of both neutrons and protons) engaging in the correlations. For example, in the DOM case, while the occupancy of single-particle proton states decrease (increase) below (above) the Fermi surface in going from  $^{40}\text{Ca}$  to  $^{60}\text{Ca}$ ; there is little change in the neutron occupancy over this same range of asymmetry. This latter trend, while in contrast to the knockout results, is in agreement with the transfer studies (Lee et al. 2010). While the elucidation of this trend will be a major focus of research in the coming decade, the present DOM analysis suggests that nucleon correlations increase with the number of possible n-p pairs. (That is, protons become more strongly correlated with increasing neutron number, while neutron correlations do not increase with increasing neutron number.)

### 3.4.2.2 Heavy-Ion Elastic Scattering

Because of its diffractive nature (Fig. 3.25), elastic scattering measurements provide a useful probe of the nuclear potential near the nuclear surface, thus providing parameters for potential models such as the optical model. Reaction cross sections for reactions induced by heavy ions (HI) can also be determined from elastic scattering experiments (see superscript exp in the

■ Fig. 3.25

**Left:** Elastic scattering angular distribution for  $^{12}\text{C} + ^{16}\text{O}$ , illustrating *Fraunhofer scattering* (Hiebert and Garvey 1964). **Right:**  $^{16}\text{O}$  ions incident on a  $^{208}\text{Pb}$  target, showing a *Fresnel scattering* pattern (Baker and McIntyre 1967). The disappearance of elastic events at large angles is due to the absorption of lower  $\ell$ -waves



following equation), since nuclear reactions preferentially remove elastic events at large scattering angles (low  $\ell$ ). Consequently, the ratio of the experimental elastic scattering cross section  $d\sigma_E/d\Omega$  to the Rutherford scattering cross section as a function of angle will decrease strongly beyond some critical angle  $\theta_{\text{crit}} \sim 30^\circ$  (► Fig. 3.25). The reaction cross section  $\sigma_R$  can be estimated from

$$\sigma_R = \int_{\theta_{\text{crit}}}^{\pi} \frac{d\sigma_{\text{Ruth}}}{d\Omega} d\Omega - \int_{\theta_{\text{crit}}}^{\pi} \frac{d\sigma_{\text{el}}^{\text{exp}}}{d\Omega} d\Omega. \quad (3.67)$$

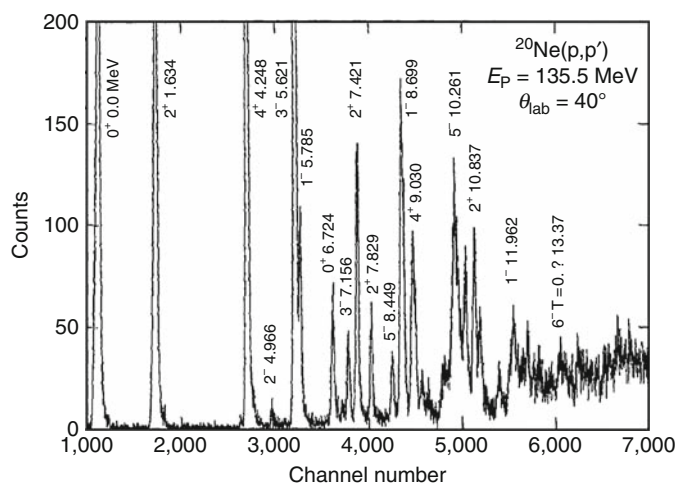
More precise results can be obtained with diffractive models (Frahn 1978), which relate  $\ell_{\text{max}}$  to the quarter point (or grazing) angle  $\theta_{1/4}$ , the angle at which  $\sigma_{\text{el}}^{\text{exp}}(\theta)/\sigma_{\text{el}}(\theta) = 0.25$ ,  $\ell_{\text{max}} = \eta \cot(\theta_{1/4}/2)$ . The adherence of experiment to the Rutherford values for scattering angles well below  $\theta_{1/4}$  makes elastic scattering a valuable technique for cross-section normalizations in heavy-ion reaction studies. The strong Coulomb field for heavy-ion collisions, proportional to  $Z_p Z_t$ , has important nuclear consequences. Among these are the Coulomb excitation of deformed nuclei to very high rotational levels and the fission of heavy nuclei at relativistic projectile energies.

### 3.4.3 Inelastic Excitation

*Inelastic scattering* refers to collisions in which there is a change in the energy state(s) of the target and/or projectile nuclei, but no change in  $Z$  and  $A$ . Such reactions are useful for

■ Fig. 3.26

Spectrum of protons observed in the  $^{20}\text{Ne}(p,p')$  reaction. Elastically scattered protons appear in the  $0^+$  peak at 0.0 MeV near channel 1,100. Inelastic events populate the excited states of  $^{20}\text{Ne}$  (Courtesy of E. J. Stephenson, IUCF)



investigating both the quantal and collective features of nuclear structure. Studies that employ  $(p,p')$  and  $(\alpha,\alpha')$  reactions are particularly useful for measuring the spins and parities of particle states in stable nuclei. In [Fig. 3.26](#) the spectrum of protons observed in the  $^{20}\text{Ne}(p,p')$  reaction is shown as an example.

*Coulomb excitation* is the process by which nuclear excitation occurs without a hard nuclear reaction. Basically, the energy for excitation is extracted from the time-varying Coulomb field as a target and projectile pass one another. This reaction has had a significant rebirth with the availability of fast ( $>50$  MeV/A) heavy-ion beams. The basic process ([Fig. 3.27](#)) is strongly energy-dependent ([Fig. 3.28](#)) and allows for the extraction of the reduced matrix element for quadrupole excitation (from the probability of exciting the first  $2^+$  state) as well as studying collective giant resonances. The revival is due to the potential for making these measurements on fast (off  $\beta$ -stability) secondary radioactive beams (Glasmacher 1998).

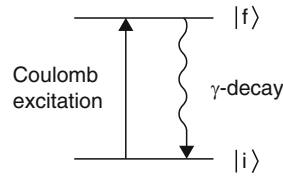
In the case of the excitation of the first  $2^+$  state of even-even nuclei, in addition to determination of the energy of this low-lying state, one also measures the reduced matrix element  $B(E2)$  from the yield of  $\gamma$ -rays depopulating this state. As the beam energy is increased, the probability for excitation of large-scale collective motion (giant resonances) increases ([Fig. 3.28](#)). Fast-beam Coulomb excitation has been a fruitful area of research, because low-intensity secondary beams can be used since cross sections can be significant fractions of a barn. The focus here will be on just one of the interesting findings of this productive research area.

[Figure 3.29](#) shows the energy of the  $2_1^+$  state for silicon, sulfur, and argon isotopes,  $Z = 14, 16, 18$ , respectively. (The trailing subscript is used to indicate which level of a specific spin and parity to which one is referring. Thus  $0_2^+$  is the second  $0^+$  state in that nucleus.) First, focus on the behavior at  $N = 20$ . The relatively high energy of the  $2_1^+$  state in Si and S indicates that  $N = 20$  is in fact magic for the corresponding proton numbers. Shifting the focus to the



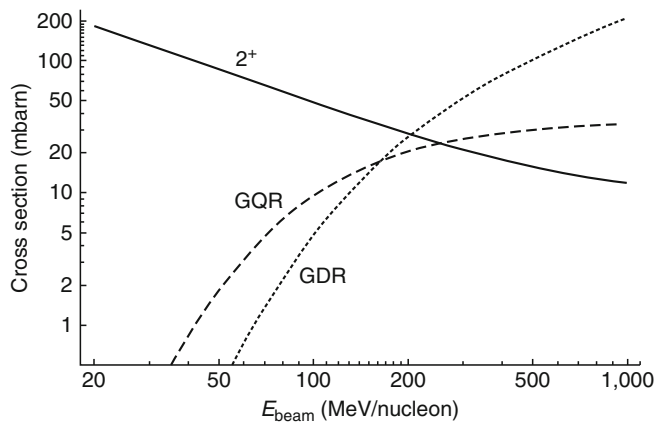
■ Fig. 3.27

Schematic picture of the first-order Coulomb excitation of a nucleus from an initial state to a final bound state and its subsequent  $\gamma$ -decay



■ Fig. 3.28

Calculated cross sections for Coulomb excitation of  $^{40}\text{S}$  in the first excited state ( $2^+$ ), the giant dipole resonance (GDR), and the giant quadrupole resonance (GQR) in  $^{40}\text{S}$  using a  $^{40}\text{S}$  beam incident on Au, versus the beam energy. The calculation assumes a minimum impact parameter of 16 fm (From Glasmacher 1998)



region of  $N = 28$ , one finds that the same cannot be said, i.e.,  $N = 28$  is seemingly not magic for these very neutron-rich species. The  $B(E2)$  values support this assertion. This loss of “magicity” to the “South-East” of stability on the chart of the nuclides is called the “island of inversion.” More generally, it has been appreciated that the values, or strengths, of the “magic” numbers can change with unusual  $n/p$  ratios. This shifting magicity can have universal consequences. For example, it has been postulated that the inversion region mentioned above determines the  $^{48}\text{Ca}/^{46}\text{Ca}$  abundance ratio in Nature (Sorlin et al. 1993).

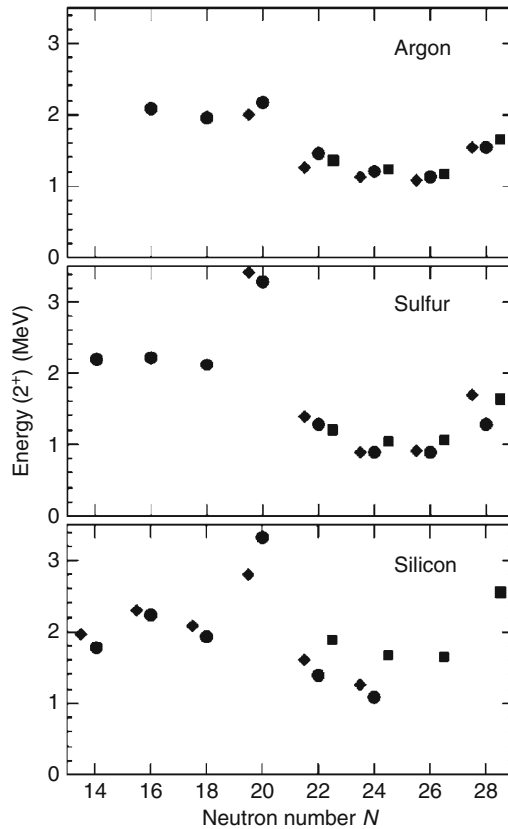
Inelastic excitation via  $\alpha$ -particles (i.e.,  $\alpha, \alpha'$ ) has provided the bulk of the data on the highly collective giant monopole resonance, often called the “breathing mode.” Data of this type (► Fig. 3.30) have been used to extract the nuclear incompressibility of finite nuclei, and with the aid of models, the incompressibility of symmetric matter (see ► Sect. 3.7).

With greater overlap of the two nuclear potentials, additional channels open up that permit transfer of one or more nucleons, or *direct reactions* (Austern 1970). Classic examples of direct reactions are one-nucleon transfer, or stripping, and pickup reactions. *Stripping* is the transfer of a single nucleon from the projectile to the target, for example a (d,p) reaction. *Pickup* is the



■ Fig. 3.29

Excitation energies of the first excited  $2^+$  states in argon, sulfur, and silicon plotted versus the neutron number  $N$ . Measured values (solid circles) are compared to shell-model calculations with a full and a truncated set basis states



reverse reaction, i.e., transfer of a nucleon from target to projectile, as in a (p,d) reaction. At low beam energies, the higher probability for neutron transfer relative to proton transfer demonstrates the charge polarizability that the colliding nuclei experience as they approach one another. This is shown schematically in [Fig. 3.31](#).

Direct reactions need not be simple one-step processes. The likelihood of a one-step process improves if the momentum transfer  $q$  is close to the angular momentum of the transferred nucleon divided by the nuclear radius at which the transfer occurs,

$$q \equiv |\mathbf{k}_{\text{in}} - \mathbf{k}_{\text{out}}| \approx \ell/R. \quad (3.68)$$

If this matching condition is satisfied, the cross sections can be compared to one-step reaction models, such as the Distorted-Wave Born Approximation (DWBA), from which spectroscopic information can be extracted. The common DWBA codes are DWUCK and PTOLEMY.

Fig. 3.30

**Left:** Spectra for the giant monopole and isoscalar dipole resonances obtained in  $(\alpha, \alpha')$  measurements and **right:** The extracted nuclear matter (nm) incompressibility constant  $K_{nm}$  (Figure courtesy, P. H. Youngblood, Texas A&M University)

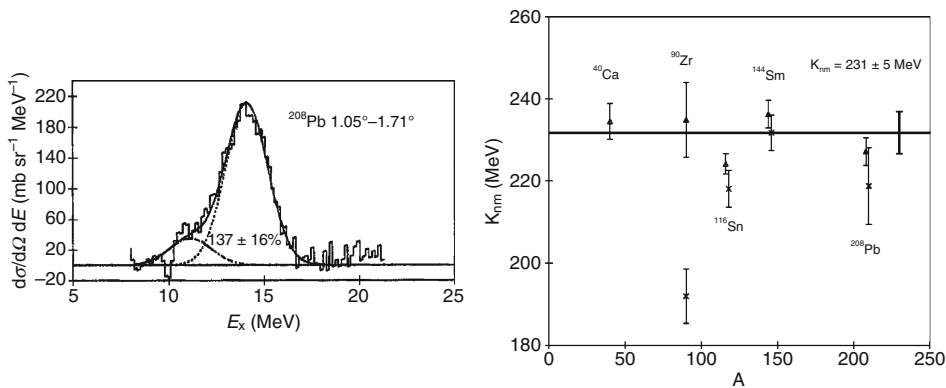
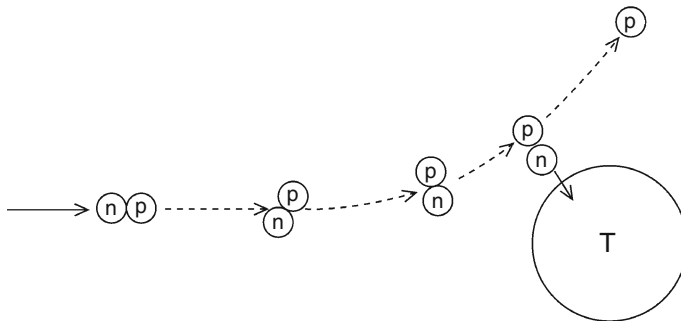


Fig. 3.31

**Schematic diagram of a (d,p) transfer reaction.** Notice that the deuteron is polarized due to mutual Coulomb repulsion with the target. For a (p,d) pick-up reaction the arrows should be reversed



Stripping and pickup studies with heavy radioactive (secondary) beams on light targets are beginning to provide structure data on nuclei far-removed from stability. Furthermore, since the (d,p) reaction is the analog of neutron capture ( $n, \gamma$ ), it provides an important surrogate pathway for studying nuclear mass buildup in r-process nucleosynthesis (see Chap. 12 in Vol. 2). Using the  $d({}^A_Z X, {}^{A+1}_Z X)p$  reaction, reverse kinematics reactions with beams of neutron-rich radioactive nuclei make it possible to study the structure and neutron-capture probabilities of nuclei nearer the *neutron-drip line* (neutron separation energy near zero).

A similar tool that is useful for studying mirror nuclei and isobaric analog states is the *charge-transfer reaction* of the type (p,n) or (n,p), the nuclear reaction equivalent of beta-decay. *Mirror nuclei* are pairs of isobars that can be interconverted by exchanging a neutron and a proton, e.g.,  ${}^{15}_7\text{N}_8$  and  ${}^{15}_8\text{O}_7$ . An *isobaric analog state* of nucleus  ${}^Z_N X_N$  is also a state in the

nucleus for which nucleonic wave functions are the same, as are the masses after correction for the Coulomb energy and the neutron-proton mass difference. One practical application of this process has been the measurement of the  $^{37}\text{Cl}(p,n)^{37}\text{Ar}$  and  $^{71}\text{Ga}(p,n)^{71}\text{Ge}$  cross sections that are related to understanding measurements of the *flux of solar neutrinos* (Bowles and Gavron 1993).

Numerous theoretical models have been employed in the analysis of direct reactions at low energies. Among the most prominent of these is the coupled-channels approach, which incorporates the quantum structure of the colliding nucleus and its product (Tamura 1965; Dasso and Landowne 1987). The coupled channels can be either inelastic or transfer modes. The coupled-channels model has proven to be among the most successful approaches for obtaining quantitative understanding of direct-reaction probabilities. In addition, it has served as a valuable guide in the interpretation of subbarrier fusion reactions (Broglia et al. 1983).

In heavy-ion reactions, the more general term *quasielastic scattering* is frequently applied to reactions at the nuclear surface. This more inclusive definition covers not only the above mechanisms, but also *multiple-nucleon-transfer reactions*. In these events, two or more nucleons may be transferred, producing a more diverse array of reaction products. The multiple-nucleon-transfer mechanism can produce nuclei relatively far away from the line of beta stability. Consider the example,



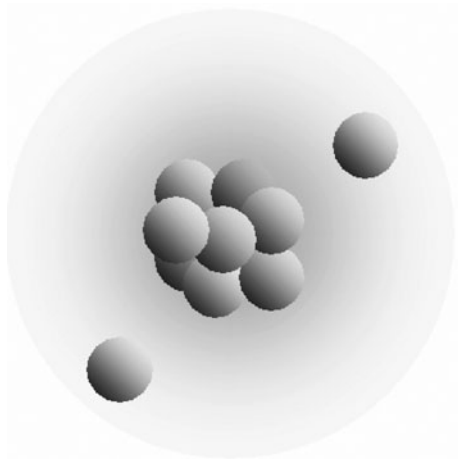
in which four neutrons are transferred from  $^{48}\text{Ca}$  to  $^{64}\text{Zn}$  and one proton is transferred in the reverse direction. While quantum and collective structure effects play an important role in inelastic scattering and few-nucleon transfer reactions, the primary products may also be formed with significant excitation energies. If the excitation energy exceeds particle binding energies, then secondary decay via statistical emission alters the primary exit channel nucleus.

### 3.4.4 Nucleon Knockout Reactions

*Nucleon knockout reactions* have also been the focus of considerable recent effort (both knockout and Coulomb excitation are dealt with in Gade et al. 2004 and Gade and Glasmacher 2008). One famous example of the power of nucleon knockout reactions using secondary beams is that of  $^{11}\text{Li}$ , an extremely neutron-rich nucleus. It is thought to have a neutron halo, which would explain its large reaction cross section (Tanihata et al. 1985, [Fig. 3.32](#)). With a half-life of 8.7 ms,  $^{11}\text{Li}$  can be produced by fragmentation of a heavier species (usually  $^{18}\text{O}$ ), separated in flight from other fragmentation products and made into an almost pure beam. Directing this beam toward a second target, a secondary reaction measurement can be performed. Neutron knockout from  $^{11}\text{Li}$  forms  $^{10}\text{Li}$ , which has no bound states so that the ultimate exit channel is  $^9\text{Li} + 2n$ . Detecting the  $^9\text{Li}$  and a neutron allows for the reconstruction of the  $^{10}\text{Li}$  momentum distribution after the knockout of the first neutron, [Fig. 3.33](#). If the target is a spectator, the  $^{10}\text{Li}$  momentum distribution is the complement of the momentum distribution of the removed nucleon. Thus, with the caveats concerning the reaction mechanism, the knockout reaction is a measure of the momentum wave function (as opposed to the more standard position representation) of one of the loosely bound nucleons. These data suggest that these valence neutrons are a mixture of  $2s_{1/2}$  and  $1p_{1/2}$  components. Note that the higher the  $\ell$  value, the broader the (linear) momentum distribution. The admixture of the second s state might seem surprising, as this level usually does not start filling until  $N = 14$ .

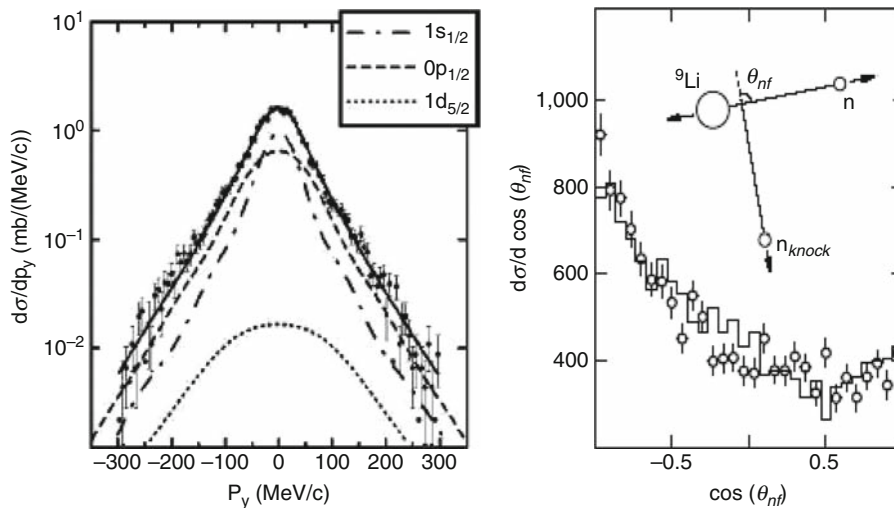
■ Fig. 3.32

Schematic view of the  $^{11}\text{Li}$  nucleus, in which the two valence neutrons are in orbits much larger than the  $^9\text{Li}$  core (Tanihata et al. 1985)



■ Fig. 3.33

Left:  $^{10}\text{Li}$  residue momentum distributions measured following neutron removal from  $^{11}\text{Li}$  on  $^{12}\text{C}$  at 287 MeV/A. Right: Angular correlations of the decay neutrons measured relative to an axis defined by the  $^{10}\text{Li}$  recoil direction as shown in the inset. The points are the experimental data and the histogram is a reconstruction corrected for experimental resolution and acceptance effects. Note the strong forward-backward asymmetry, which reflects interference of the  $\ell = 0$  and 1 final states



Its contribution for  $N = 8$  (in  $^{11}\text{Li}$ ) is thought to be a consequence of the tensor interaction between neutrons and protons (Myo et al. 2007).

*Knockout reactions*, such as  $(p, \alpha)$ ,  $(\gamma, \alpha)$ , and  $(e, e' \alpha)$  in even  $N = Z$  (alpha particle) nuclei are also especially important as they provide evidence for *alpha particle clustering* in nuclei. At low energies, such reactions, for example,  $^{19}\text{F}(p, \alpha)^{16}\text{O}$  and  $^{28}\text{Si}(\gamma, \alpha)^{24}\text{Mg}$ , which reduce the mass of the heavy partner, are important competitors to the synthesis pathways leading to the formation of elements just below  $^{56}\text{Fe}$  in nova bursts.

### 3.4.5 Mean-Field-Dominated HI Reactions

#### 3.4.5.1 Impact Parameter Dictates the Reaction Channel

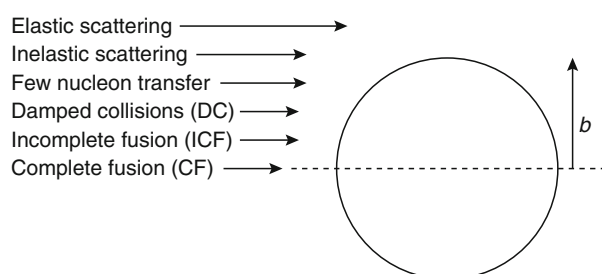
Nuclear chemists have been particularly active in the study of reactions between heavy ions (HI) and heavy nuclei. The interest can be traced to the fact that all heavy elements with  $Z > 101$  have been made with HI fusion–evaporation reactions (Loveland 2007). With increasing mass, the distinct quantal features become less important. Classical or quasiclassical reaction models become reasonable when the de Broglie wavelength becomes significantly smaller than nuclear dimensions. However, this condition is not satisfied in HI reactions with energies just exceeding the Coulomb barriers. Thus, quantal descriptions via a Time-Dependent Hartree-Fock (TDHF) approach (Bonche et al. 1976) or some form of quantum molecular dynamics (Feldmeier and Schnack 2000) are needed. In practice, semiclassical methods are usually invoked to describe the range of mechanisms observed at bombarding energies near the Coulomb barrier.

As the energy is increased well above the Coulomb barrier, classical concepts become more applicable and a partition of the impact-parameter space into different reaction types becomes reasonable. ▶ [Figures 3.34](#) and ▶ [3.35](#) illustrate the approximate relationship between reaction mechanism and impact parameter  $b$ , or  $\ell$ -wave, for collisions between two complex nuclei at energies of more than a few MeV/A above the barrier.

The classification scheme in ▶ [Fig. 3.35](#) becomes simplified for lighter projectiles, for which fusion and simple surface reactions are the principal exit channels at low relative bombarding energies. For very heavy projectiles, the *damped-collision* (*deep-inelastic*)

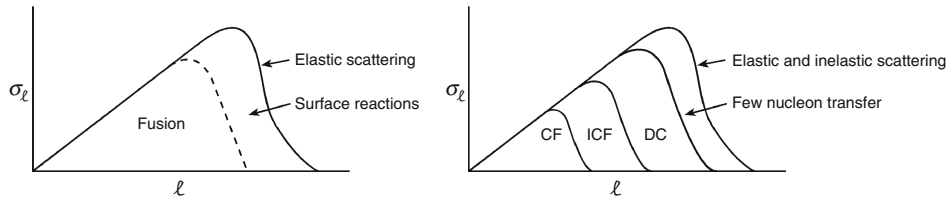
■ [Fig. 3.34](#)

Reaction mechanisms classified schematically according to relative impact parameter  $b$  ( $\ell$ -wave). Large values of  $b$  are classified as peripheral collisions and small values as central collisions



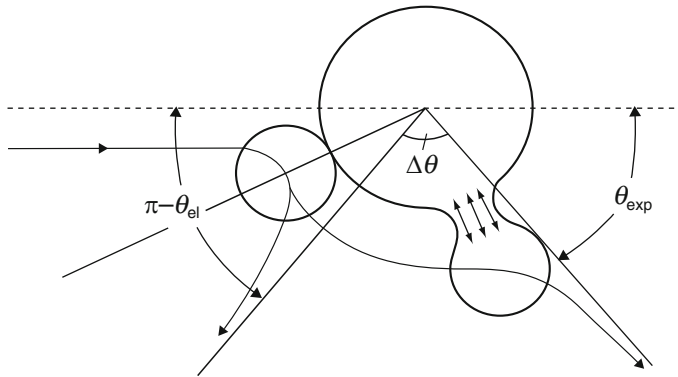
■ Fig. 3.35

Distribution of partial cross sections  $\sigma_\ell$  as a function of angular momentum quantum number  $\ell$ , decomposed according to reaction mechanism. Left panel is for light-ion-induced reactions (H, He) and right panel for heavy-ion reactions



■ Fig. 3.36

Illustration of a damped (deep inelastic) collision. The projectile trajectory is shown by the heavy curve and the extension of the original Coulomb-scattering trajectory by dashed lines. During the rotation angle of the dinuclear complex,  $\Delta\theta = \theta_{\text{el}} - \theta_{\text{exp}}$ , a neck is formed between the reacting species, through which nucleon exchange and energy dissipation proceed



mechanism is dominant as the mutual Coulomb field between the colliding particles becomes very large and inhibits fusion.

In the following subsections, the various mechanisms are discussed in order of decreasing impact parameter, beginning with elastic scattering and finishing with complete fusion.

### 3.4.5.2 Surface Reactions: Inelastic Scattering and Nucleon Transfer

For impact parameters with trajectories that scatter near the grazing angle, the separation between the colliding nuclei becomes sufficiently small that they begin to sample the attractive component of the nuclear potential. Reactions can then occur at the nuclear surface (leading to two-body final states) that proceed on a time scale comparable to the nuclear transit time. Interactions in this category usually involve excitation of low-lying modes in one or both of the colliding species and are particularly valuable for studying nuclear structure. Experimentally,

reactions at the nuclear surface are distinguished by: (1) angular distributions that peak in the forward direction or near the grazing angle, and (2) distinct spectral peaks, corresponding to energy states in the product nuclei.

### 3.4.5.3 Damped Collisions

At intermediate impact parameters, the nuclear overlap between target and projectile nuclei becomes sufficiently strong that the nuclear force may compete favorably with the repulsive Coulomb and centrifugal forces. When these competing forces approximately balance one another, it is possible to create short-lived dinuclear complexes, or “*nuclear molecules*” (► Fig. 3.36). These temporal species survive long enough to undergo a partial rotation and significant energy dissipation before undergoing binary breakup. Based on this behavior, these reactions are classified as *damped* or *dissipative* collisions, DC. The importance of the damped-collision mechanism relative to the total reaction cross section depends on the charge product  $Z_p Z_t$ . If the nuclear charge product is small, the DC cross section is also small. For collisions between very heavy nuclei, damped collisions may consume nearly the entire nuclear reaction cross section (Schröder and Huizenga 1977; Töke and Schröder 1992). While other processes become significant with increasing energy, for collisions between the heaviest nuclei, the bulk of the reaction cross section remains of this dissipative type up to several tens of MeV/A (Baldwin et al. 1995).

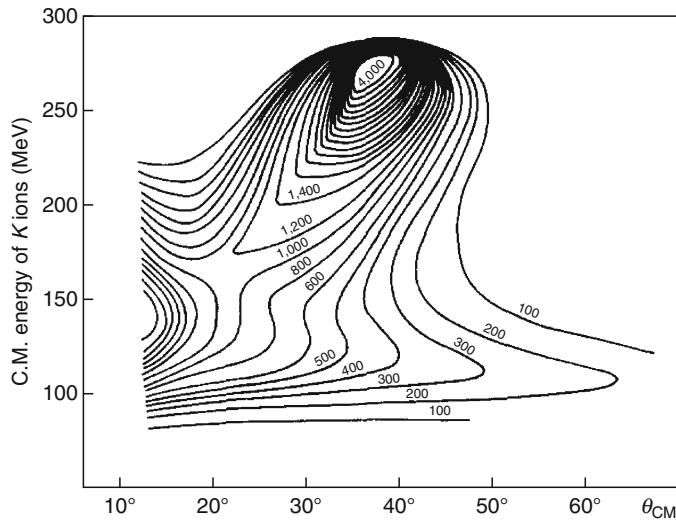
During the contact time, a neck forms between the reacting nuclei, through which statistical diffusion of neutrons and protons occurs in both directions (Planeta et al. 1990). It is this nucleon-exchange process that mediates the dissipation of radial kinetic energy into internal excitation energy. At the same time, extensive nucleon diffusion generates a broad distribution in both charge and mass around the projectile and target values. Thus the distinction between damped collisions and fission is that the product charge and mass distributions are concentrated near those of the projectile and target in the former case, but which for the latter are symmetric, near the total charge and mass divided by two (for all but the lowest excitation energies).

The angular and energy-damping features of the damped-collision mechanism are best illustrated by means of a Wilczynski plot (Wilczynski et al. 1973), shown in ► Fig. 3.37. This type of plot summarizes the probability for observing a projectile-like fragment in the  $^{40}\text{Ar} + ^{232}\text{Th}$  reaction as a function of scattering angle and total kinetic energy. Here the most energetic nonelastic fragments form a peak near the grazing angle, as mentioned in ► Sect. 3.4.5.1. As the energy damping increases, a ridge of events develops near the grazing angle, corresponding to quasi-elastic surface reactions. The broad band that appears for the largest kinetic energies defines the damped collision events. The kinetic energies of the fully damped fragments are consistent with fission fragment kinetic energy systematics (Viola et al. 1985). However, the damped-collision angular distribution is peaked near the grazing angle, unlike fission, which is symmetric about  $90^\circ$  in the center-of-mass system.

Theoretical calculations indicate that the rotation angle  $\Delta\theta$  (► Fig. 3.36) depends on the impact parameter. Smaller impact parameters lead to greater target and projectile overlap and thus longer rotation times, enhancing the degree of nucleon transfer and energy dissipation. Analysis of the data suggests that for fully damped events, the rotation time is about  $10^{-22}$  s. The dissipated energy appears in the product nuclei as excitation energy. The frictional forces during contact also impart sizeable angular momenta to the primary fragments. These excited,

■ Fig. 3.37

Double-differential cross section (indicated on plot); contours  $d\sigma^2/d\Omega dE$  for the 10MeV/A and  $^{40}\text{Ar} + ^{232}\text{Th}$  reaction plotted versus scattering angle and kinetic energy of projectile-like fragment (Wilczynski et al. 1973). The grazing angle is near  $40^\circ$  in this reaction



high-spin product nuclei subsequently cool by secondary particle emission to form the observed fragment  $Z$  and  $A$  distributions.

Because of the statistical nature of nucleon exchange, the nuclide distribution of the products extends over a very broad range of projectile-like and target-like fragments. This has made possible the identification of a large number of exotic nuclei that have significantly expanded knowledge of nuclear properties. By utilizing similar reactions at higher projectile energies (► Fig. 3.38), it becomes possible to create beams of radioactive nuclei for further exploration of important problems in nuclear reactions, structure, and nuclear astrophysics.

In order to explain the dissipation of large amounts of relative kinetic energy into internal excitation and shape degrees of freedom, microscopic transport theories based on statistical nucleon exchange have proven to be of broadest utility. Based upon a master-equation approach (Nörenberg et al. 1974, 1976; Randrup 1978), the macroscopic variables are accounted for qualitatively via a Fokker–Planck equation in which a drift coefficient describes the net flow of nucleons across the target–projectile interface and a diffusion coefficient that accounts for nuclear friction effects.

#### 3.4.5.4 Composite-Nucleus Formation

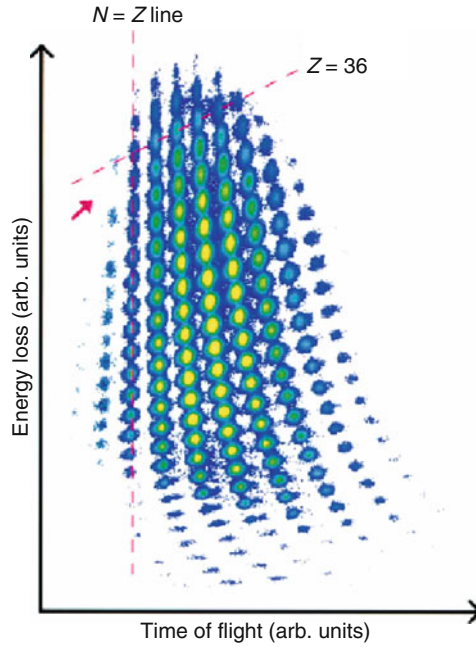
Total amalgamation of target and projectile corresponds to *complete fusion* (CF). If the composite completely samples the mononuclear phase space, a compound nucleus (CN) is formed.

If the barrier is robust, as it is for HI fusion, Wentzel–Kramers–Brillouin (WKB) logic can be used to generate the transmission coefficient (Gamow penetration factor) as a function of the energy of relative motion  $\varepsilon$  (as it is for spontaneous alpha-decay),



■ Fig. 3.38

Distribution of nuclides produced in the 75 MeV/A  $^{78}\text{Kr} + ^{58}\text{Ni}$  reaction. Atomic number increases along the vertical axis and mass number along the horizontal axis (From Pfaff et al. 1996)



$$T_\ell(\varepsilon) = \exp \left\{ -\frac{2}{\hbar c} \int_{R_{\text{in}}}^{R_{\text{out}}} \sqrt{2\mu c^2 [V(r) - \varepsilon]} dr \right\} \approx \exp \left\{ -\frac{2\pi}{\hbar \omega} \left[ V_C - \varepsilon + \frac{\ell(\ell+1)\hbar^2}{2\mu R_B^2} \right] \right\}. \quad (3.70)$$

Here  $\varepsilon$  is the energy of relative motion. In the first expression, the general WKB result is given in terms of the real potential  $V(r)$  and the classical inner and outer turning points,  $R_{\text{in}}$  and  $R_{\text{out}}$ , respectively. The second quantity gives the result if the potential is approximated by an inverted harmonic-oscillator potential of frequency  $\omega$ .  $R_B$  is the intranuclear separation distance at the peak of the barrier.)

From the expression for the transmission coefficient  $T_\ell$  it is seen that for sufficiently high angular momenta, the Coulomb plus centrifugal terms may exceed the available beam energy, leading to an upper limit to the angular momentum,  $\ell_{\text{max}}$ , that can contribute to fusion (Bass 1974). For slightly higher  $\ell$ -waves this limitation may produce *incomplete fusion* reactions in which only a part of the projectile is captured by the target.

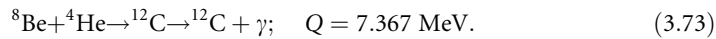
For heavy-ion reactions below the average  $\ell$ -value, fusion saturates as the energy is lowered yielding a transmission coefficient  $T_\ell$  and cross section nearly independent of  $\ell$  (Vandenbosch 1992). In this case, the fusion cross section with a center-of-mass energy  $E$ , reduces to

$$\sigma_{\text{CF}} = \frac{R_B^2 \hbar \omega}{2E} \exp \left[ -\frac{2\pi}{\hbar \omega} (V_C - E) \right]. \quad (3.71)$$

This expression, which predicts an asymptotic slope in energy of  $\ln[E\sigma(E)] = 2\pi/\hbar\omega$ , describes fusion excitation functions at low energy quite well. For deformed nuclei,  $R_B$  will depend on the relative orientation of the colliding pair, resulting in a distribution of effective fusion barriers. As a result, not only is it possible to observe fusion below the mean fusion barrier, but it is also possible to obtain information of the effective distribution of barriers contributing to fusion (Dasgupta et al. 1998). At subbarrier energies, coupling to inelastic channels can be considered as a “doorway” to fusion and thus coupling of such channels to the entrance channel can also be an important consideration (Brogia et al. 1983).

In some heavy-ion reactions a small fraction of the projectile mass may escape capture and proceed forward with the beam momentum. These reactions are called *incomplete fusion* (ICF) or *massive transfer*. The result of such incomplete fusion is, aside from the uncaptured fragment, an excited nucleus that is fully internally equilibrated and thus its decay is suitably treated by statistical models of compound nucleus decay, the subject dealt with in the next major section.

A special case of CN formation occurs when the capture proceeds through an isolated resonance reaction. Such reactions are also of fundamental importance to the nucleosynthesis pathways that form the elements beyond helium (see Chap. 12 in Vol. 2). The classic example here is the  $3\alpha \rightarrow {}^{12}\text{C}$  reaction



There are only three levels of  ${}^{12}\text{C}$  below  $E^* = 10 \text{ MeV}$ . One of these levels occurs at 7.654 MeV, just above the  $Q$ -value for the  ${}^8\text{Be}(\alpha, \gamma)$  reaction (also a resonance reaction). This level was predicted by F. Hoyle before it was observed, based on the fact that C (and life) exists. It is the resonance with this state that magnifies the  $3\alpha \rightarrow {}^{12}\text{C}$  cross section and provides the gateway to synthesis of heavier elements. More detailed discussions of resonance and neutron-capture reactions in astrophysics can be found in (Rolfs and Rodney 1988).

The two major decay modes of CN are light-particle emission and fission. The modeling of these decay modes is treated in the next section. In closing this section, it is pointed out that the spectra of light particles (of energy  $\varepsilon$  and type  $\tau$  emitted from a CN  $P(\varepsilon_\tau)$ ) is Maxwell–Boltzmann (like) in form, up-shifted in energy by a Coulomb barrier height ( $B_C$ ) if the ejectile is charged,

$$P(\varepsilon_\tau) \propto \varepsilon_\tau^x e^{-(\varepsilon_\tau - B_C)/T}. \quad (3.74)$$

The variable power  $x$  on the exponential prefactor (which determines the spectral rise at low energy) arises from: (a) statistical shape variations which affect the actual barriers, (b) a mixture of “volume” and “surface” emission, (c) the emission of more complex nuclei that subsequently decay into the channel of interest, and (d) quantum penetration. The first factor is the most important, and thus in fitting spectra, often a distribution of  $B_C$  values is required.

## 3.5 Statistical Decay

### 3.5.1 Preliminaries

Standard statistical-model treatments of compound nucleus decay are predicated on a time-scale separation between the formation of the CN and the time scales for simple (mostly single-particle) decay modes, as well as the massively collective decay process of fission. With

this decoupling of the entrance channel from the exit channel (except for conserved quantities), the CN decays statistically; that is, the decay samples all the phase space allowed by conservation laws (Ericson et al. 1963). The problem is always the identification and quantification of this phase space. As almost all reactions proceed through binary or sequences of binary steps, the rates of decays will be determined by the critical configurations of a binary nature. (The case of multifragmentation is thought to be an exception to this statement: see the end of this section and [Sect. 3.7.5](#).)

There have been two successful approaches to this quantification: the Hauser–Feshbach (HF) and the transition-state (TS) treatments. The former was historically used to treat light-particle emission and the latter to treat fission. Modern codes have extended HF to treat ejectiles as heavy as carbon and with the aid of calculations of conditional barriers, transition-state theory has been used to treat binary divisions with mass asymmetry in the decay channel as a continuous variable.

### 3.5.2 The Hauser–Feshbach Treatment of Particle Emission

The logic employed in the HF treatment (Hauser and Feshbach 1952), as well as the earlier WE treatment (Weisskopf and Ewing 1940) the which lacks proper consideration of angular momentum coupling, is that the one-way decay rate would be equal to the reverse rate if true reactant–product equilibrium were attained. The one way, state-to-state probability for a fixed  $\ell$ -value and energy is readily given by the transmission through the optical model potential,  $T(\varepsilon)$ . This rate would be equal, by microscopic reversibility (mechanics is time-reversal invariant), to the outgoing state-to-state probability. Thus an observable rate is simply the microscopic (state-to-state) rate times the density of final states. The latter reflects the number of possible final microstates within an experimental window. This window is naturally quantized by angular momentum and is quantized in energy either by the discrete structure of the quantum system or, at modest excitation energy, by the number of overlapping states in an energy bite determined by an experimental energy resolution, i.e.,  $\omega dE$ , where  $\omega$  is the state density.

While the forward and backward rates would be equal and thus cancel, giving no net rate in an imagined equilibrium, in the kinetic process the net-rate (unconfined to a box and thus with no backward rate) is equal to the outgoing one-way rate. Thus the rate of emission of nucleons or clusters in any specified state from an initial parent level of excitation energy  $E_i$  and spin  $J_i$  is the result of a sum over the product intrinsic state-to-state rates and final-state level densities, where the sum is over: (a) the possible  $\ell$ -values (inner sum [Eq. \(3.76\)](#)) and (b) the so called “channel spin”  $S = j + s$ , where  $j$  and  $s$  are the intrinsic spin of the residual and ejectile spin (outer sum). With consideration of the possible spin combinations, the HF equation for the emission rate  $R_{i \rightarrow f}$  of a particle of type  $\tau$  energy  $\varepsilon_\tau$  and separation energy  $S_\tau$ , in terms of the inverse cross section  $\sigma_{f \rightarrow i}$  and the density of levels of the parent  $i$  and the daughter  $f$  is,

$$R_{i \rightarrow f}(E_i, J_i \rightarrow j, s) dE = \frac{2\lambda^2}{h} \sigma_{f \rightarrow i}(E_i, J_i) \left( \frac{(2s+1)(2j+1)}{(2J_i+1)} \right) \left( \frac{\omega_f^L(E_f, j)}{\omega_i^L(E_i, J_i)} \right), \quad (3.75)$$

with

$$\sigma_{f \rightarrow i}(E_i, J_i) = \pi \lambda^2 \sum_{S=|j-s|}^{S=j+s} \sum_{\ell=|J_i-S|}^{\ell=J_i+S} \left( \frac{2J_i+1}{(2s+1)(2j+1)} \right) T_\ell^\tau(\varepsilon), \quad (3.76)$$

and

$$E_f = E_i - S_e - \varepsilon_e. \quad (3.77)$$

In order to execute this logic, the following must be known: (1) the ejectile spin, mass, and separation energy and (2) the density of levels (as a function of excitation and angular momentum) of the parent (i) and daughter (f). As the latter has lower mass (and perhaps charge), as well as excitation energy, its level density will be smaller than that of the parent.

Monte Carlo codes are available that execute this logic event-wise, removing energy in each step until particle emission can no longer occur. Some codes seamlessly switch to gamma emission until all products are in their ground states. Since the HF equations treat ejectiles as objects with only one quantum option (there is no ejectile density of final levels), each level in a complex ejectile must be treated as a separate channel. Some modern codes (e.g., GEMINI) have used this logic to treat complex ejectiles (level by level) as heavy as C isotopes (Charity et al. 2001). Such codes are indispensable for calculating decays initiated by the low-energy accelerators located in hospitals for isotope production, for evaluating concepts for transmutation of nuclear reactor waste, and as afterburners for treating the statistical decay that invariably results after fast (nonstatistical) processes originating in high-energy collisions, including those initiated by cosmic rays.

### 3.5.3 The Transition-State Treatment of CN Decay

In the 1930s Eyring, Polanyi, and Wigner developed transition state (TS) theory, which is a computationally efficient way to compute *classical* reaction rates without integrating trajectories. The main idea is to define a dividing surface that partitions the configuration space into reactant and product sectors and compute the rate from the directional phase-space flux through this surface. One complication (below) is that the dividing surface must be such that it is not recrossed. The transition-state logic was almost immediately applied to fission by Bohr and Wheeler (1939). (See Vandenbosch and Huizenga (1973) or Wagemans (2000) for a detailed presentation of fission data and theory.) In this case, the absolute decay width (at an excitation energy above the ground state  $E^* = E - V_{\text{gd.st.}}$ ) comes from an integral over the density of levels from the point where the energy in the decay channel  $\varepsilon$  is zero (i.e., maximal energy to be dispersed among the nondecay degrees of freedom and thus maximal level density) to the maximum channel energy (where there is a minimum of energy in the coordinates other than the decay channel),

$$\Gamma_f^{\text{BW}} = \left( \frac{1}{2\pi\omega_{\text{mn}}^{\text{L}}(E^*)} \right) \int_{\varepsilon=0}^{E^*-B_f} \omega_{\text{sp}}^{\text{L}}(E^* - B_f - \varepsilon) d\varepsilon. \quad (3.78)$$

The critical aspect in executing the TS logic is consideration of how the density of levels of the mononuclear (spherical or marginally deformed) parent ( $\omega_{\text{mn}}^{\text{L}}$ ) grows with excitation energy as compared to growth of the density of levels of the highly deformed saddle-point shape ( $\omega_{\text{sp}}^{\text{L}}$ ). The logic employed in statistical model codes is to calculate the level-density parameter via a physical expansion, increasing its value in proportion to the surface area. Following the prescription of Ignatyuk et al. (1975), Reisdorf (1981), and Töke and Swiatecki (1982), the level density parameter  $a$  (see ▶ Eq. (3.66)) can be written as a physical Liquid Drop Model-like expansion in terms of a deformation parameter  $q$ . In such an expansion, one has

constants for the volume  $c_v$  and surface  $c_s$  contributions, where the latter is multiplied by the surface area at deformation  $q$  relative to that of a sphere ( $B_s(q)$ ),

$$a(q) \approx c_v + c_s A^{2/3} B_s(q). \quad (3.79)$$

The complication that the transition state cannot be recrossed was dealt with theoretically by Kramers (1940), where the fission width is reduced relative to the Bohr–Wheeler estimate by saddle recrossing. As the recrossing probability increases with friction, the reduced fission probability can be cast in terms of the friction coefficient  $\gamma$ ,

$$\Gamma_f^{\text{Kram}} = \left[ (1 + \gamma^2)^{1/2} - \gamma \right] \Gamma_f^{\text{BW}} \quad (3.80)$$

The importance of this correction is still being debated (McCalla and Lestone 2008). However, it is included in most modern decay codes.

In the early 1980s data on so-called complex fragment (CF) statistical emission became available. Complex fragments are usually defined as those with atomic numbers from three to one half the total mass of the system. The first data, shown in [Fig. 3.39](#), demonstrated the statistical nature of the emission and were used to extract conditional barriers; that is, barriers that correspond to the minimum energy required to pass from the CN system to an exit channel of fixed mass asymmetry. A general TS theory for treating CF emission was presented by Moretto (1975). This theory exchanges the problem of calculating transmission coefficients (needed for HF) with calculating the barrier and density of levels for the conditional barriers, i.e., barriers with frozen mass asymmetry. As mentioned above, the best modern codes allow for either scheme to be used.

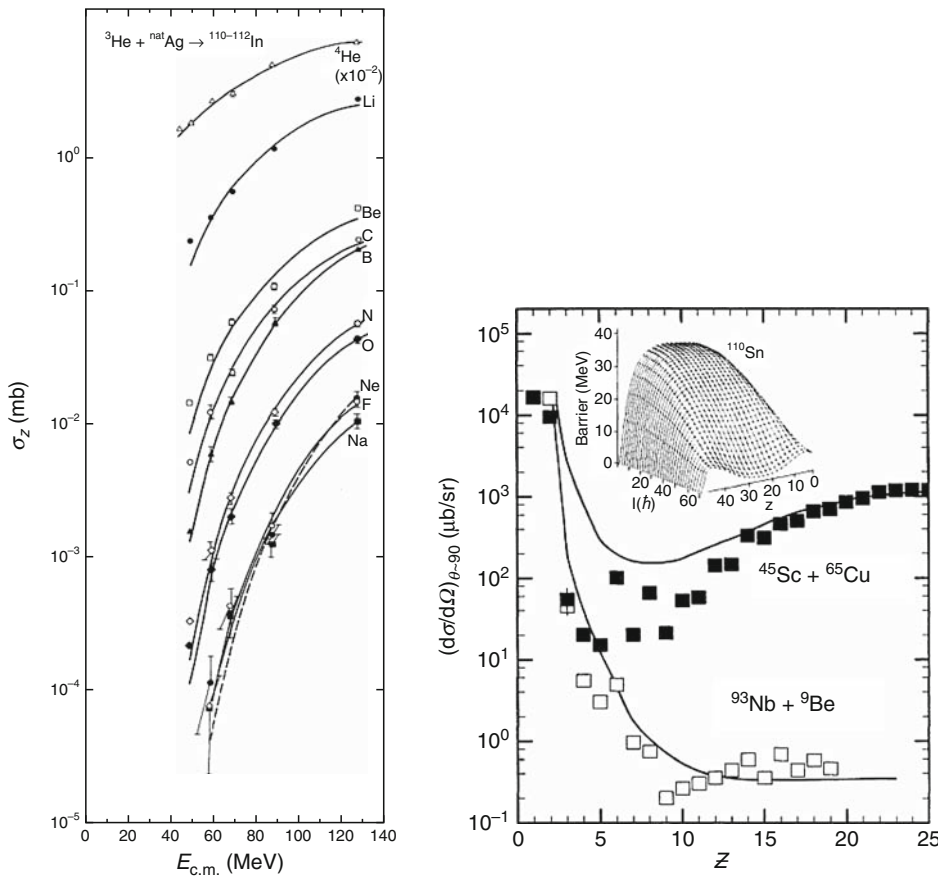
### 3.5.4 The Density of States of Highly Excited Nuclei

A complete presentation of the issues related to the properties of what are often called “hot nuclei” is given in Shlomo and Kolomietz (2004). One of the assumptions underlying both of the standard treatments is that the reverse process can be considered as capture onto an object that bears significant resemblance to the ground state of the daughter. The macroscopic forward (decay rate) is then just the microscopic rate multiplied by the appropriate density of states. However, at high excitation energy nuclei will expand, with some reduction of the central density and the surface becoming far more extended. This poses two problems. First, the OM might not provide correct transmission coefficients, as the excited objects of relevance have different correlations than those of the ground state. The second problem is that even for uncorrelated fermion systems, the relevant density of states should be for the extended object.

From a schematic model the qualitative effects of expansion are shown in [Fig. 3.40](#) (Sobotka et al. 2004). Calculations based on realistic effective Hamiltonians (Samaddar et al. 2007, 2008) yield similar results. With increasing excitation energy per nucleon, the equilibrium state (which for an isolated system is that with the maximum entropy) is one with reduced density. This effect increases the level-density parameter (see dotted line in [Fig. 3.40](#), right hand side). Many-body theory (Prakash et al. 1983) has provided insight into how the effective mass terms evolve with density and excitation energy. In a local-density approximation (i.e., the level density parameter  $a$  can be calculated as the sum of contributions from different density regions of a nucleus), the  $k$ -mass ( $m_k$ , see [Eq. \(3.57\)](#)) increases from 0.7 to 1 with decreasing density and the peak of the  $\omega$ -mass ( $m_\omega$ ), at the nuclear surface is removed with excitation energy (see [Sect. 3.3.3](#)). The effect of the  $k$ -mass is to suppress  $a$  at low excitation but to

■ Fig. 3.39

**Left:** Excitation functions for complex fragment evaporation from a  $^3\text{He}$ -induced reaction (Mcmahan et al. 1987). **Right:** Mass distribution generated from the decay of  $A \approx 110$  systems at both low and high angular momenta. The inset shows the finite-ranged Droplet Model conditional-barrier distributions (Sobotka et al. 1987)



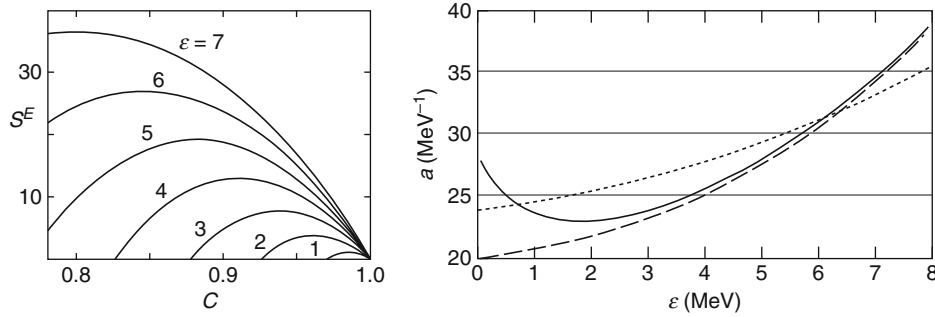
increase it with increasing excitation. This evolution provides positive feedback to expansion, feedback that is active over several MeV/A of excitation. On the other hand, the collapse of the  $\omega$ -mass at the nuclear surface (which was responsible for increasing  $a$  at low excitation) drives  $a$  down over the first few MeV/A of excitation energy. The collective effect is a variation of the density of states that yields a “Caloric Curve,”  $E^*(T)$ , with a pseudo plateau. While not a *phase* transition in the classical sense, these effects represent a transition from a correlated fermion system to one that more closely resembles a hot, but noninteracting Fermi gas.

### 3.5.5 Thermodynamic Models for Multifragmentation

Multifragmentation is thought to involve a nearly simultaneous breakup of the nucleus into many fragments. This image of the process suggests that the relevant phase space is that

■ Fig. 3.40

**Left:** The mononuclear excess entropy (above that for a nonexpanded system) as a function of a self-similar expansion coordinate (inverse of scaled radius parameter, i.e.,  $C = 1$  no expansion), for unit (MeV) steps in the excitation energy per nucleon  $\varepsilon$ . **Right:** The level density parameter with expansion but  $m^*/m = 1$  (dotted), considering both expansion and the evolution of  $m_k$  (dashed) and expansion with both  $m_k$  and  $m_\omega$  (solid) are shown (Sobotka et al. 2004)



corresponding to any number of fragments in the exit channel (rather than just two as in the HF and TS treatments). Statistical models of this phase space have been generated based on fixed energy and particle number – microcanonical ensemble, ‘Gross (1990) and Bondorf et al. (1985); fixed temperature and particle number – canonical, Das et al. (2005), and fixed temperature and chemical potential – grand-canonical, Randrup and Koonin (1981). As would be expected, such models predict a liquid–gas phase transition for large, uncharged nuclear systems, as discussed in Sect. 3.7. These models do reproduce a considerable amount of data. Having done so, it has been the hope that manifestations of the infinite-system phase transition in a finite system is also represented. To give the flavor of these approaches, the canonical prescription (for one particle type) is presented here.

The first assumption is that the partition function  $Q$  is the product of the individual partition functions for the component parts, corrected for indistinguishability,

$$Q_A = \sum_i \prod_i \frac{1}{n_i!} \left( \frac{V_{\text{free}}}{\Lambda} \right)^{n_i} (q_i)^{n_i}, \quad (3.81)$$

where the sum is over all possible partitions, the product is over the fragments in that partition,  $n_i$  is the number of a given fragment type ( $i$ ) in this partition,  $q_i$  is internal partition function for cluster type  $i$ , and the factor in parenthesis is the free volume measured in units of the thermal box size

$$\Lambda = \lambda_{\text{th}}^3 = \left[ \frac{h}{(2\pi mT)^{1/2}} \right]^3. \quad (3.82)$$

The average number of clusters of type  $i$  is

$$\langle n_i \rangle = \left( \frac{V_{\text{free}}}{\Lambda_i} q_i \right) \frac{Q_{A-i}}{Q_A}. \quad (3.83)$$

The partition function (for  $A$  particles) can be readily calculated from a recursion relation (Das et al. 2005). The result of particle number conservation in each partition is,

$$Q_A = \frac{1}{A} \sum_{k=1}^A k \left( \frac{V_{\text{free}}}{A_k} q_k \right) Q_{A-k}. \quad (3.84)$$

The execution of this logic then comes down to specifying the internal partition function for each unit  $q$ . For nucleons, with no internal degrees of freedom,  $q = 1$  (neglecting spin). For clusters,  $q$  is calculated from the Helmholtz free energy estimated using a liquid-drop model to calculate the internal energy and the Fermi-gas model to calculate for the entropic contribution to the Helmholtz free energy  $F$ , i.e.,

$$q_k = \exp[-F/T] = \exp[(W_0 k - \sigma(T)k^{2/3} + T^2 k/\varepsilon_0)/T]. \quad (3.85)$$

$W_0$  and  $\varepsilon_0$  are constants, while  $\sigma(T)$  models a surface free energy that goes to zero at a critical temperature.

This model is logically consistent and when extended to two particle types (for neutrons and protons, see Das et al. 2005) can reproduce many experimental observables. However, its main shortcoming is that it neglects interactions between the clusters. This leads to unphysical effects such as regions of negative heat capacity. This is inconsistent with thermodynamics and is well known to result from unphysical Hamiltonians. This has been made clear by both molecular (Lovett 2007) and mock nuclear systems, simulated with Lennard–Jones-type interactions (Campi et al. 2005). That is, if one considers the interactions that are active at the inter- (as well as intra-) cluster level, regions of negative heat capacity largely disappear as long as the system is truly ergodic. The later well-known qualification is demonstrated by the recent molecular dynamics work of Thirring et al. (2003).

### 3.6 Mechanisms in the Nucleon-Nucleon Domain

Once the projectile energy significantly exceeds the Coulomb barrier, nucleon-nucleon (N-N) scattering in the early stages of the target–projectile interaction may generate nucleons or clusters that are sufficiently energetic to escape the mean field of the composite system. These fast *nonequilibrium processes* begin to appear when the projectile energy per nucleon approaches the *Fermi energy*  $\varepsilon_F$ . In the Fermi Gas Model, the nucleus is treated as a degenerate gas of spin  $\frac{1}{2}$  particles confined within the nuclear volume. The Fermi energy  $\varepsilon_F$  can be defined as the kinetic energy measured from the bottom of a one-body potential (a positive quantity) or the binding energy of the last nucleon (a negative quantity). By the former measure,  $\varepsilon_F$  is about +30 MeV for both neutrons and protons in nuclei near the valley of stability. By the latter measure,  $\varepsilon_F$  is equal in magnitude to the binding energy but opposite in sign. Thus, by the latter measure,  $\varepsilon_F \approx -8$  MeV for both neutrons and protons in nuclei near beta stability but diverge from one another as the neutron/proton asymmetry deviates from stability, with ultimately the value of the nucleon type in excess decreasing to zero at the drip line. The kinetic energy view is a very useful concept for many reactions and is used below, but one has to appreciate that this approach views the nucleus as a collection of independent particles, i.e., no correlations. (The latter definition is more useful for nuclear structure and does not suffer from the one-body model assumption.)

Experimentally, nonequilibrium phenomena become apparent above projectile kinetic energies of about 20 MeV per projectile nucleon, which is comparable to the Fermi energy of nucleons in the nuclear potential well. These processes grow in both probability and complexity with increasing beam energy (Durand et al. 2001).



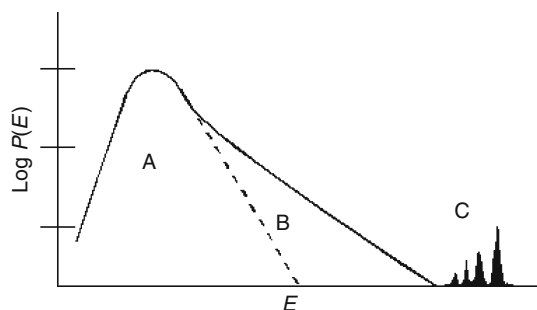
Nonequilibrium phenomena are distinguished by two principal features. First, they occur on a time scale much shorter than the typical equilibration time for statistical decay of a compound nucleus ( $\tau \approx 10^{-21}$  s). Second, they produce multiparticle final states that are subsequently followed by statistical decay of the excited heavy product. In normal kinematics ( $A_p < A_t$ ), the energetic light particles or clusters are forward-peaked and form a distinct exponential tail (area B in [Fig. 3.41](#)) on the Maxwellian spectra produced in later evaporation stages (area A in [Fig. 3.41](#)). The preequilibrium component for the nucleon channels is as in by early stage emissions of the multistep compound model, as in by the FKK model for example. At the extreme of nonequilibrium emissions are the discrete peaks (labeled C), which correspond to direct reactions, or the first step in a multistep compound model.

The same partition of the cross section seen in the light-particle emission is observed in the *linear momentum transfer* (LMT) to the heavy reaction partner, [Fig. 3.42](#). The folding angle between correlated binary fission fragments can be used as a gauge for measuring the degree of LMT in a reaction with a highly fissionable target, i.e., one for which  $\sigma_R \approx \sigma_f$ . In this context, LMT = 1.0 corresponds to a complete fusion (CF) reaction in which the total projectile momentum is transferred to the composite system, yielding the maximum excitation energy. LMT = 0.0 ( $\theta_{\text{corr}} \approx 180^\circ$ , [Fig. 3.42](#)) indicates a quasi-elastic mechanism that deposits only a small amount of momentum and excitation energy in the heavy product nucleus. At low bombarding energies, most of the reaction cross section goes into complete fusion reactions, with simple transfer events forming a peak near  $180^\circ$ . With increasing projectile energy, the high LMT peak broadens and shifts toward lower LMT due to the onset of nonequilibrium contributions in which incomplete fusion or prompt light particles carry off some of the projectile momentum, thus decreasing the deposited excitation energy. At the highest bombarding energies, the LMT distribution becomes nearly flat, indicating the deposition of a continuous spectrum of excitation energies, but with diminishing probability for complete fusion of target and projectile as the beam energy increases. Above beam energies of 100 MeV/A, the probability for complete fusion events is very low.

For nonfissionable systems, similar effects of the increase in nonequilibrium phenomena with increasing beam energy can be observed by measuring the velocity distribution of heavy residues relative to the expected velocity for complete fusion events. This approach is especially

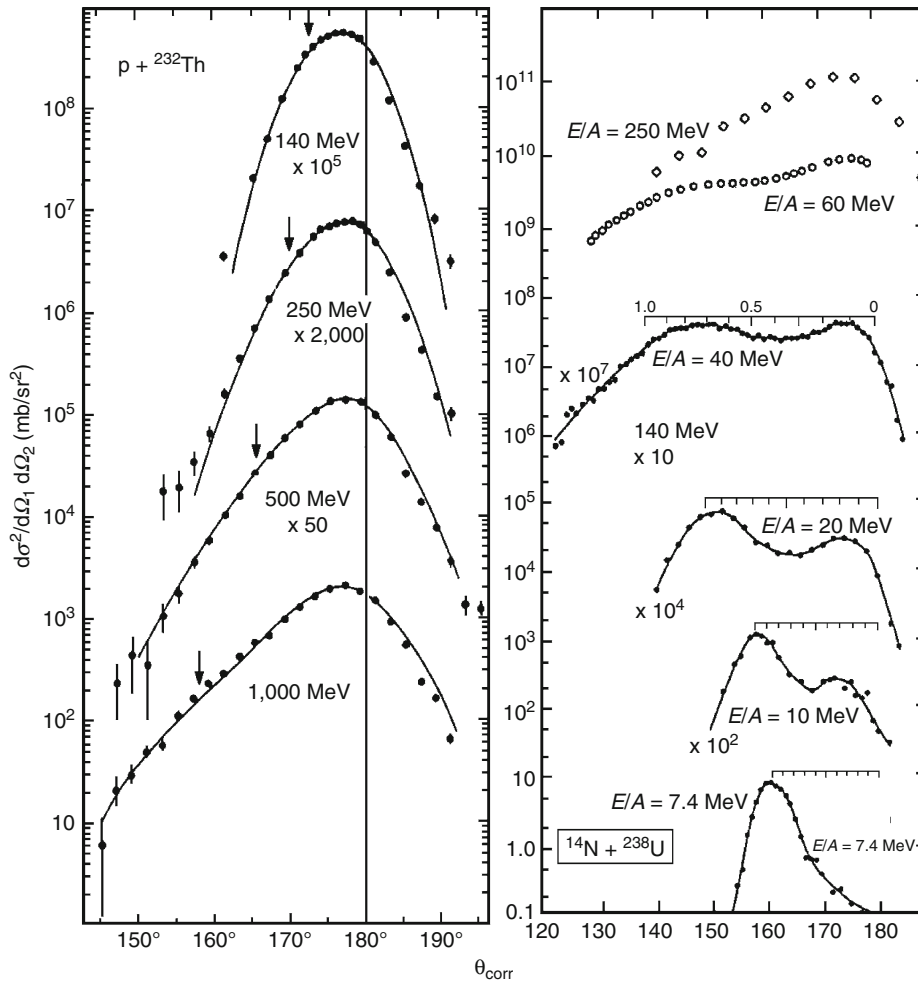
**Fig. 3.41**

Kinetic energy spectrum at forward angles for emission of light particles. Region A corresponds to evaporation from an equilibrated compound nucleus; region B describes preequilibrium emission, and C indicates the excitation of discrete states in direct reactions



■ Fig. 3.42

Diagram of the evolution of nuclear reaction mechanisms from the mean-field to nucleon-nucleon regimes as a function of projectile kinetic energy per nucleon  $E/A$ , as measured by the angle between coincident fission fragments  $\theta_{\text{corr}}$ . Correlation angles nearer  $180^\circ$  designate incomplete momentum transfer. The left frame shows the evolution for a proton-induced reaction on  $^{232}\text{Th}$ ; arrows indicate  $\theta_{\text{corr}}$  values for CF (Saint-Laurent et al. 1984). For the right-hand frame, the bar above each plot indicates the LMT scale (1.0 corresponds to CF) for the  $^{14}\text{N} + ^{238}\text{U}$  reaction. The two peaks correspond to fusion-like and quasi-elastic processes (Tsang et al. 1984; Fatyga et al. 1985). In all cases, the correlations are broadened by neutron evaporation from the fission fragments



useful in reverse-kinematics studies, where the heavy residues have appreciable kinetic energies. Both the fission-fragment correlations and residue-velocity distributions demonstrate that energetic collisions produce a wide spectrum of nonequilibrium reaction mechanisms that vary with the projectile–target composition and bombarding energy.

The organization of this section proceeds as follows: Relatively simple nonequilibrium phenomena observed in reactions near the Fermi energy are initially discussed. The subsequent sections deal with: models designed to account for the complex reactions that occur at intermediate energies ( $E/A > 20$  MeV), a simplified participant–spectator model to account for the reaction observables, and finally, reactions at sufficiently high energy to generate nuclear material with densities significantly in excess of normal nuclear density.

### 3.6.1 Reactions Near the Fermi Energy

The role of nonequilibrium emission as an intermediate mechanism, linking prompt one-step reactions to statistical particle evaporation from an equilibrated system, is most transparent in the proton spectra of light-ion-induced reactions on complex nuclei (Wu et al. 1979). The exponentially falling, or *preequilibrium*, component (B) in [Fig. 3.41](#) can be viewed as arising from a time-dependent process in which particles are emitted as the energy density in the initial target–projectile interaction zone randomizes throughout the nuclear volume: the lower the particle energy, the later in the process the particle was emitted. Two-component fits to the spectral shapes of components A and B yield slope temperatures consistent with an equilibrated Fermi gas for the statistical component, but slope temperatures are two-to-four times higher for the preequilibrium part, indicating emission from an earlier, hotter stage of the reaction.

Preequilibrium effects also appear in the excitation functions for heavy reaction products in this energy regime. The product yields shown in [Fig. 3.11](#) reach their peaks at bombarding energies consistent with compound nucleus formation; however, all excitation functions have appreciable cross-section tails that extend to higher bombarding energies. For example, in the reaction



the yield of  ${}^{198}\text{Tl}$  ([Fig. 3.11](#)) persists to much higher energies than predicted by compound nucleus energetics, because at least one of the emitted neutrons is of preequilibrium origin and carries off more energy than an evaporated neutron. The lowering of the average excitation energy due to preequilibrium emission reduces the probability for sequential evaporative emission and thus serves to hinder attempts to produce nuclei far from stability by increasing the beam energy.

For bombarding energies well above the barrier, one also observes the preequilibrium emission of intermediate-mass fragments ( $2 < Z < \sim 20$ , or IMFs) in reactions on heavy nuclei. The reaction observables for IMF emission strongly resemble those for light particles and presumably occur on a comparable short time scale. Models based upon a coalescence concept (Bond et al. 1977) have met with some success for light clusters, but encounter more difficulties for IMFs.

The experimental observables ascribed to the preequilibrium mechanism have usually been interpreted in the context of the *exciton model* (Griffin et al. 1966; Blann et al. 1975). In the basic model, the nucleus is treated as a Fermi gas in which the projectile initiates a series of sequential N–N collisions, generating unstable particle-hole states, or excitons (*exciton* = a particle-hole pair). The number of excitons is thus proportional to the degree of thermalization.

Large exciton numbers imply multiple collisions for which the projectile energy is partitioned among many nucleons likely to be in bound (single-particle) states, yielding high

excitation energies. Conversely, when only a few excitons are involved (few collisions), much larger energy transfers must occur and particles are raised to unbound states that yield energetic particle emission, leaving the heavy partner in a low state of excitation. Refinements of the model now include numerous physical effects such as the treatment of the nuclear potential and N-N mean-free path, Pauli blocking, barrier penetration, and finite-state lifetimes (Gadioli and Hodgson 1992; Chadwick and Oblozinsky 1992).

### 3.6.2 Models of Collision Dynamics

While the exciton model and its derivatives have been relatively successful in describing light-ion-induced reactions near the Fermi energy, the reaction mechanism becomes more complex at higher energies or when heavy-ion projectiles are involved. A major complication is introduced when multiple nonequilibrium processes occur during the evolution from initial target-projectile contact to the internally equilibrated final state. This problem is frequently approximated by a two-step model that assumes a fast collision stage followed by statistical decay of the system at a much later time ( $\tau > 10^{-21}$  s). The fast stage (time scale  $\tau \approx 10^{-22}$  s) is described by models that attempt to account for mass and energy dissipation during the collision. The second stage is governed by statistical decay mechanisms such as particle evaporation and fission, as discussed in [Sect. 3.5](#).

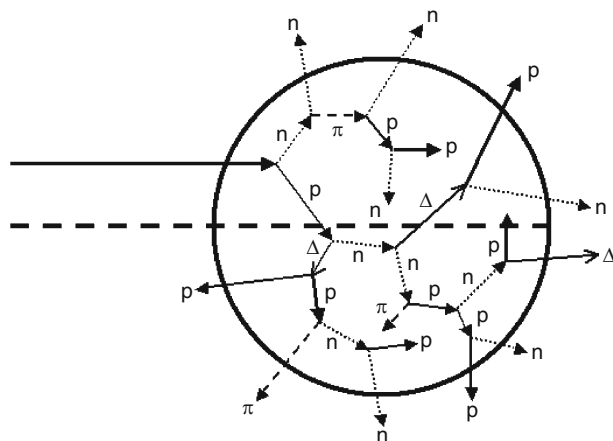
For reactions well above the Fermi energy ( $E/A > 100$  MeV), the *intranuclear cascade* (INC) model (Serber 1947) has been frequently employed. For projectiles with de Broglie wavelengths much smaller than the average internucleon separation distance in the nucleus, all nucleon-nucleon collisions can be treated as quasi-free N-N scatterings. The projectile is assumed to follow a semiclassical path and initiate an N-N interaction that generates a cascade of scatterings in three dimensions. The cascade is computed numerically until all available projectile energy is dissipated into either fast cascade particles that leave the system or into internal excitation energy of the target residue. [Figure 3.43](#) shows the schematic concept of the INC model.

The INC model is a phenomenological approach that employs experimental N-N scattering cross sections and angular distributions as a function of energy up to several GeV. Nuclear geometry is incorporated to deal with nuclear surface effects for large impact parameters and a Fermi-gas model with Coulomb barrier effects is used to evaluate the number of fast cascade particles that escape, as well as those that are thermalized and converted into excitation energy. Monte Carlo methods are used to select the impact parameter in each event as well as the scattering angles. For heavy-ion reactions, where multiple primary N-N collisions become possible in the initial contact stage, account must be taken of the vacancies created by these collisions. At energies for which meson production and excitation of the intrinsic resonance states of the nucleon (e.g.,  $\Delta$ ,  $N^*$  etc.) become possible, the scattering cross section for these types of reactions must be included, as well as the reabsorption probability of the mesons and decay of the nucleon excited states. At proton energies of several GeV and above, the growing number of meson types and resonance states introduces an additional complication, since there is limited experimental guidance for estimating these scattering cross sections.

INC codes – e.g., ISABEL, Yariv and Fraenkel (1981), and QGSM, Toneev et al. (1990) – are relatively successful in reproducing the fast cascade component of the reaction observables for light-ion-induced reactions above 100 MeV. They also predict the qualitative result that a broad distribution of excitation energies will be produced due to impact-parameter-dependent

■ Fig. 3.43

Simplified schematic picture of an intranuclear cascade event for an energetic proton incident on a heavy nucleus. The number of scatterings increases as the impact parameter decreases



transparency effects, with the maximum usually being well below the maximum possible excitation energy. Quantitative predictions of the excitation energy are more problematical. This uncertainty stems from the simple approximations relative to the nuclear potential that became important in terminating the cascade in its latter stages.

For heavy-ion reactions, an additional complication with the INC model is that it ignores mean-field effects, which become relevant when there is extensive mixing of target and projectile nucleons. This shortcoming has been addressed via a microscopic theory based on the *Boltzmann–Uehling–Uhlenbeck* (BUU) formalism (Bertsch et al. 1984); and variations (Gregoire et al. 1985). In this formalism, the time evolution of the mean-field is described by a one-body density-distribution function that is solved simultaneously with a nucleon-nucleon collision integral, thus accounting for both the mean field and N-N collisions. The collision integral is calculated via an intranuclear cascade where only scattering into unoccupied phase space cells is allowed.

Models of this type have proven effective in describing the multiplicities and spectra for energetic nucleons (Durand et al. 2001), as well as small-angle particle-particle correlations and integrated spatial distributions (Bauer et al. 1992). In confronting theory with heavy residue data, BUU-type calculations encounter two principal shortcomings, both of which are also present in INC calculations: first, the time at which thermalization has been achieved and second, the lack of density fluctuations in the model that would provide a mechanism for the formation of nuclear clusters. In an effort to develop a full dynamical theory of fragment production, density fluctuations have been incorporated via the classical *molecular dynamics* (MD) approach (Schlagel and Pandharipande 1987), which has led to several quantal dynamical models (QMD) such as fermionic molecular dynamics (Feldmeier et al. 1995; Feldmeier and Schnack 2000), antisymmetrized molecular dynamics (Ono and Horiuchi 1996), and Brownian one-body dynamics (Chomaz et al. 1994).

Both BUU- and QMD-like models can be used to investigate the *nuclear equation of state* (EOS) and the phase diagram for nuclear matter shown schematically in Fig. 3.3. One parameter of particular concern is the nuclear incompressibility constant  $K$  (a subject dealt

with in the next section). From measurements of spatial flow distributions of emitted light ions, it has been possible to determine the bombarding energy at which the transition from the mean-field to nucleon-nucleon scattering dominance occurs; i.e., the “balance energy” where attractive mean-field scattering becomes equal to repulsive nucleon-nucleon scattering (Magestro et al. 2000).

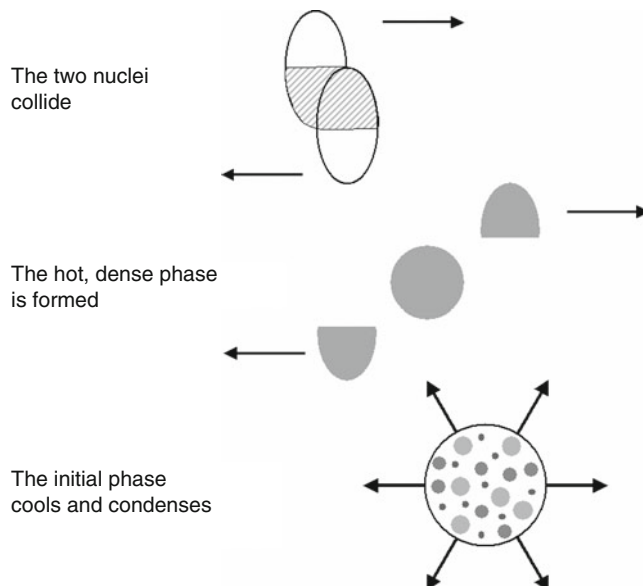
The collision models also demonstrate how nuclear reactions can be used to explore variations from normal nuclear density  $\rho_0$ , ranging from dilute ( $\rho < \rho_0$ ) to compressed ( $\rho > \rho_0$ ) states, by varying the bombarding energy and target–projectile asymmetry. For example, proton-induced reactions above about 5 GeV may leave the heavy partner in a state of depleted density due to the near-instantaneous knockout of several fast cascade particles. At the other extreme, in symmetric heavy-ion collisions, the large target–projectile overlap region in central collisions leads to significant compression and high energy density in the early stages of the reaction.

### 3.6.3 Participant–Spectator Reactions

For heavy-ion collisions well above the Fermi energy, models predict a low probability for composite-nucleus formation. Instead, most of the cross section is predicted to go into reactions that can be generalized as “*participant–spectator*” reactions (► Fig. 3.44). In the participant–spectator scenario, the *participant* source is defined by those nucleons that occupy the geometrical overlap volume of the target and projectile, which is impact-parameter dependent.

► Fig. 3.44

**Schematic picture of the participant–spectator model. The hot participant region is formed from nucleons in the target–projectile overlap region. The target and projectile remnants on the periphery act as spectators, which then decay statistically**



The number of participant nucleons and the energy-density of this localized source increase with decreasing impact parameter. The *spectators* are the target and projectile remnants outside the overlap volume and they decouple from the participant source on a time scale that decreases with increasing projectile energy and then decay statistically. The excitation energy of these spectators is a function of the overlap region.

Studies of the projectile spectator, or *projectile fragmentation*, permit investigation of nuclei at extremes of temperature and neutron–proton asymmetry (nuclei with large *isospin* components). By employing reverse kinematics, nuclei of all the elements can be studied. Because of the broad range of impact parameters that contribute to projectile-fragmentation events, the nuclidic yield distribution is very broad in  $N$  and  $Z$ , with the resultant formation of product nuclei far from stability. Exploitation of this result has led to the discovery of many new neutron- or proton-rich nuclei and provided access to a greatly expanded nuclear landscape for nuclear structure and nuclear astrophysics studies. One of the more intriguing byproducts of such studies has been the discovery of “*halo nuclei*” such as  ${}^6_3\text{Li}$  (► Fig. 3.32 and the discussion of knockout reactions) in which the nuclear radius is abnormally large, since the highest-lying pair of neutrons occupies an extended orbit (Hanson et al. 1995; Hanson and Tostevin 2003).

The participant zone constitutes a unique nuclear environment, analogous to a rapidly evolving plasma decoupled from the nuclear mean field. This zone is the source of energetic nonequilibrium light particles emitted from the neck region between the two separating spectator nuclei. Isospin effects in the overlap volume may subsequently modify the isotope yields. Because of the large multiplicities of particles that may be emitted from both spectator and participant sources, quantitative understanding of these reactions requires large detector arrays with excellent charge, mass, and spatial resolution (see ► Chap. 48 in Vol. 5).

The fact that the projectile fragments are emitted with velocities near that of the beam also has practical consequences. From the detection point of view, the identification of a fragment’s charge and mass is simplified by the strongly forward-focused kinematics. Projectile fragmentation is also the basis for one of the major radioactive-beam accelerator concepts. By magnetically separating specific fragmentation products, beams of nuclei far from stability can now be provided with intensities high enough to perform nuclear reaction and structure studies. This capability will greatly enhance future efforts to study the effects of neutron–proton asymmetry on the EOS that are predicted to be significant in several nuclear matter theories (Baran et al. 1998; Li 1997). Several accelerator facilities currently exist, or are in the construction/planning stages, for the study of nuclear isospin effects; for example, ATLAS at Argonne National Laboratory, USA (ATLAS 2010), ISAC at TRIUMF, Canada (TRIUMF 2010), CCL at Michigan State University, USA (CCL 2010), SIS at GSI, Germany (GSI 2010), GANIL, France (GANIL 2010), HRIBF at Oak Ridge National Laboratory, USA (HRIBF 2003), JINR in Dubna, Russia (JINR 2003), RARF at RIKEN, Japan (RIKEN 2010), Cyclotron Institute at Texas A&M, USA (TAMU 2010) and the recently approved FRIB facility at Michigan State University, USA (FRIB 2010).

### 3.6.4 Relativistic Heavy-Ion Collisions: Dense Nuclear Matter

In order to investigate the behavior of nuclear matter at still higher temperatures and densities, it is essential to rely on collisions between heavy ions at relativistic energies (Hermann et al. 1999; Reisdorf and Ritter 1997). At bombarding energies near 1 GeV/A and above, nuclear matter can be compressed to densities considerably higher than in normal nuclei, perhaps

approaching the conditions believed to be present when a neutron star is formed in the core of a collapsing supernova. From event-by-event analysis of the collective trajectories and the momenta of particles emitted during these collisions (► Fig. 3.45), vital tests of the nuclear equation of state can be performed. Two relevant terms often employed in relativistic heavy-ion research are rapidity and flow.

*Rapidity* is defined by the expression

$$y = \frac{1}{2} \ln \left( \frac{E + p_z c}{E - p_z c} \right), \quad (3.87)$$

where  $p_z$  is the momentum component parallel to the beam and  $E$  is the total energy (rest mass plus kinetic energy). Rapidity, which is a relativistic representation of the velocity parallel to the beam, provides a variable suitable for discussing the kinematical regions generated in collisions of relativistic heavy ions.

Depending on the axis of orientation, different types of flow can be defined by addition of vectors, such as in ► Fig. 3.45. *Transverse flow* (see  $F$  in ► Fig. 3.46) is a concept used to examine the emission patterns of spectator nucleons that are emitted transverse to the beam direction ( $z$ -axis in ► Fig. 3.45), presumably due to the anomalously large scatterings they undergo when they interact with the compressed region formed in an event. Target and projectile matter can be distinguished on the basis of their respective rapidities. The amount

■ Fig. 3.45

Schematic view of a relativistic Au + Au collision with impact parameter  $b = 6.0$  fm as a function of time (increasing from left to right as indicated in the cells of the top panel). The middle frame represents matter within a density greater than  $0.1 \rho_0$ , where  $\rho_0$  is the ground-state density of nuclear matter. Bottom panel shows this projection in the reaction plane ( $x$ - $z$ ) with respect to the beam direction  $z$ . The top panel shows contours of constant pressure in the transverse plane ( $x$ - $y$ ) (From Danielewicz et al. 2002)

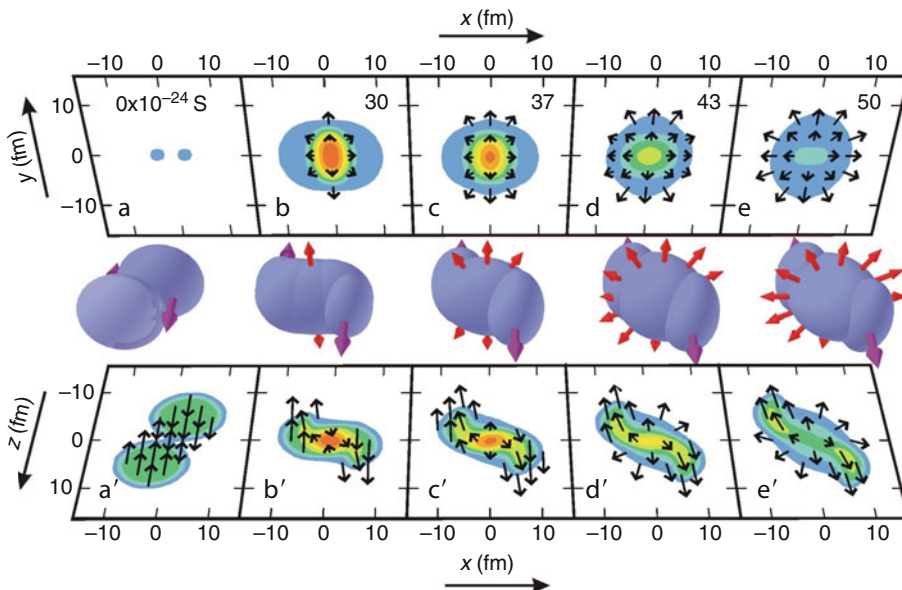
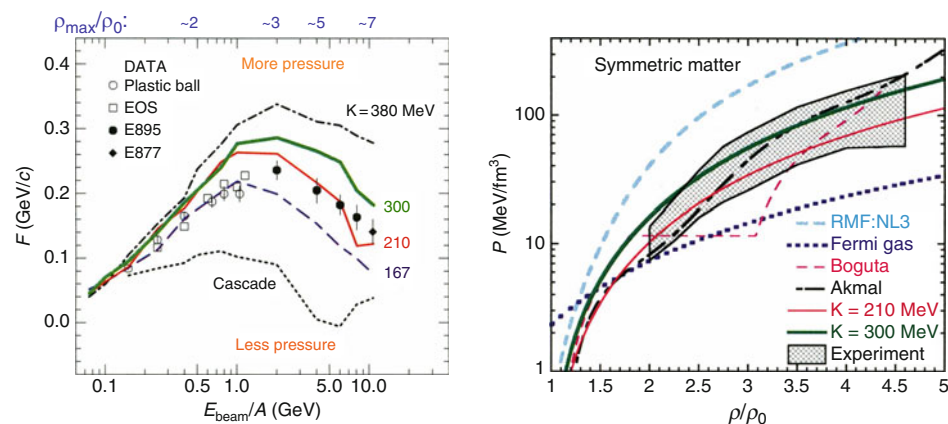




Fig. 3.46

Transverse flow  $F$  as a function of beam energy (left) and zero-temperature EoS for symmetric nuclear matter (right). Note that the larger the incompressibility coefficient, the larger the pressure  $P$  (From Danielewicz et al. 2002)



of flow (Danielewicz et al. 2002) is sensitive to the compressibility of the matter modeled by the transport model. By comparing flow data with the predictions of transport-theory calculations, it is then possible to evaluate the parameters of the EOS at high density (next section).

Flow can be used as a measure of the properties of the N-N interaction in the high density overlap volume, as well as evaluating the densities reached in such collisions. Densities up to  $\rho/\rho_0 \approx 2-4$  (Danielewicz et al. 2002) have been estimated from such studies, providing new insights into the nuclear EOS and the related problem of neutron-star formation in supernovae. In addition, the spectra observed at bombarding energies above  $E/A \approx 10$  GeV/nucleon reach spectral temperatures of up to  $T \approx 150$  MeV. Such temperatures approach the value for deconfinement into a quark-gluon plasma, a plasma of a type not present since the primeval conditions of the Big Bang.

In recent years, the focus of this research has been at the Relativistic Heavy-Ion collider at Brookhaven National Laboratory (RHIC 2005, 2010). One of the most significant findings from the work at RHIC has been that the quark-gluon plasma generated has an ultralow viscosity-to-entropy ratio. The low viscosity implies that the degrees of freedom (quarks and gluons) have short mean-free paths and that the medium itself is still strongly correlated. While this implies that hydrodynamic reaction-model descriptions are valid, fundamental theory is yet to provide a clear insight into why the medium is so strongly coupled. Even higher energy work at the Large Hadron Collider at Conseil Européenne pour la Recherche Nucléaire (LHC, CERN 2010) will produce still higher temperatures and is likely to shed new light on this question.

## 3.7 The Nuclear Equation of State

### 3.7.1 Background and Connection to Classical Thermodynamics

In an introduction to thermodynamics, one studies large systems with the aid of “extensive” energy functions. These energy functions have two “sectors” for one-component systems, one

“mechanical” and the other “thermal.” For multicomponent systems another “chemical” sector must be added. The variables are:  $P$  and  $V$  (or its inverse, the number density  $\rho$ ) for the “mechanical” sector and  $S$  and  $T$  for the “thermal” sector. The natural independent variable for the thermal sector is the entropy  $S$  for the pure energy functions while  $T$  is the independent variable in this sector for the free energies (corresponding to the energy available to do work). For macroscopic systems  $S$  and  $V$  are extensive, while  $T$  and  $P$  are intensive, meaning that one and only one of the variables in each set must be extensive.

Equations of state (EoS) are an attempt to capture the interrelationships between the variable set of thermodynamics for *infinite matter*, in the absence of long-range interactions. Thermodynamics itself is the enterprise of trying to describe matter with the absolute minimum number of macroscopic variables. One deduces the EoS from direct measurement of the macroscopic variables and from measureable derivatives such as the isothermal and adiabatic compressibilities for the “mechanical” sector and the constant pressure or volume heat capacities for the thermal sector.

For finite systems such as nuclei, a surface sector must be added. This sector is not extensive (i.e., while proportional to the surface area, it is not proportional to the amount of material). The study of systems where the energy functions are nonextensive has a long history starting with the work of Gibbs. Both small systems (due to surfaces) and systems with long-range interactions (where the interaction energy scales with the number of participants squared) fall into this category. Nuclei suffer from both of these extensivity-destroying features.

Recalling basic (extensive) thermodynamics, the internal energy  $E$  of an extensive one-component system is

$$dE^* = TdS - PdV \quad \text{or} \quad d\varepsilon = Tds - Pd\varepsilon. \quad (3.88)$$

The lower case is employed in the second version to indicate the energy, entropy, and volume per particle. The pressure is no more than the dependence of energy on volume or number density,

$$P = -\left(\frac{\partial \varepsilon}{\partial v}\right)_s = \rho^2 \left(\frac{\partial \varepsilon}{\partial \rho}\right)_s = \rho^2 \left[ \left(\frac{\partial \varepsilon_0}{\partial \rho}\right)_s \right] + \rho^2 \left\{ \left(\frac{\partial \varepsilon_{\text{asym}}}{\partial \rho}\right)_s \right\}. \quad (3.89)$$

The second equality makes use of the fact that the volume per unit and the number density are inversely related,  $v = \rho^{-1} \rightarrow dv = -\rho^{-2}d\rho$ . The final equality separates the isoscalar component of the pressure (the only term present for symmetric matter) from that originating from neutron/proton asymmetry. At large asymmetries, the second term dwarfs the first, so it is this term that is principally responsible for resisting the gravitational collapse of a neutron star.

The compressibility is defined as either the negative of the relative change in the volume with the application of pressure or the relative change in the density with the application of pressure under specified conditions. (The signs are such as to make the coefficient positive for any thermodynamically stable system.) Therefore, the adiabatic compressibility (the version which dictates the speed of sound) is

$$\kappa_s = -\frac{1}{v} \left(\frac{\partial v}{\partial P}\right)_s = \frac{1}{\rho} \left(\frac{\partial \rho}{\partial P}\right)_s. \quad (3.90)$$

Rather than dealing with  $\kappa$ , nuclear science has focused in its inverse, the “*incompressibility*” coefficient”  $K$ . Another minor change is that rather than dealing with a problem that is intrinsically 3-dimensional, the analysis is reduced to a one-dimensional problem of the stiffness with respect to harmonic vibrations of a uniform (albeit infinite) sphere of radius  $R$ .

(The conversion to a 1-D problem, with the independent variable being  $R$ , makes use of  $d\rho/dR = -3\rho/R$  twice, yielding the factor of 9). In this case, from [Eq. \(3.89\)](#) one obtains the nuclear matter (nm) incompressibility  $K_{\text{nm}}$  (with the dimensions of energy):

$$K_{\text{nm}} [\text{MeV}] \equiv 9 \left( \frac{\partial P}{\partial \rho} \right)_s = 9 \rho_{\text{sat}}^2 \left( \frac{\partial^2 \varepsilon}{\partial^2 \rho} \right)_{s, \rho = \rho_{\text{sat}}}. \quad (3.91)$$

This is just the inverse of  $\kappa_s$ , with a slightly different coefficient. (Note that  $1/\rho$  for saturated nuclear matter is  $V/A = (4/3)\pi R^3/A = (4/3)r_0^3\pi \approx 7.2 \text{ fm}^3/\text{nucleon}$ ).

The thermal properties of matter are captured by its ability to absorb energy. The quantum version of the relevant question is: at a given excitation energy, how many ways can a system sustain that energy? At constant volume, the energy-dependent answer to this question is captured in the heat capacity as a function of excitation energy

$$C_V(E^*) \equiv \left( \frac{\partial E^*}{\partial T} \right)_V = T \left( \frac{\partial S}{\partial T} \right)_V = k_B T \left( \frac{\partial \ln \omega(E^*)}{\partial T} \right)_V. \quad (3.92)$$

The effective mass, introduced in [Sect. 3.3](#) and discussed more in [Sect. 3.5](#), is the factor that corrects a single-particle logic for the many-body correlations. Thus, one can say that the study of the evolution in the level-density parameter  $a$ , is one of determination of how  $m^*$  changes with  $E^*$ . This thermal sector was discussed in [Sect. 3.5](#).

Description of the properties of matter is punctuated by phase transitions. While formally such transitions can occur only in the (extensive) matter limit, the manifestations of a matter phase transition in a finite system can profoundly affect the behavior of a finite “clump” of matter. In nuclear science, symmetric matter must undergo a liquid-to-gas-like transition as the matter is heated and the average density reduced, since it has an attractive interaction that can be saturated at short-range. Just as in the case of standard fluids, there will be a coexistence region that self-partitions into low- and high-density phases. Just how this transition is manifest in real charged and finite nuclear (i.e., in the real nonextensive) systems has been the focus of considerable effort.

### 3.7.2 The Perspective from Energy-Density-Functional Theory

Extraction of an EoS from a fundamental theory is of course desirable, and while there has been progress along this line, presently one must work with functionals of relevant properties such as the density and asymmetry that depend on free parameters that must be determined by some fitting procedure (Bender et al. 2003).

The task is to generate a functional for the energy of a finite system as a function of density and other variables that might be relevant. In fact, this procedure just generates a more rigorous alternative to the Liquid-Drop Model (LDM). This version of developing an expression for the mass of a drop involves an integral over space. The surface term comes from the gradients (inspired by van der Waals) and the asymmetry terms by the dependence on both of the individual densities. The Coulomb term, not included in the expression provided in the text, comes from an integral over the nuclear volume, the same way as it does in the LDM.

Let the energy as a function of density  $E(\rho)$  be this function, which in the nuclear case must be a function of the local neutron and proton densities and their derivatives. (Van der Waals appreciated that nature must “pay” for producing nonuniform densities.) The binding energy

for a drop must come from an integral of the nuclear energy density  $\xi$ , with corrections for density gradients over the nuclear density,

$$E = \int \left\{ \xi(\rho_n, \rho_p) + \eta(\nabla\rho)^2 + \eta_{\text{asym}}(\nabla\rho_n - \nabla\rho_p)^2 + \dots \right\} d^3r + E_{\text{Coul}}, \quad (3.93)$$

where, in this case, the  $\eta$ 's (one isoscalar and one for the asymmetry) are coefficients to be determined by fitting data in exactly the same fashion as the surface and asymmetry coefficients are fit in the liquid-drop model.

This approach works well for classical fluids, although its convergence has never been proved. The connection to infinite uncharged nuclear matter is that the gradient expansion vanishes and the Coulomb term (which blows up in the infinite limit) is dropped. In that case, the nuclear energy density  $\xi$  or the energy per nucleon  $\varepsilon$  (see [Eq. \(3.94\)](#)) can be viewed as an isoscalar part (with only a density dependence) and an asymmetry component with both a density and an asymmetry dependence as a function of the deviation of the density from saturation and of the asymmetry from symmetry,

$$\xi \equiv \frac{E}{V} = \rho \left\{ \frac{E}{A} \right\} = \rho \varepsilon, \quad (3.94)$$

where

$$\begin{aligned} \varepsilon(\alpha, \delta) &\approx [\varepsilon_0(\alpha)] + \{\varepsilon_{\text{asym}}(\alpha, \delta)\} \approx [\varepsilon_0(\alpha)] + \{S(\alpha)\delta^2\}, \\ \alpha &\equiv \frac{\rho_n + \rho_p}{\rho_0}, \quad \delta \equiv \frac{\rho_n - \rho_p}{\rho_n + \rho_p}. \end{aligned} \quad (3.95)$$

The term in square brackets is the energy (per nucleon) of symmetric nuclear matter, while the term in curly brackets captures the change in the energy with asymmetry. Note that the coefficient of the asymmetry term is density-dependent.

Development of the first and second terms (isoscalar and isovector, respectively) in [Eq. 3.94](#) leads to several other coefficients that in principle can be phenomenologically determined. As symmetric matter represents an equilibrium point, an expansion in the density (from the saturation value) cannot have a linear term. The same cannot be said of the asymmetry term. Therefore, an expansion for both the isoscalar and asymmetry terms can be written,

$$\varepsilon(\alpha, \delta) = \left[ \varepsilon_0 + \frac{K}{18}(\alpha - \alpha_0)^2 + \dots \right] + \left\{ \left( S_0 + \frac{L}{3}(\alpha - \alpha_0) + \frac{K_{\text{asym}}}{18}(\alpha - \alpha_0)^2 \dots \right) \delta^2 \right\} + \dots, \quad (3.96)$$

where the term in curly parenthesis is the asymmetry contribution is the  $S(\alpha)$  in [Eq. 3.94](#). The constants in the coefficients are chosen so that the constants ( $K$ ,  $L$ , and  $K_{\text{asym}}$ ) are consistent with other formulations (Danielewicz and Lee 2009).

### 3.7.3 The Incompressibility from the Physical LDM-Like Expansion

The incompressibility can also be expressed in a Liquid-Drop Model-like expansion, that is, an expansion where the terms are associated with *physical corrections*, rather than the result of

a Taylor expansion. Doing so provides an expression for the incompressibility of a *finite* charged drop (Youngblood et al. 1999),

$$K_A = K_{\text{nm}} + K_{\text{surf}} A^{-1/3} + K_{\text{asym}} \left( \frac{N-Z}{A} \right)^2 + K_{\text{coul}} \frac{Z^2}{A^{4/3}}. \quad (3.97)$$

The first term  $K_{\text{nm}}$  is the incompressibility of infinite uncharged nuclear matter (the extensive quantity), the second corrects the matter incompressibility for the presence of the surface, the third term corrects for the neutron–proton asymmetry of the matter and the fourth term (one that blows up for infinite matter) corrects for the charge on the finite drop.

The left-hand side of the physical expansion can be determined from the (mean) energy of the giant-monopole resonance (GMR), and root-mean-square size of the nuclear drop (Colò et al. 2004),

$$E_{\text{GMR}} = \hbar \sqrt{\frac{K_A}{m \langle r^2 \rangle}}. \quad (3.98)$$

Fitting the physical expansion leads to a value of  $K_{\text{nm}} = (240 \pm 10)$  MeV (Colò et al. 2004).

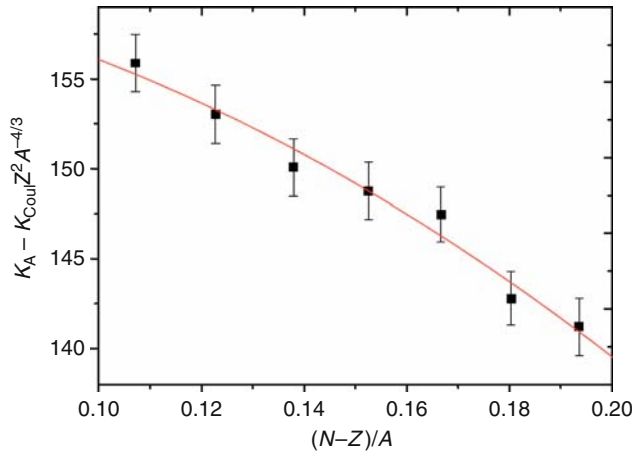
Unfortunately, the GMR data address only tiny variations of the mean density about saturation. The extrapolation to densities far different than saturation is questionable. To gain insight into density variations of more relevance to neutron-star structure, HI “flow” analyses of the type shown in Fig. 3.45 have been used. The momenta transverse to the beam (as a function of the beam energy) are shown in Fig. 3.46 along with a comparison to model (BUU) simulations. The more incompressible the fluid, the greater the momentum “extruded” perpendicular to the beam axis. The constraints on the symmetric matter incompressibility are summarized on the right-hand side of the same figure (Danielewicz et al. 2002). Two statements can be made about the flow results. First, these data are inconsistent with the strongly repulsive nuclear equations of state derived from relativistic mean field theories and weakly repulsive equations of state, which would result from a phase transition at densities less than three times the saturation density. Second, while the uncertainties grow with density, the flow results are consistent with those from the GMR studies.

It is the asymmetry term that has been the focus of much recent effort, as it is this term that provides the internal pressure, holding back the gravitational collapse of a (cold) neutron star. First, results are presented from the perspective of the physical (LDM-like) expansion. As  $K_{\text{surf}}$  is close in magnitude (but opposite in sign) to  $K_{\text{nm}}$ , and the Coulomb constant ( $-5.2$  MeV) is essentially model-independent, for sufficiently heavy isotopes, the difference  $K_A - K_{\text{coul}} Z^2 A^{-4/3}$  from Eq. 3.97 can be approximated by the analytic form  $y = K_{\text{asym}} \delta^2 + b$ , where  $\delta = (N - Z)/A$ . This approximate relationship has been employed for a series of even- $A$  Sn isotopes for which the giant monopole resonance (GMR) was excited with inelastic alpha-particle scattering at small angles (Li et al. 2007). This work (Fig. 3.47) provided a value  $K_{\text{asym}} = (-550 \pm 100)$  MeV. Data on the GMR from isotopes with asymmetries greater or less than those of the natural Sn isotopes would greatly reduce the uncertainty on  $K_{\text{asym}}$ . This will be one of the focus activities at FRIB in the coming decade. Nevertheless, this result is consistent with the value  $K_{\text{asym}} = (-500 \pm 50)$  MeV obtained from analysis of the isotopic transport ratios in medium-energy heavy-ion reactions (Li et al. 2008).

Viewed from the energy-density expansion perspective, the analysis described above will scramble the constant ( $S_0$ ), linear ( $L$ ), and quadratic ( $K_{\text{asym}}$ ) terms in Eq. 3.96. Separating the dependences is an active research area, about which several comments can be made.

■ Fig. 3.47

Systematics of the difference  $K_A - K_{\text{Coul}} Z^2/A^{4/3}$  in the Sn isotopes as a function of  $\delta = (N-Z)/A$ ;  $K_{\text{Coul}} = -5.2$  MeV. The solid line represents least-squares quadratic fit to the data (When plotted in this fashion, the value of  $K_{\text{asym}}$  comes from the curvature of the best fit) (From Li et al. 2007)



First, there is a cross-correlation (shown in Fig. 3.48) between the constant term ( $S_0$ ) and the linear term ( $L$ ) (Tsang et al. 2009). Second, an overall constraint on the density dependence of the asymmetry energy is deduced from HI-reaction data (Danielewicz and Lee 2009; Shetty et al. 2007),

$$S(\rho) \propto \rho^x (1 + c\rho); \quad \frac{2}{3} \leq x \leq 1. \quad (3.99)$$

Again, in an effort to be forward looking, experiments on parity-violating electron scattering on  $^{208}\text{Pb}$  (a project called PREX) will be done in the next few years. If successful, this experiment will produce data directly sensitive to the linear term in the dependence of the asymmetry energy on density (Horowitz and Piekarewicz 2002).

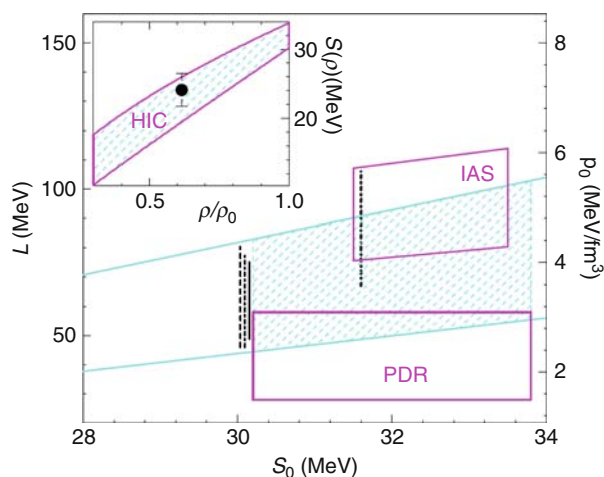
### 3.7.4 Cluster Formation at Very Low Density

At very low density and temperature, alpha clusters become a significant component of symmetric nuclear matter (Friedman and Pandharipande 1981). The contribution of such clusters is determined by an interplay between the translational phase space (which favors free nucleons with increasing temperature) and binding energy (which favors alpha-particle formation by allowing more energy to be available for translation). One only needs to consider alpha decay of heavy nuclei to appreciate that clustering in the matter tails of heavy (cold) nuclei is significant. As is the case in water, one can consider such clusters as transitory, an existence that increases as the density and temperature decrease.

There have been significant advances on both the theoretical and experimental fronts in elucidating the behavior of nuclear material at very low densities, densities less than 0.1 of saturation. On the theoretical front, a virial (density expansion) EoS has been formulated by

■ Fig. 3.48

Representation of the constraints on parameters  $S_0$  and  $L$  in Eq. 3.96. The right axis corresponds to the neutron-matter-symmetry pressure at saturation density. The region bounded by the *diagonal lines* represents the constraints obtained from analysis of HI collisions. The vertical lines near  $S_0 = 31$  MeV are obtained from LDM-like analyses (i.e., masses). The lower and upper boxes are formed by the constraints from the so-called Pigmy Dipole resonances (neutron-rich skin vs. core) and from symmetry-energy analysis on nuclei, respectively. The inset shows the density dependence of the symmetry energy in the shaded region. The symbol in the inset represents the GDR. Note the greatly offset scales on the abscissa and ordinate (From Tsang et al. 2009)



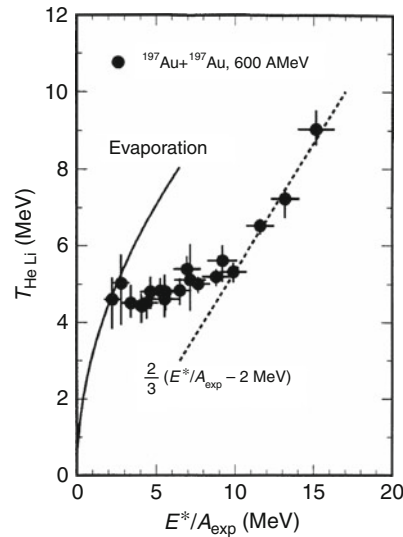
explicitly considering the (N-N), N-alpha and alpha-alpha scattering phase shifts (Horowitz and Schwenk 2006). One of the values of this work has been to quantify the pressure reduction and asymmetry energy enhancement (relative to a nucleon gas), due to alpha-particle clustering. Confirmation of this enhancement at densities of 0.01–0.05 times the ground-state density of symmetric nuclear matter has been observed in an analysis of HI reaction data (Kowalski et al. 2007, Natowitz et al. 2010). This limiting behavior is one aspect of clustering in nuclear systems. The next section deals with perhaps the most significant aspect of this behavior.

### 3.7.5 Multifragmentation: The Low-Density Regime and the Manifestation of the Liquid–Gas Phase Transition in Nuclear Collisions

When the first high-energy accelerators became available in the 1950s, radiochemical and emulsion studies indicated the existence of a reaction mechanism in which a heavy nucleus is disintegrated into multiple neutrons, H and He ions, and IMFs (Fig. 3.1), a process now called multifragmentation (Lynch 1987; Trautmann 2001; Chomaz 2001). The connection of this phenomenon to the nuclear liquid–gas phase transition in matter was made after construction of a “caloric curve,” i.e.,  $T(E^*)$ , shown in Fig. 3.49 (Pochodzalla et al. 1995). The ordinate was constructed using isotope ratio “thermometers.” Such thermometers use the

■ Fig. 3.49

**Caloric curve** (temperature vs. heat) derived from peripheral collisions in  $^{197}\text{Au} + ^{197}\text{Au}$  reactions. Temperatures are derived from yield ratios of  $^3\text{He}/^4\text{He}$  and  $^6\text{Li}/^7\text{Li}$  isotopes and heat ( $E^*/A$ ) from event-by-event calorimetry. The *solid line* describes the expected behavior for nuclear evaporation. The dashed line is that expected for a hot nuclear gas. The plateau region in between has been interpreted as evidence for a “boiling-like” phase transition in nuclei (Pochodzalla et al. 1995)



difference in the ground-state masses of different isotopes in a Boltzmann expression for the relative yield of the isotopes (Albergo 1985). The experimental isotope ratios are fit by adjusting the temperature.

The only way to have a halt in the increase in  $T$  with increasing  $E^*$  is for additional degrees of freedom to become available. In the case of the macroscopic liquid–gas transition, it is the access to the full 3-D translational degrees of freedom that halts the increase in the average energy in any one degree of freedom (as energy is poured into the newly accessed ones.)

The observables in high-energy light-ion or intermediate-energy HI collisions all relate to the above-mentioned multifragmentation exit channel. In order to create multifragmentation events, it is necessary to deposit excitation energies in a nucleus in excess of  $E^*/A \approx 4\text{--}5$  MeV, i.e., about 1 GeV in a heavy nucleus. Transport codes predict that such events are rare, comprising less than  $\sim 5\%$  of the nuclear reaction cross section. Among the methods used to prepare such systems have been light-ion reactions (ISiS, FASA), reverse-kinematics reactions (EOS), peripheral reactions (ALADIN), and near-symmetric heavy-ion ( $A + A$ ) reactions (INDRA, ALADIN and Miniball). The various detector systems (given in square brackets) and earlier devices are referred to in Durand et al. (2001).

The plateau in the caloric curve is only indicative of access to additional degrees of freedom, not necessarily access to prompt multifragment decay. For example, expansion or greatly increasing the surface diffuseness, or an increase in the level-density parameter all would decrease the rate of increase of  $T$  with  $E^*$ , as discussed in Sect. 3.5. However, numerous

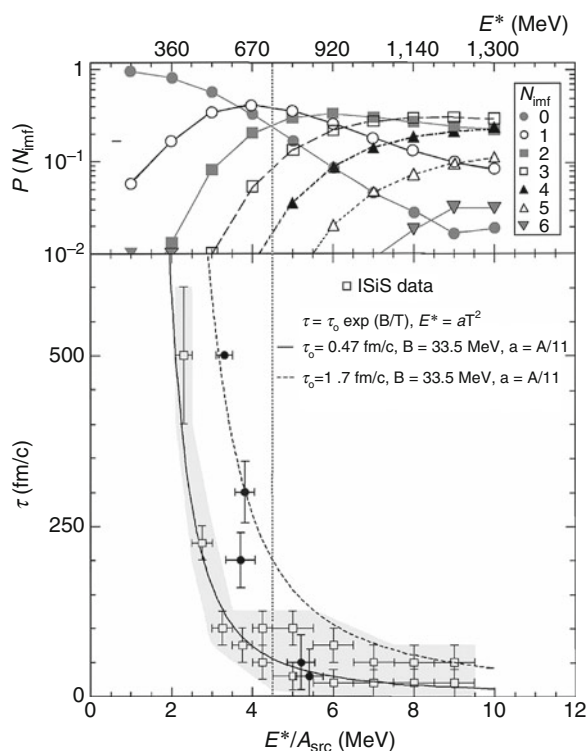


observables do in fact indicate that multifragmentation is the result of a near-instantaneous phenomenon rather than the result of sequential binary decays. Among these observables are evidence for a breakup density of only 20–30% of normal nuclear density ( $\rho/\rho_0 \approx 0.2$ – $0.3$ ), compression–decompression effects in  $A + A$  reactions, and most important, time-scale measurements based on spatial correlations among the clusters. The latter work demonstrates that the breakup time scale is nearly simultaneous ( $\tau \approx 10^{-22}$  s), much shorter than expected for a drawn-out sequential evaporative sequence (see [Fig. 3.50](#) and Viola et al. 2006).

Nuclear models based upon both statistical concepts and those for a generalized liquid–gas phase transition dependent on fragment size distribution are in general accord with the phase transition interpretation as long as the models assume expansion to a given breakup volume. In these models, the decay can be that expected from a statistical sampling of the cluster phase space (Bondorf et al. 1985; Gross 1990; Das et al. 2005), that is, without any dynamics, or a time-dependent approach in which emission occurs as the system expands to the breakup volume (Friedman 1990). However, it must be mentioned that as recent fragment–fragment correlation data could not be reproduced by prompt fragmentation models, Gentil et al. (2008), the interpretation of these complex decays is still not fully understood.

**Fig. 3.50**

**Top:** Evolution of a multifragmentation reaction as a function of heat  $E^*/A$  for the number of  $Z \geq 3$  fragments (probability  $P(N_{\text{mf}})$ , IMF multiplicity  $N_{\text{mf}}$ ). **Bottom:** Breakup time  $\tau$  in fm/c (1 fm/c  $\approx 3.3 \times 10^{-24}$  s). The growing multiplicity and rapid decrease in the breakup time are consistent with a “boiling-like” phase transition in nuclei (Beaulieu et al. 2000)



Analyses based on the finite-scaling model proposed by Fisher for classical drops (Elliott et al. 2002), percolation theory (Bauer et al. 1992), and a statistical multifragmentation model (Botvina et al. 1999) show generally good agreement with the concept that the transition (halt in the increase in the  $T$  with  $E^*$ ) is associated with accessing the multifragment phase space. The opening of this most complex decay channel in finite nuclei at  $T \approx 4\text{--}6$  MeV implies that infinite, uncharged matter cannot exist above  $T_{\text{crit}} \approx 17$  MeV (Natowitz et al. 2002).

Perhaps, the most insightful result employing the fragmentation data comes from employing Fisher's model (Elliott et al. 2002). The critical exponents associated with the transition that occurs in the finite system's analog to the infinite matter liquid–gas phase transition are extracted. In addition, using the ubiquitous coexistence behavior for classical fluids, the nuclear phase transition data were added to what are known as “Guggenheim plots” ( $T/T_{\text{crit}}$  vs. both the low and high reduced densities  $\rho_v/\rho_{\text{crit}}$  and  $\rho_l/\rho_{\text{crit}}$ ). However, it should be kept in mind that unlike the macroscopic cases employed by Guggenheim and others to prove reducibility, actual measurements of the two coexisting densities as a function of temperature is not done. Nevertheless, this work shows how nature's systems, while seeming quite different, are often interrelated. The careful reader would have noted a few such cases of this unity of natural systems in this chapter.

### 3.8 Addendum: Cross-Section Calculations

For the case of a beam of charged particles incident on a thin target of thickness  $x$ , as illustrated in [Fig. 3.51](#), the projectile flux can be expressed as  $n_p = I/(qe)$ . Here  $I$  is the electric current in amperes, as measured in a Faraday cup that collects the total charge deposited by projectiles of charge  $qe$ . For light ions, the projectile ion is usually fully stripped of its atomic electrons so that  $q = Z$ , the atomic number of the ion. However, for very low energy or very heavy ions, complete stripping of the atomic electrons may not occur, so that the ionic state of the projectile must be accounted for. The number density of target atoms  $n_t$  is given by

$$n_t = (\rho_M/M)N_A, \quad (3.100)$$

where  $\rho_M$  is the mass density,  $M$  is the molar mass of the target atoms, and  $N_A$  is Avogadro's number ( $6.022 \times 10^{23} \text{ mol}^{-1}$ ). For reactions induced by a beam of particles (two dimensional geometry), the surface number density of target nuclei ( $N_t/\text{area}$ ) is the relevant target collision factor, assuming that the beam cross section is smaller than the target area. For a given thickness  $x$  the surface number density (usually measured in  $\text{cm}^{-2}$ ) is

$$N_t/S = n_t x. \quad (3.101)$$

where  $S$  is the surface area of the target.

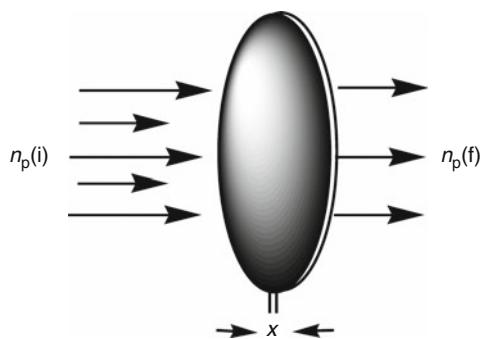
With these definitions the production rate  $R(a,k)$  for a given exit channel  $k$  becomes

$$R(a,k) = n_p n_t x \sigma(a,k). \quad (3.102)$$

where the quantities are most commonly given in the following units:  $R$  ( $\text{s}^{-1}$ ),  $n_p$  ( $\text{s}^{-1}$ ),  $n_t$  ( $\text{cm}^{-3}$ ),  $x$  (cm), and  $\sigma$  ( $\text{cm}^2$ ). For thick targets the above linear behavior does not hold anymore. However, an arbitrarily thick sample can be viewed as being composed of thin slices of thickness  $dx$ . The rate of product nucleus formation is then given by the rate of particle removal from the beam as it passes through the slice of the target of thickness  $dx$ ,

Fig. 3.51

Beam of projectile nuclei impinging on a circular disk of thickness  $x$



$$-dn_p = n_p n_t \sigma(a, k) dx. \quad (3.103)$$

Here  $\sigma(a, k)$  stands for the total cross section. Integration over the thickness  $x$  of the target gives

$$-\int_i^f \frac{dn_p}{n_p} = \sigma n_t \int_0^x dx, \quad (3.104)$$

where  $i$  (initial) and  $f$  (final) are to indicate the particle flux entering and leaving the target, respectively, and

$$\frac{n_p(f)}{n_p(i)} = \exp(-n_t \sigma x). \quad (3.105)$$

The production rate then becomes

$$R = n_p(i) - n_p(f) = n_p(i)[1 - \exp(-n_t \sigma x)]. \quad (3.106)$$

If  $\sigma$  is the total reaction cross section, this expression predicts the attenuation of the beam due to all nuclear reactions in a target of thickness  $x$ . This expression assumes that the beam intensity and cross section are constants. In reality, this is not necessarily the case and corrections may be required due to time variations in the projectile current and dependence of the cross section on beam energy (Fig. 3.51).

For an infinitely thin target, that is, one in which there is no appreciable attenuation of the beam due to target thickness, the above expression can be simplified by expanding the exponential term,  $\exp(-n_t \sigma x) \approx 1 - n_t \sigma x$ . This leads to a commonly-used expression for the rate

$$R(a, b) = \frac{I_0}{z_p e} \sigma(a, b) \frac{N_t}{S}, \quad (3.107)$$

where  $S$  is the area of the target containing  $N_t$  atoms of weight  $w$  and  $N_t = (w/M)N_A$ . The surface number density (measured, for example, in atoms  $\text{cm}^{-2}$ ) – or its alternative, the surface density (given, for instance, in  $\text{g cm}^{-2}$ ), to which it is proportional – is ordinarily a more accurate and easily determined quantity for thin targets than is the actual thickness. The basic assumption here is that the beam diameter is smaller than that of the target.

In the geometry of a nuclear reactor, the target can be considered to be immersed in a neutron gas, so that all target atoms  $N_t$  are exposed to the flux of neutrons. In such cases, target thickness usually does not matter and one can write

$$R = \sigma(a, b)N_t\phi, \quad (3.108)$$

where  $\phi$  is the *neutron flux* (which is usually given in neutrons  $\text{cm}^{-2} \text{s}^{-1}$ ), a parameter of the reactor and the position of the irradiation within it. The same is true for reactions in stars, except that this expression must be modified for the flux of both reactants.

Finally, in the production of radionuclides, it is necessary to include the effects of radioactive decay during bombardment in the rate equation as discussed in ► Chap. 7 of this volume. The net production rate ( $dN/dt$ ) will be the difference between the production ( $R$ ) and decay ( $\lambda N$ ) rates

$$dN/dt = R - \lambda N. \quad (3.109)$$

The solution to this differential equation gives the number of atoms  $N$  produced as a function of time,

$$N = (1/\lambda)R(1 - e^{-\lambda t}), \quad (3.110)$$

where  $\lambda$  is the decay constant of a given radioactive product nucleus and  $t$  is the bombardment time. The factor  $(1 - e^{-\lambda t})$  is called the *saturation factor*. This factor is an important consideration in production of short-lived medical radionuclides for diagnosis and therapy, and for efficient use of accelerator or reactor time. For bombardment times greater than one half-life, this factor illustrates the *law of diminishing returns*; i.e., half the maximum activity is formed after one half-life, 3/4 after two half-lives, etc.

### 3.9 Selected Nuclear Reaction Web Resources

Argonne Tandem Linac Accelerator System (ATLAS), <http://www.phy.anl.gov/atlas>  
 Australian National University Tandem, Canberra, <http://www.rsphysse.anu.edu.au/nuclear>  
 Bhabha Atomic Research Center, <http://www.dae.gov.in/res.htm>  
 Canada's National Laboratory for Particle and Nuclear Physics (TRIUMF), <http://www.triumf.ca>  
 Centre Européenne pour la Recherche Nucléaire (CERN), <http://public.web.cern.ch>  
 China Institute of Atomic Energy, Beijing, <http://www.nti.org/db/china/ciae.htm>  
 Chinese Academy of Sciences, Lanzhou, <http://english.imp.cas.cn/>  
 Coupled Cyclotron Laboratory, Michigan State University, <http://www.nsl.msui.edu>  
 Cyclotron Research Center at Louvain, <http://www.cyc.ucl.ac.be>  
 Facility for Rare Isotope Beams (FRIB), <http://www.frib.msu.edu/>  
 Fermi National Accelerator Laboratory (FNAL), <http://www.fnal.gov>  
 Gesellschaft für Schwerionenforschung (GSI), <http://www.gsi.de>  
 Grand Accélérateur des Ions Lourds (GANIL), <http://www.ganil.fr/>  
 Holifield Radioactive Ion Beam Facility (HRIBF), <http://www.phy.ornl.gov/hribf/hribf.html>  
 Institute for Nuclear Physics, Jülich (COSY), <http://www.fz-juelich.de>  
 Joint Institute for Nuclear Research (JINR), <http://www.jinr.dubna.su>  
 Kernphysisch Versneller Instituut (KVI), Groningen, <http://www.kvi.nl>  
 Laboratory National Legnaro (LNL), <http://www.lnl.infn.it>  
 Laboratory of Nuclear Science, Catania, <http://www.ct.infn.it>  
 Lawrence Berkeley Laboratory, <http://www.lbl.gov>

Lawrence Livermore National Laboratory, <http://www.llnl.gov>  
Los Alamos National Laboratory, <http://www.lanl.gov>  
Los Alamos Print Archives (LANL), <http://lib-www.lanl.gov/>  
National Nuclear Data Center, NNDC (BNL), <http://www.nndc.bnl.gov/>  
Pacific Northwest National Laboratory, <http://www.pnl.gov>  
Relativistic Heavy-Ion Collider (RHIC), <http://www.bnl.gov/RHIC>  
Research Reactors Database, <http://www.iaea.or.at/worldatom/rrdb/>  
RIKEN Accelerator Research Facility (RIKEN), <http://www.rarf.riken.go.jp>  
The Svedberg Laboratory (TSL), <http://www.tsl.uu.se>  
The Texas A&M Cyclotron Institute, <http://cyclotron.tamu.edu>

## References

- Aerts G et al. (2006) Phys Rev C73 : 054610  
Albergo S et al (1985) Nuovo Cimento Soc Ital Fis A 89A:1  
ATLAS (2010) <http://www.phy.anl.gov/atlas>  
Austern N (1970) Direct reaction theories. Wiley, New York  
Axilrod BM, Teller E (1943) J Chem Phys 11:299  
Baker SD, McIntyre JA (1967) Phys Rev 161:1202  
Baldwin SP, Lott B et al (1995) Phys Rev Lett 74:1299  
Baran V, Colonna M, Ditoro M, Larimov AB (1998) Nucl Phys A 632:716  
Bass R (1974) Nucl Phys A 231:45  
Bauer W, Gelbke CK, Pratt S (1992) Annu Rev Nucl Sci 42:77  
Beaulieu L et al (2000) Phys Rev Lett 84:5971  
Bender M, Heenen P-H, Reinhard P-G (2003) Rev Mod Phys 75:121  
Benenson W, Harris JW, Stocker H, Lutz H (eds) (2002) Handbook of physics. Springer, New York  
Bertsch GF, Kruse H, Dasgupta S (1984) Phys Rev C 29:673  
Bertulani CA (2009) Wiley Encyclopedia of Physics Wiley-VCH, Berlin  
Blann HM et al (1975) Annu Rev Nucl Sci 25:123  
Bohr A, Mottelson BR (1969) Nuclear structure, vols 1 and 2. W.A. Benjamin, New York  
Bohr N, Wheeler JA (1939) Phys Rev 56:426  
Bonche P, Koonin S, Negele WG (1976) Phys Rev C 13:1010  
Bond P, Johansen PJ, Koonin SE, Garpman S (1977) Phys Lett 71B:43  
Bondorf J et al (1985) Nucl Phys A 443:221  
Botvina A et al (1999) Phys Rev C 59:3444  
Bowles TJ, Gavron VN (1993) Annu Rev Nucl Part Sci 43:117  
Breit G, Wigner EP (1936) Phys Res 49:519  
Brogia RA et al (1983) Phys Lett 133B:34  
Buck B, Maddison RN, Hodgson PE (1960) Phil Mag 5:1181  
Campi X, Krivine H, Plagnol E, Sator N (2005) Phys Rev C 17:041601  
CCL (2010) <http://www.nsl.msu.edu>  
CERN (2010) <http://public.web.cern.ch>  
Cerny J (ed) (1974) Nuclear reactions and spectroscopy. Academic, New York/London  
Chadwick MB, Oblozinsky P (1992) Phys Rev C 46:2028  
Charity RJ et al (2001) Phys Rev C 63:024611  
Charity RJ, Sobotka LG, Dickhoff WH (2006) Phys Rev Lett 97:162503  
Charity RJ, Mueller JM, Sobotka LG, Dickhoff WH (2007) Phys Rev C 76:044314  
Chomaz P (2001) International nuclear physics conference, <http://proceedings.aip.org/proceedings>  
Chomaz P, Colonna M, Guarnera A, Randrup J (1994) Phys Lett B 254:340  
Colò G et al (2004) Phys Rev C 70:024307  
Cottingham WA, Greenwood DA (2001) An introduction to nuclear physics. Cambridge University Press, New York  
Danielewicz P, Lee J (2009) Nucl Phys A 818:36  
Danielewicz P, Lacey R, Lynch WG (2002) Science 298:1592  
Das CB, Das Gupta S, Lynch WG, Mekjian AZ, Tsang MB (2005) Phys Rev 406:1  
Dasgupta S, Hinde DJ, Rowley N, Stefanini AM (1998) Annu Rev Nucl Part Sci 48:401  
Dasso CH, Landowne S (1987) Comp Phys Comm 46:187  
Durand D, Suraud E, Tamain B (2001) Nuclear dynamics in the nucleonic regime. Institute of Physics Publishing, Bristol  
Elliott JB, Moretto LG, Phair L et al (2002) Phys Rev Lett 88:042701  
Ericson T et al (1963) Ann Phys 23:390  
Fatyg M et al (1985) Phys Rev Lett 55:1376  
Feldmeier H, Schnack J (2000) Rev Mod Phys 72:655  
Feldmeier H, Bieler K, Schnack J (1995) Nucl Phys 586:493

- Feshbach H, Kerman A, Koonin S (1980) *Ann Phys* (N.Y.) 125:429; (1993) *Phys Rev C* 47:2255
- Frahn WE (1978) *Nucl Phys A* 302:267
- FRIB (2010) <http://www.nsl.msu.edu>
- Friedman WA (1990) *Phys Rev C* 42:667
- Friedman B, Pandharipande VR (1981) *Nucl Phys A* 361:502
- Gade A, Glasmacher T (2008) *Prog Part Nucl Phys* 60:161
- Gade A et al (2004) *Phys Rev Lett* 93:042501
- Gadioli E, Hodgson PE (1992) *Pre-equilibrium nuclear reactions*. Oxford University Press, New York
- GANIL (2010) <http://www.ganil.fr>
- Gentil E, Le et al (2008) *Phys Rev Lett* 100:022701
- Glasmacher T (1998) *Annu Rev Nucl Part Sci* 48:1
- Glauber RJ, Osland P (1979) *Phys Lett B* 80:401
- Gregoire C et al (1985) *Nucl Phys A* 436:365
- Griffin JJ et al (1966) *Phys Rev Lett* 17:478
- Gross DHE (1990) *Rep Prog Phys* 53:605
- GSI (2010) <http://www.gsi.de>
- Hanson PG, Tostevin JA (2003) *Annu Rev Nucl Part Sci* 53:219
- Hanson PG, Jensen AS, Jonson B (1995) *Annu Rev Nucl Part Sci* 45:591
- Hauser W, Feshbach H (1952) *Phys Rev* 87:366
- Hermann N, Wessels JP, Wienold T (1999) *Annu Rev Nucl Part Phys* 49:581
- Hiebert JC, Garvey GT (1964) *Phys Rev* 135:B346
- Hodgson PE (1967) *Annu Rev Nucl Sci* 17:1
- Horowitz CJ, Piekarewicz J (2002) *Phys Rev C* 66:055803
- Horowitz CJ, Schwenk A (2006) *Nucl Phys A* 776:55
- HRIBF (2003) <http://www.phy.ornl.gov/hrifb/hrifb.html>
- Huizenga JR, Moretto LG (1972) *Annu Rev Nucl Sci* 22:427
- IAEA (2010) <http://www.iaea.or.at/worldatom/rddb/>
- Ignatyuk AV et al (1975) *Yad Fiz* 21:1185; *Sov J Nucl Phys* 21:612
- Janssens RVE, Khoo TL (1991) *Annu Rev Nucl Sci* 41:321
- JINR (2003) <http://www.jinr.ru/>
- Kittel C (1986) *Elementary statistical physics*. Dover, Mineola, QC174.8K56
- Kowalski S, Natowitz JB, Shlomo S et al (2007) *Phys Rev C* 75:014601
- Kramers HA (1940) *Physica* (Amsterdam) 7:284
- Krane KS (1988) *Introductory nuclear physics*. Wiley, New York
- Lanzafame HM, Blann M (1970) *Nucl Phys* 142:545
- Lee J, Tsang MB et al (2010) *Phys Rev Lett* 104 :112701
- Li B-A, Ko CM (1997) *Nucl Phys A* 618:498
- Li B-A, Chen L-W, Ko CM (2008) *Phys Rep* 464:113
- Li T, Garg U et al (2007) *Phys Rev Lett* 99:162503
- Loveland W (2007) *Phys Rev C* 76:014612
- Lovett R (2007) *Rep Prog Phys* 70:195
- Lynch WG (1987) *Annu Rev Nucl Part Sci* 37:493
- Magistro DJ et al (2000) *Phys Rev C* 61:C21602(R)
- Mahaux C, Sartor R (1990) *Adv Nucl Phys* 20:1
- McCalla SG, Lestone JP (2008) *Phys Rev Lett* 101:032702
- McMahan MA et al (1987) *Phys Rev Lett* 54:1995
- Messiah A (1958) *Quantum Mechanics*, Dover Books
- Moretto LG (1975) *Nucl Phys A* 247:211
- Mueller H, Serot BD (1995) *Phys Rev C* 52:2072
- Myo T, Kato K, Toki H, Ikeda K (2007) *Phys Rev C* 76:024305
- Natowitz J et al (2002) *Phys Rev Lett* 89:212701
- Natowitz J et al (2010) *Phys Rev Lett* 104, 202501
- NEA (2010) <http://www.nea.fr>
- NNDC (2010) <http://www.nndc.bnl.gov>
- Nörenberg W et al (1974) *Phys Lett B* 52:289
- Nörenberg W et al (1976) *Z Phys A* 274:241
- NRC (1999) In: Committee on Nuclear Physics, National Research Council (ed) *Nuclear physics: the core of matter, the fuel of stars*. <http://books.nap.edu/catalog/6288.html>
- Ono A, Horiuchi H (1996) *Phys Rev C* 53:2341, *Ibid.* p. 2958
- Otsuka T (2005) *Phys Rev Lett* 95:232502
- Pfaff R et al (1996) *Phys Rev C* 53:1753
- Pieper SC, Varga K, Wiringa RB (2002) *Phys Rev C* 66:044310
- Polish J et al (1990) *Phys Rev C* 41:942
- Pochodzalla J et al (1995) *Phys Lett* 75:1040
- Prakash M, Wambach J, Ma ZY (1983) *Phys Lett B* 128:141
- Randrup J (1978) *Ann Phys* (NY) 112:356
- Randrup J, Koonin SE (1981) *Nucl Phys A* 356:223
- Reisdorf W (1981) *Z Phys A* 300:227
- Reisdorf W, Ritter HG (1997) *Annu Rev Nucl Part Sci* 47:663
- RHIC (2005) BRAHMS, PHENIX, PHOBOS, and STAR white papers. *Nucl Phys A* 757:1
- RHIC (2010) <http://www.bnl.gov/RHIC>
- RIKEN (2010) <http://www.rarf.riken.go.jp>
- RNDP (2003) <http://www.ippe.obninsk.ru/podrcjcd/>
- Rolfs CE, Rodney WS (1988) *Cauldrons in the cosmos*. University of Chicago Press, Chicago
- Rutherford E (1911) *Phil Mag* 21:669
- Saint-Laurent F, Conjeaud M, Dayras R, Harar S, Oeschler H, Volant C (1984) *Nucl Phys A* 422:307
- Samaddar SK, De JN, Viñas X, Centelles M (2007) *Phys Rev C* 75:054608
- Samaddar SK, De JN, Viñas X, Centelles M (2008) *Phys Rev C* 78:034607
- Schlagel TJ, Pandharipande VJ (1987) *Phys Rev C* 36:162
- Schröder WU, Huizenga JR (1977) *Annu Rev Nucl Sci* 27:465
- Serber R (1947) *Phys Rev* 72:1114
- Shetty DV, Yennello SJ, Souliotis GA (2007) *Phys Rev C* 76:024606
- Shlomo S, Kolomietz VM (2004) *Rep Prog Phys* 67:1
- Shlomo S, Natowitz JB (1990) *Phys Lett B* 252:187
- Sobotka LG et al (1987) *Phys Rev C* 36:2713
- Sobotka LG, Charity RJ, Töke J, Schröder WU (2004) *Phys Rev Lett* 93:132702

- Sorlin O et al (1993) Phys Rev C 47:2941  
Strutinsky VM (1967) Nucl Phys A 95:420  
Subedi R et al (2008) Science 320:1476  
TAMU (2010) <http://cyclotron.tamu.edu/>  
Tamura T (1965) Rev Mod Phys 37:679  
Tanihata I et al (1985) Phys Rev Lett 55:2676  
Thirring W, Narnhofer H, Posch HA (2003) Phys Rev Lett 91:130601  
Töke J, Schröder WU (1992) Ann Rev Nucl Part Sci 42:401  
Töke J, Swiatecki WJ (1981) Nucl Phys A372:141  
Toneev VD et al (1990) Nucl Phys A 519:463c  
Trautmann W (2001) In: Norenberg W, Guerreau D, Metag V (eds) Nucleus-nucleus collisions 2000. North-Holland, Amsterdam  
TRIUMF (2010) <http://www.triumf.ca>  
Tsang MB et al (1984) Phys Lett 134B: 169  
Tsang MB et al (2009) Phys Rev Lett 102:122701  
Vandenbosch R (1992) Annu Rev Nucl Part Sci 42:447  
Vandenbosch R, Huizenga JR (1973) Nuclear fission. Academic, New York  
Viola VE, Kwiatkowski K, Walker M (1985) Phys Rev C 31:155  
Viola VE et al (2006) Phys Rep 434:1  
Wagemans C (2000) The nuclear fission process. CRC Press, Boca Raton  
Weisskopf VF, Ewing DH (1940) Phys Rev 57:672  
Wilczynski J et al (1973) Phys Lett 47b:484  
Wu J, Chang CC, Holmgren HD (1979) Phys Rev C 19:370  
Yariv Y, Fraenkel Z (1981) Phys Rev C 24:488  
Youngblood DL, Clark HL, Lui Y-W (1999) Phys Rev Lett 82:691

